WATER-FAT IMAGING AND GENERAL CHEMICAL SHIFT IMAGING WITH SPECTRUM MODELING

by

LI AN

B.Sc., Peking University, 1988
M.Sc., The University of Calgary, 1995

A THESIS SUBMITTED IN PARTIAL FULFILMENT OF
THE REQUIREMENTS FOR THE DEGREE OF

DOCTOR OF PHILOSOPHY

in

THE FACULTY OF GRADUATE STUDIES

DEPARTMENT OF PHYSICS & ASTRONOMY

THE UNIVERSITY OF BRITISH COLUMBIA

November 1998

0-612-38848-4

ABSTRACT

Water-fat chemical shift imaging (CSI) has been an active research area in magnetic resonance imaging (MRI) since the early 1980's. There are two main reasons for water-fat imaging. First, water-fat imaging can serve as a fat-suppression method. Removing the usually bright fatty signals not only extends the useful dynamic range of an image, but also allows better visualization of lesions or injected contrast, and removes chemical shift artifacts, which may contribute to improved diagnosis. Second, quantification of water and fat provides useful chemical information for characterizing tissues such as bone marrow, liver, and adrenal masses. A milestone in water-fat imaging is the Dixon method that can produce separate water and fat images with only two data acquisitions. In practice, however, the Dixon method is not always successful due to field inhomogeneity problems. In recent years, many variations of the Dixon method have been proposed to overcome the field inhomogeneity problem. In general, these methods can at best separate water and fat without identifying the two because the water and fat magnetization vectors are sampled symmetrically, only parallel and anti-parallel. Furthermore, these methods usually depend on two-dimensional phase unwrapping which itself is sensitive to noise and artifacts, and becomes unreliable when the images have disconnected tissues in the field-of-view (FOV).

We will first introduce the basic principles of nuclear magnetic resonance (NMR) and magnetic resonance imaging (MRI) in chapter 1, and briefly review the existing water-fat imaging techniques in chapter 2. In chapter 3, we will introduce a new method for water-fat imaging. With three image acquisitions, a general direct phase encoding (DPE) of the

chemical shift information is achieved, which allows an unambiguous determination of water and fat on a pixel by pixel basis. Details of specific implementations and noise performance will be discussed. Representative results from volunteers and patients in a clinical setting will be presented. In chapter 4, new improvements in the signal-to-noise-ratio (SNR) for the DPE method will be introduced and details of noise performance analysis will be discussed. In chapter 5, a special DPE sampling scheme will be introduced. With three-orthogonal phase (TOP) image acquisitions, it allows a correction of image magnitude errors caused by factors such as T_2^* relaxation. Details of data acquisition and signal processing will be discussed. Representative results from volunteers will be presented. In chapter 6, we will introduce a new two-point water-fat imaging method. By sampling water and fat asymmetrically and minimizing the gradient energy in a phase map, this method determines water and fat without ambiguity and handles disconnected tissues well. Details of data acquisition, signal processing, and noise performances will be discussed. Representative results from volunteers will be presented. In chapter 7, we will introduce a new general method of chemical shift imaging with spectrum modeling (CSISM). CSISM models a spectrum as several peaks with known resonance frequencies but unknown peak amplitudes which can be resolved from a set of spin-echo images. Details of data acquisition, signal processing and noise performances will be discussed. Representative results from phantom experiments and a clinical scan will be presented. In chapter 8, the general ideas, results and conclusions of all the methods we introduced in this thesis will be discussed, compared, and summarized.

TABLE OF CONTENTS

CHAPTER 1

CHAPTER 2

CHAPTER 3

CHAPTER 4

CHAPTER 5

CHAPTER 6

CHAPTER 7

CHAPTER 8

LIST OF FIGURES

ACKNOWLEDGEMENTS

I would like to acknowledge the following people for their contributions to this thesis. Dr. Qing-San Xiang, my supervisor, was involved in every aspect of this thesis, from general ideas to programming details. Dr. Alex MacKay, Dr. John Aldrich, and Dr. Myer Bloom offered me many constructive suggestions through committee meetings and other casual discussions. I am also grateful to all the people who have helped me and encouraged me while I was working at UBC, BC Children's Hospital, and St. Paul's Hospital.

DEDICATION

To my wife, Lan Li, and my parents, who give me reason and support

CHAPTER 1

INTRODUCTION

1.1 Important Discoveries in Nuclear Magnetic Resonance (NMR)

In 1933, Otto Stern and his collaborators first observed the effect of nuclear spin by the deflection of a beam of hydrogen molecules in a magnetic field [1,2]. In 1937, I. I. Rabi and his co-workers conducted the first successful nuclear magnetic resonance (NMR) experiment with a modified molecular beam apparatus [3]. In 1944, Otto Stern was awarded the 1943 Nobel Prize in Physics "for his contribution to the development of the molecular-ray method and his discovery of the magnetic moment of the proton" [4]. At the same time, the 1944 Nobel Prize in Physics was awarded to I. I. Rabi "for his resonance method for recording the magnetic properties of atomic nuclei" [4].

NMR in bulk materials was first achieved by two groups of physicists independently. One group of physicists were Edward M. Purcell, Henry C. Torrey, and Robert V. Pound, who were employed by MIT but carried out their experiments at Harvard University. They obtained the NMR signal with an absorption experiment in late 1945 [5]. In their experiment, a resonance cavity was placed in the gap of a large electromagnet. The cavity was filled with about 1kg of paraffin. A radiofrequency magnetic field fixed at 30 MHz was introduced into the cavity with the direction of the RF field perpendicular to the static field everywhere. The RF field output from the cavity was detected by a bridge circuit. They expected the cavity output to drop due to the absorption of the RF field by the paraffin when magnetic resonance occurs. It was known that, at resonance, the static magnetic field strength B and the RF angular frequency ω should satisfy the Larmor equation

$$\omega = \gamma B \tag{1-1}$$

where γ is the gyro-magnetic ratio. For hydrogen, γ_H is equal to 26752 rad/sec/gauss , or equivalently, $\gamma_H/2\pi$ is equal to 4.2577 kHz/gauss. The magnetic field strength B was slowly varied around the expected resonance value by changing the magnet current. At a field of 7100 Gauss, the cavity output dropped significantly. The first nuclear magnetic resonance in bulk material was thus observed. Another group of physicists at Stanford, consisting of Felix Bloch, W. W. Hansen, and Martin Packard, obtained a NMR signal in early 1946 with an induction method [6]. In their experiment, a brass box was placed in the gap of an electric magnet. Their sample of liquid water was put into the box along with two orthogonally placed RF coils. One coil was used to excite the sample with an RF field while the second coil was used to pick up the nuclear induction signal as the magnetization precessed around the static magnetic field after magnetic resonance. Bloch and Purcell shared the Nobel Prize in Physics in 1952 "for their development of new methods for nuclear magnetic precision measurements and discoveries in connection therewith" [4].

The use of NMR in imaging was introduced by Paul Lauterbur in late 1971. In his historical paper published in 1973 [7], Lauterbur described a method to generate a 2-dimensional or 3-dimensional NMR image by the use of magnetic field gradients in several directions and back-projecting the one-dimensional spectra produced from each gradient. The first Fourier transform (FT) imaging technique was proposed by Kumar, Welti, and Ernst in 1975 [8]. A few years later, a modified FT imaging method was developed by Edelstein *et al* and named as “spin warp” method [9]. Most of the imaging pulse sequences we use today are based on this spin warp method. In the next section, we will introduce some basic principles of NMR physics and spin warp imaging.

1.2 Magnetization at Equilibrium

A nucleus with an odd number of protons and/or an odd number of neutrons possesses a magnetic moment and is referred to as a spin. When a spin is placed in a magnetic field, the spin will have a potential energy. To analyze this single spin system with quantum mechanics, the Hamiltonian H is set to be equal to the potential energy of the spin

$$H = -\mu \cdot \mathbf{B} \tag{1-2}$$

where μ is the magnetic moment of the spin and **B** the magnetic field. The magnetic moment μ is related to the spin angular momentum **S** by

$$\mu = \gamma \mathbf{S} \tag{1-3}$$

Thus

$$H = -\gamma \mathbf{S} \cdot \mathbf{B} = -\gamma S_z B \tag{1-4}$$

Where operator S_z is the z component of **S**. It is easy to see that the stationary states of the system are the eigenstates of S_z and the energy levels are given by

$$E_{m_s} = -\gamma \hbar B m_s \qquad\qquad -s \le m_s \le s \tag{1-5}$$

The constant $\hbar$ is equal to h/2π, where h is known as the Plank’s constant. s is the quantum number of the spin angular momentum **S**. For a proton spin, s is known to be 1/2. Thus m_s can only be -1/2 and 1/2, corresponding to "spin-down" and "spin-up" eigenstates respectively. The energy separation of the two states is

$$\Delta E = \gamma \hbar B \tag{1-6}$$

which is illustrated in Figure (1-1). A transition from the lower to the upper state can be made by absorption of RF energy of angular frequency ω which satisfies

$$\hbar \omega = \Delta E \tag{1-7}$$

Substituting equation (1-6) into equation (1-7), the Larmor equation given in equation (1-1) is obtained. For a large number of proton spins in a magnetic field, the population of spins on each energy state follows Boltzmann's distribution when the system reaches thermal equilibrium. The spin population ratio R between the spin-down and spin-up states is given by

$$R = \frac{n_-}{n_+} = \exp(-\frac{\Delta E}{kT}) = \exp(-\frac{\gamma \hbar B}{kT}) \tag{1-8}$$

where the Boltzmann's constant k equals 1.38×10^{-23} Joule/ K^o. At a room temperature of $T \approx 300$ K^o and a magnetic field of $B = 1.5$ Tesla, $\Delta E / kT$ is about 1.0×10^{-5}. Therefore, R is approximately

$$R \approx 1 - \frac{\Delta E}{kT} = 1 - \frac{\gamma \hbar B}{kT} \tag{1-9}$$

Hence, there are slightly more protons on the spin-up state than on spin-down state, resulting in a net macroscopic magnetization. Magnetization is defined as the total magnetic moment in a unit volume. Considering a total of N protons in a unit volume, the magnetization vector $\mathbf{M}_0$ can be calculated by,

$$\begin{aligned} M_0 &= \mu(n_+ - n_-) \\ &= \mu(n_+ + n_-)\frac{(n_+ - n_-)}{(n_+ + n_-)} \\ &= \mu N\frac{(1-R)}{(1+R)} \\ &\approx \mu N\frac{\gamma\hbar B}{2kT} \\ &= \frac{\gamma^2\hbar^2}{4kT}NB \end{aligned} \qquad (1\text{-}10)$$

where $\mu = \gamma\hbar/2$ is used, which can be derived from equation (1-3). From equation (1-10), we see that the magnetization vector at thermal equilibrium lies in the direction of **B** and has a magnitude proportional to the strength of **B**, and is also proportional to the proton number density N.

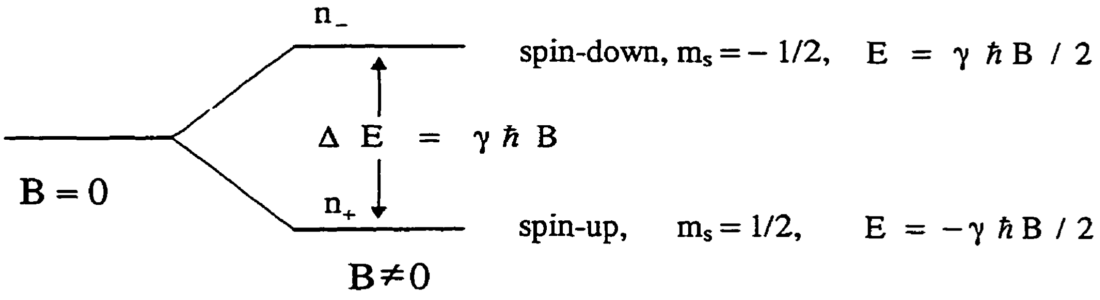

Figure 1-1 Energy splitting of a proton spin in a magnetic field.

1.3 Equation of motion for the Magnetization Vector

In the previous section, we calculated $\mathbf{M}_0$ in a static magnetic field **B** at thermal equilibrium. Here, we will analyze the dynamic behavior of magnetization vector **M** in a magnetic field **B** that is generally time dependent. As a time-independent operator in quantum mechanics, the magnetic moment μ satisfies the following equation of motion

$$\frac{d}{dt}<\mu>=\frac{i}{\hbar}<[H,\mu]> \tag{1-11}$$

where "< >" denotes the expectation value of a variable, and $[H,\mu]$ is the commutator of the Hamiltonian H and magnetic moment μ. Substituting the definitions of H and μ defined in equation (1-2) and equation (1-3) into equation (1-11), as well as using the following commutation properties of **S**

$$\begin{aligned}
[S_x,S_y] &= i\hbar S_z \\
[S_y,S_z] &= i\hbar S_x \\
[S_z,S_x] &= i\hbar S_y
\end{aligned} \tag{1-12}$$

Equation (1-11) can be transformed into

$$\frac{d}{dt}<\mu>=<\mu>\times\gamma\mathbf{B} \tag{1-13}$$

where "×" denotes cross product. For an ensemble of N non-interacting proton spins in a unit volume, the magnetization vector **M** is equal to $N<\mu>$. Thus, the equation of motion for the magnetization vector **M** is

$$\frac{d}{dt}\mathbf{M}=\mathbf{M}\times\gamma\mathbf{B}. \tag{1-14}$$

Considering a static magnetic field in the z-direction $\mathbf{B}=B_0\mathbf{z}$, equation (1-14) has the following general solution

$$\begin{aligned}
M_x(t) &= M_x(0)\cos\omega_0 t + M_y(0)\sin\omega_0 t \\
M_y(t) &= -M_x(0)\sin\omega_0 t + M_y(0)\cos\omega_0 t \\
M_z(t) &= M_z(0)
\end{aligned} \tag{1-15}$$

where $M_x(t)$, $M_y(t)$, $M_z(t)$ are the three components of **M** at time instance t while $M_x(0)$, $M_y(0)$, $M_z(0)$ are their initial values. The constant ω_0 is the Larmor frequency given by $\omega_0=\gamma B_0$. The solution means the magnetization vector **M** will precess about **B** forever after being tipped away from the direction of the magnetic field **B**, see Figure 1-2. How to tip **M** away from the direction of **B** will be discussed in detail in the next section.

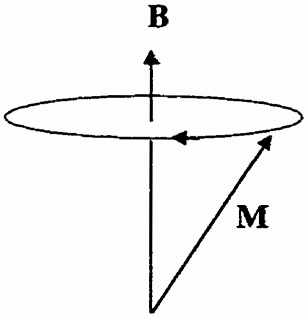

Figure 1-2 The precession of **M** about the magnetic field **B**.

In the above analysis of the motion of magnetization **M**, relaxation effects of **M** have been ignored. There are two relaxation processes going on after **M** is tipped away from the direction of **B**, one of which is T_1 relaxation and the other is T_2 relaxation. T_1 relaxation is a measure of the time for the longitudinal component of the magnetization to go back to its thermal equilibrium value. During T_1 relaxation, spins give up energy to the surrounding lattice in order to go back to their lowest energy state, i.e. the state of thermal equilibrium. Hence, T_1 relaxation is also called spin-lattice relaxation. T_2 relaxation is a measure of the time of disappearance of the transverse component of the magnetization. T_2 relaxation can be understood as follows. The interactions among spins cause internal magnetic field inhomogeneity. The magnetization vectors of different spin groups will precess at slightly different free-precession frequencies if they experience slightly different magnetic fields. After a period of time, the transverse component of the net magnetization vector **M** will disappear as the transverse components of the magnetization vectors of different spin groups lose coherence. T_2 relaxation is also called spin-spin relaxation. T_1 is greater than T_2 for biological tissues. Typically, T_1 is in the order of 1 sec and T_2 is in the range of 10 ms to 100 ms.

Taking the relaxation processes into consideration, the equation of motion for the magnetization is described by the Bloch equation,

$$\frac{d}{dt}\mathbf{M}=\mathbf{M}\times\gamma\mathbf{B}-\frac{M_x\mathbf{x}+M_y\mathbf{y}}{T_2}-\frac{(M_z-M_0)\mathbf{z}}{T_1} \tag{1-16}$$

where M_0 is the magnitude of the magnetization vector **M** at thermal equilibrium. Considering a constant magnetic field $\mathbf{B}=B_0\mathbf{z}$, equation (1-16) can be written in components as

$$\begin{aligned}\frac{d}{dt}M_x &= \gamma M_y B_0 - \frac{M_x}{T_2}\\ \frac{d}{dt}M_y &= -\gamma M_x B_0 - \frac{M_y}{T_2}\\ \frac{d}{dt}M_z &= -\frac{M_z - M_0}{T_1}\end{aligned} \tag{1-17}$$

which has the following general solution,

$$\begin{aligned}M_x(t) &= [M_x(0)\cos\omega_0 t + M_y(0)\sin\omega_0 t)]\exp(-t/T_2)\\ M_y(t) &= [-M_x(0)\sin\omega_0 t + M_y(0)\cos\omega_0 t]\exp(-t/T_2)\\ M_z(t) &= M_0 + [M_z(0) - M_0]\exp(-t/T_1)\end{aligned} \tag{1-18}$$

The above equation expresses in a quantitative manner that M not only precesses about B_0 at the Larmor frequency but also has T_1 longitudinal relaxation time T_1 and transverse relaxation time T_2, see Figure 1-4(a). To simplify the equation of motion for **M**, we introduce a rotating frame of reference (**x'**, **y'**, **z'**), which rotates clock-wise around z-direction at Larmor frequency $\omega_0 = \gamma B_0$, see Figure 1-3.

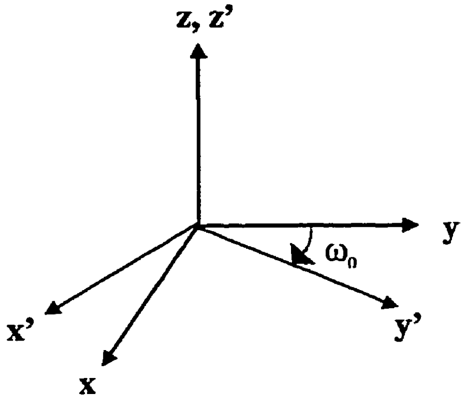

Figure 1-3 Rotating frame of reference (x', y',z')

The time derivative of **M** in the rotating frame $\frac{d'}{dt}\mathbf{M}$ is related to the time derivative of **M** in the laboratory frame $\frac{d}{dt}\mathbf{M}$ by,

$$\frac{d'}{dt}\mathbf{M} = \frac{d}{dt}\mathbf{M} - \Omega \times \mathbf{M} \tag{1-19}$$

where Ω is the angular velocity of the rotating frame relative to the laboratory frame and is equal to $-\omega_0\mathbf{z}$. Hence, the Bloch equations in the rotating frame can be obtained by substituting equation (1-16) into equation (1-19),

$$\frac{d'}{dt}\mathbf{M} = \mathbf{M} \times \gamma \Delta \mathbf{B} - \frac{M_x x' + M_y y'}{T_2} - \frac{(M_z - M_0) z'}{T_1} \tag{1-20}$$

where $\Delta\mathbf{B}$ is the effective field in the rotating frame and is given by $\Delta\mathbf{B} = \mathbf{B} - B_0\mathbf{z}$. When there is no other field but the homogeneous static field $B_0\mathbf{z}$, $\Delta\mathbf{B}$ equals zero and the solution of the Bloch equation in the rotating frame is,

$$\begin{aligned} M'_x(t) &= M'_x(0)\exp(-t/T_2) \\ M'_y(t) &= M'_y(0)\exp(-t/T_2) \\ M'_z(t) &= M_0 + [M'_z(0) - M_0]\exp(-t/T_1) \end{aligned} \tag{1-21}$$

where $M'_x(t)$, $M'_y(t)$, $M'_z(t)$ are the three components of **M** at time instance t in the rotating frame while $M'_x(0)$, $M'_y(0)$, $M'_z(0)$ are their initial values. In the rotating frame of reference, the magnetization vector only undergoes T_1 and T_2 relaxation processes and has no precession since the effective field is zero, see Figure 1-4 (b).

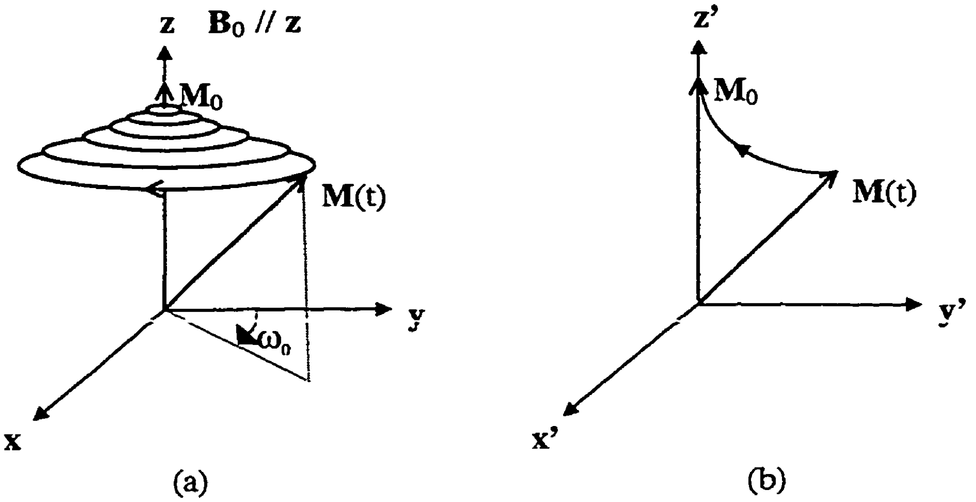

Figure 1-4 Time evolution of the magnetization vector **M** in the laboratory frame (a) and in the rotating frame (b)

1.4 RF Excitation and Signal Reception

Now it is time to answer the question of how to tip the magnetization vector away from the direction of the static magnetic field. The answer lies in the original induction experiment performed by Bloch *et al.* In the induction experiment, the magnetization vector was tipped away from the direction of the static magnetic field by applying an RF field perpendicular to the static magnetic field. Then, the magnetization vector will precess about the static magnetic field and induce a signal in a receiving coil. This induction method has been and still is the foundation of NMR technologies. We will use a simple example to explain the induction theory.

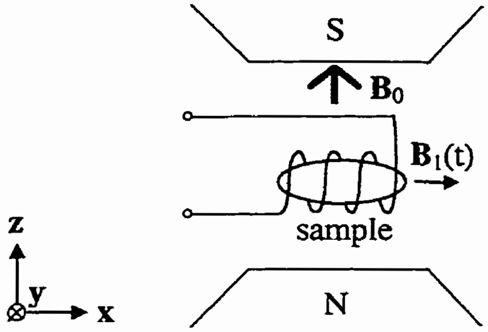

Figure 1-5 Schematic illustration of NMR signal induction

As shown in Figure 1-5, a small sample is placed in a static magnetic field $\mathbf{B}_0 = B_0\mathbf{z}$. The magnetization vector of the sample at thermal equilibrium will be in the $\mathbf{B}_0$ direction and is assumed to be $\mathbf{M}_0 = M_0\mathbf{z}$. An RF coil is placed along the x-axis to transmit an RF field $\mathbf{B}_x(t)$ to excite the sample. The RF field is tuned to the Larmor frequency and is given by

$$\mathbf{B}_x(t) = \mathbf{x}\,2B_1 \cos\omega_0 t \tag{1-22}$$

This linearly polarized field can be decomposed into two circularly polarized components $\mathbf{B}_x(t) = \mathbf{B}_1(t) + \mathbf{B}_1'(t)$, with $\mathbf{B}_1(t)$ rotating clockwise and $\mathbf{B}_1'(t)$ rotating counter-clockwise

$$\begin{aligned} \mathbf{B}_1(t) &= \mathbf{x}\,B_1 \cos\omega_0 t - \mathbf{y}\,B_1 \sin\omega_0 t \\ \mathbf{B}_1'(t) &= \mathbf{x}\,B_1 \cos\omega_0 t + \mathbf{y}\,B_1 \sin\omega_0 t \end{aligned} . \tag{1-23}$$

In the rotating frame of reference, $\mathbf{B}_1(t)$ becomes a constant field and $\mathbf{B}_1'(t)$ rotates at an angular velocity twice of the Larmor frequency,

$$\begin{aligned}\mathbf{B}_1(t) &= \mathbf{x}' B_1 \\ \mathbf{B}_1'(t) &= \mathbf{x}' B_1 \cos 2\omega_0 t + \mathbf{y}' B_1 \sin 2\omega_0 t\end{aligned} \tag{1-24}$$

Because the duration of RF field is very short compared to T_1 and T_2, the relaxation effects during the RF excitation period are ignored. The equation of motion for **M** in the rotating frame of reference is,

$$\frac{d'}{dt}\mathbf{M} = \mathbf{M} \times \gamma \Delta\mathbf{B} = \mathbf{M} \times \gamma \mathbf{B}_1(t) + \mathbf{M} \times \gamma \mathbf{B}_1'(t) \tag{1-25}$$

Since $\mathbf{B}_1'(t)$ is rotating with angular velocity $2\omega_0$, the torque $\mathbf{M} \times \gamma \mathbf{B}_1'(t)$ averages to zero and has no significant effect on **M**. The equation of motion can be simplified as,

$$\frac{d'}{dt}\mathbf{M} = \mathbf{M} \times \gamma \mathbf{B}_1(t) \tag{1-26}$$

The solution of the above equation is given by,

$$\begin{aligned}M_{x'}(t) &= 0 \\ M_{y'}(t) &= M_0 \sin \gamma B_1 t \\ M_{z'}(t) &= M_0 \cos \gamma B_1 t\end{aligned} \tag{1-27}$$

which represents the precession of **M** about the **x'** axis at an angular velocity γB_1, see Figure 1-6. The flip angle α of the magnetization is given by,

$$\alpha = \gamma B_1 \tau \tag{1-28}$$

where τ is the duration of the RF pulse. The magnitude of $\mathbf{M}_T$, the transverse component of **M**, is calculated by

$$M_T = M_0 \sin(\alpha) = M_0 \sin(\gamma B_1 \tau) \tag{1-29}$$

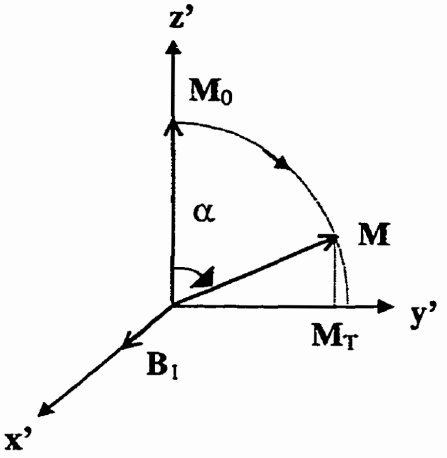

Figure 1-6 Nutation of **M** in the rotating frame of reference.

After the termination of the RF field $\mathbf{B}_x$, the effective field becomes zero and the magnetization vector stays stationary in the rotating frame. In the laboratory frame, however, the magnetization vector **M** precess about z axis at angular velocity ω_0, see Figure 1-7 (a). The rotation of $\mathbf{M}_T$ induces an electromotive force (emf) in the coil that can be observed using an oscilloscope. The emf in the coil is called free induction decay (FID) and will persist in the coil until M_T decays out by T_2 relaxation and other factors. The FID is schematically illustrated in Figure 1-7 (b).

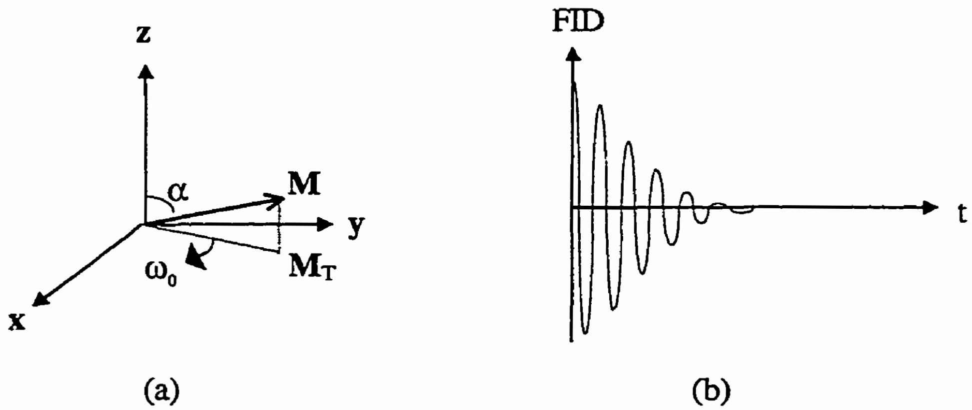

(a) (b)

Figure 1-7 (a) Free precession of **M** in the laboratory frame after termination of the RF pulse (b) Induced voltage in the coil

Now, we will show how to calculate the FID signal. For an elementary volume dV at location $\mathbf{r}$ in a sample, the elementary magnetic moment is given by $d\mathbf{m} = \mathbf{M}(\mathbf{r},t)\,dV$. The transverse component of the magnetic moment is given by $d\mathbf{m}_T = \mathbf{M}_T(\mathbf{r},t)\,dV$. The free precession of $d\mathbf{m}_T$ at Larmor frequency will induce an electromotive force (emf) in the coil. The total emf in the coil is the integral of the contributions from all the elementary magnetic moments. A master equation for the signal from a NMR experiment was developed by Hoult *et al* [10] that can be expressed as,

$$\begin{aligned} \xi(t) &= -\frac{d}{dt}\int \tilde{\mathbf{B}}_1(\mathbf{r})\cdot\mathbf{M}(\mathbf{r},t)dV \\ &= \int \omega_0 \tilde{B}_{1T}(\mathbf{r})M_T(\mathbf{r},t)\cos[\phi(\mathbf{r},t)-\omega_0 t]\,dV \end{aligned} \tag{1-30}$$

where $\xi(t)$ is the induced emf or voltage in the coil: $\tilde{\mathbf{B}}_1(\mathbf{r})$ is a hypothetical magnetic field and $\tilde{\mathbf{B}}_{1T}(\mathbf{r})$ its transverse component; $\phi(\mathbf{r},t)$ represents the phase angle of $\mathbf{M}_T(\mathbf{r},t)$ in the rotating frame of reference. Based on the principle of reciprocity, the hypothetical magnetic field $\tilde{\mathbf{B}}_1(\mathbf{r})$ is defined as the magnetic field that would be created by the coil if 1 A of current were to be passed through it. Because both M_T and ω_0 are proportional to the static magnetic field strength B_0, according to equations (1-1) and (1-10), the induced signal is proportional to B_0^2.

In order to analyze the FID signal, we need to demodulate the signal and store it into a computer. Quadrature signal detection is widely used to demodulate the signal. In quadrature signal detection, the FID signal $\xi(t)$ is split into two channels $\xi_1(t)$ and $\xi_2(t)$ by multiplying two reference signals which are $\cos\omega_0 t$ and $\sin\omega_0 t$ respectively,

$$\begin{aligned}\xi_1(t) &= \xi(t)\cos\omega_0 t = \frac{1}{2}\int \omega_0\tilde{B}_{1T}M_T\cos(2\omega_0 t-\phi)dV + \frac{1}{2}\int \omega_0\tilde{B}_{1T}M_T\cos(\phi)dV \\ \xi_2(t) &= \xi(t)\sin\omega_0 t = \frac{1}{2}\int \omega_0\tilde{B}_{1T}M_T\sin(2\omega_0 t-\phi)dV + \frac{1}{2}\int \omega_0\tilde{B}_{1T}M_T\sin(\phi)dV\end{aligned} \tag{1-31}$$

Typically, $2\omega_0$ is in MHz range while the rate of change of ϕ is in the KHz range. So, the low frequencies of the signal can be separated from the high frequencies of the signal by a low pass filter. After low pass filtering, the signals in the two channels become

$$\begin{aligned}\xi_1(t) &= \frac{1}{2}\int \omega_0\tilde{B}_{1T}M_T\cos(\phi)dV \\ \xi_2(t) &= \frac{1}{2}\int \omega_0\tilde{B}_{1T}M_T\sin(\phi)dV\end{aligned} \tag{1-32}$$

The signals of the two channels can be combined into one complex signal array S(t) which is defined as $S(t) = \xi_1(t) + i\xi_2(t)$. Therefore,

$$S(t) = \frac{1}{2}\int \omega_0\tilde{B}_{1T}M_T\exp(i\phi)\,dV \tag{1-33}$$

For a well designed coil, $\tilde{B}_{1T}$ is highly uniform and can be considered as a constant in the whole region of interest. For simplicity, all constants are removed from equation (1-33) and S(t) becomes

$$S(t) = \int M_T\exp(i\phi)\,dV \tag{1-34}$$

It is not difficult to see that $M_T\exp(i\phi)$ is the complex form representation of the transverse magnetization vector $\mathbf{M}_T$ in the rotating frame. As an integral of $\mathbf{M}_T$ over the whole volume of the RF excited part of the sample, the complex signal S(t) is actually the total magnetic moment of the sample at time t in the rotating frame.

For the above simple induction experiment, the direction of transverse magnetization stay stationary in the rotating frame, thus ϕ is equal to zero. The complex signal S(t) is written as

$$\begin{aligned} S(t) &= \int M_T dV \\ &= VM_T \\ &= VM_0 \sin(\alpha)\exp(-t/T_2) \end{aligned} \tag{1-35}$$

where V is the total volume of the RF excited part of the sample. The signal S(t) is simply a T_2 decay curve.

1.5 Proton Chemical Shift Spectroscopy

In the previous sections, all of our theories were based on the assumption that the resonance frequency of a proton spin depends only on the external magnetic field according to the Larmor relationship. If this is strictly so, NMR would have been of little use in chemistry and biology. However, it was observed that nuclei in different chemical environments may have different resonance frequency shifts. The resonance frequency shift depends on the molecular structure, and thus, is referred to as the chemical shift. The first observation of chemical shift was reported by Proctor and Yu when they use ammonium nitrate (NH_4NO_3) to determine the magnetic moment of ^{14}N [11]. A saturated solution in water produced two strong lines instead of one. The observation was attributed to some "nasty" chemical effect. Arnold *et al* first clearly demonstrated the chemical shift effect by the observation of three separate lines in the NMR spectrum of ethanol (CH_3CH_2OH) [12]. The three separate lines are associated with three different chemical groups, CH_3, CH_2, and OH.

The cause of the chemical shift can be explained as follows, which is diagrammatically illustrated in Figure 1-8.

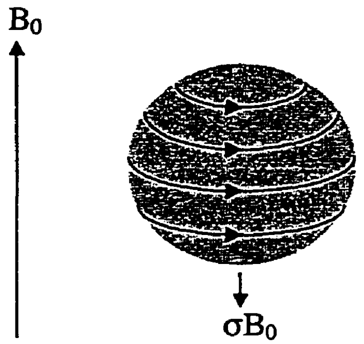

Figure 1-8 Electron shielding: the origin of chemical shift

In the external magnetic field $\mathbf{B_0}$, the electron cloud surrounding the nucleus is induced to circulate counter-clockwise about $\mathbf{B_0}$. The moving negative charge will generate an electric current circulating clockwise, which in turn creates a small magnetic field σB_0 opposing the external field. The term σ is a dimensionless shielding constant, which is independent of the external magnetic field. The magnitude of σ is very small and typically on the order of a few parts per million (ppm) for protons. The effective field that the nucleus experiences is given by

$$B = B_0 - \sigma B_0 = (1 - \sigma) B_0 \tag{1-36}$$

Thus, according to Larmor equation, the resonance frequency ω becomes

$$\omega = \gamma B = \gamma (1 - \sigma) B_0 \tag{1-37}$$

Ideally, the shielding constant σ could be calculated by knowing ω, γ, and B_0 accurately. However, it is not easy to generate a highly accurate magnetic field. On the other hand, it is convenient to measure the frequency difference between the resonance frequency of the sample and that of a standard chemical with the same nucleus, and then calculate the ratio of the frequency difference and the resonance frequency of the standard chemical. This ratio will be quoted as the chemical shift for the sample. For proton chemical shift experiments, TMS (tetramethyl silane, $Si(CH_3)_4$) is an accepted standard. The chemical shift δ is defined as

$$\delta = \frac{\omega - \omega_{TMS}}{\omega_{TMS}} \tag{1-38}$$

where ω_{TMS} is the resonance frequency of TMS. Chemical shift δ is related to the shielding constant σ by

$$\begin{aligned} \delta &= \frac{\omega - \omega_{TMS}}{\omega_{TMS}} \\ &= \frac{\gamma(1-\sigma)B_0 - \gamma(1-\sigma_{TMS})B_0}{\gamma(1-\sigma_{TMS})B_0} \\ &= \frac{\sigma_{TMS} - \sigma}{1-\sigma_{TMS}} \\ &\approx \sigma_{TMS} - \sigma \end{aligned} \tag{1-39}$$

where σ_{TMS} is the shielding constant of TMS. Because the protons in TMS are highly shielded, the shielding constant of TMS is greater than that of most other substances. Therefore the chemical shift δ is usually a small positive number on the order of several ppm.

Modern proton chemical shift spectroscopy experiments are usually done with the Fourier transform (FT) method, which was introduced by Ernst *et al* in 1965 [13]. The basic concept of FT spectroscopy can also be illustrated by using the simple induction experiment shown in Figure 1-5. The sample in this experiment can be a mixture of proton nuclei of different chemicals. These proton nuclei with a broad range of resonance frequencies are excited by a wide bandwidth RF field, i.e. all the nuclei with slightly different Larmor frequencies are all nutated down 90° to the transverse plane. The FID is then acquired and demodulated into complex signal S(t) which is the total transverse magnetic moment in the rotating frame. Due to their different chemical shifts, protons in different chemical components can have different Larmor frequencies and precess with different frequency ω' in the rotating frame. The rotating frame is selected to be rotating at the center frequency of the RF field. Ignoring the relaxation effects during data acquisition and field inhomogeneity, S(t) can be written as

$$S(t) = V\int M_T(\omega')\exp(-i\,\omega' t)\,d\omega' \qquad (1\text{-}40)$$

where $M_T(\omega')$ is the transverse magnetization for the nuclei with Larmor frequency ω'. It is clear that S(t) is the Fourier transform of $M_T(\omega')$ which is what we want to obtain from the spectrocopy experiment. However, S(t) only covers half of the time domain, as shown in Figure 1-6 (b). The other half can be filled with the hermitian conjugate of the available data due to the fact that $M_T(\omega')$ should have real values. This is equivalent to inverse Fourier transforming S(t) and taking the real part of the result as $M_T(\omega')$. Because spin density is proportional to M_T, the spectrum $M_T(\omega')$ is actually the spin density distribution as a function of resonance frequency. With the help of this spectrum, we can know the chemical constituents of the sample.

1.6 Spin-Echo Experiments

In reality, the static magnetic field $\mathbf{B}_0$ is not perfectly homogeneous in space. The inhomogeneity mainly comes from two sources. One source is the imperfection in the magnet that makes the external magnetic field $\mathbf{B}_0$ not perfectly homogeneous. The other source is the susceptibility variations in the sample. Even if the external magnetic field is perfectly homogenous, the local magnetic field experienced by the spins can be changed by susceptibility variations in the sample. As a result of field inhomogeneity, different spin groups may experience slightly different magnetic fields and precess at different frequencies after a 90° RF pulse. In the rotating frame of reference, the magnetization vectors for different spin groups will fan out and their vector sum, i.e. the magnetization vector **M**, will gradually disappear, see Figure 1-9.

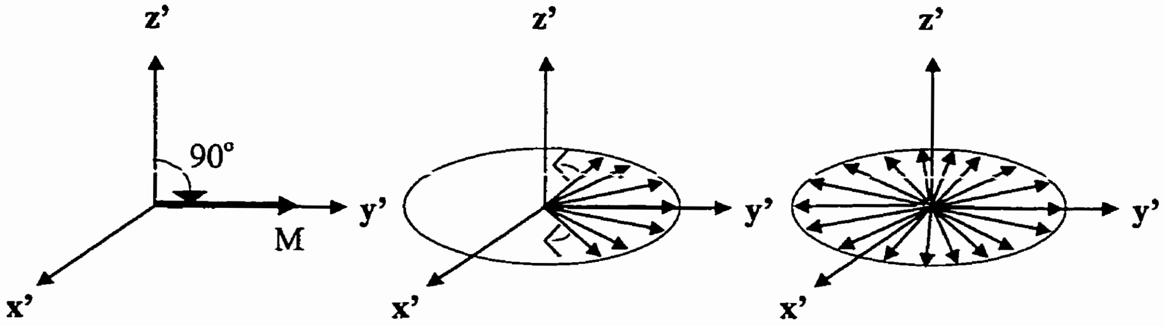

Figure 1-9 Dephasing of spins in the rotating frame of reference due to field inhomogeneity.

Taking into account the decay due to field inhomogeneity, the transverse component of magnetization decays with an effective time constant T_2^*

$$\frac{1}{T_2^*} = \frac{1}{T_2} + \gamma \Delta B . \qquad (1\text{-}41)$$

where ΔB is a measure of the field inhomogeneity. Obviously, T_2 is longer than T_2^*, so the decay of the FID is dominated by T_2^*, and T_2 can not be determined directly from the FID signal. However, the signal loss due to field inhomogeneity is recoverable. T_2 can be measured by a spin-echo experiment. E. L. Hahn performed the original spin-echo experiment in 1949 with two 90° pulses [14]. Carr and Purcell made several significant improvements over Hahn's method [15]. We use a CP (named after Carr and Purcell) pulse sequence to illustrate how a spin-echo experiment works. The CP pulse sequence is denoted as $90°_{x'} - \tau - 180°_{x'} - \tau - \text{echo}$. At time $t = 0$, a $90°$ pulse is applied in the x' direction to nutate the magnetization vector down onto the transverse plane, see Figure 1-10 (a). The duration of the $90°$ pulse is ignored since it is very short. After the $90°$ pulse, the magnetization vectors of different spin groups begin to fan out due to field inhomogeneity, resulting in a reduced total magnetization and FID, see Figure 1-10 (b). At time $t = \tau$, a $180°$ pulse is applied in the same direction as the $90°$ pulse. All the spin magnetization vectors are flipped over around the x' axis, see Figure 1-10 (c). After the $180°$ pulse, the spin magnetization vectors keep precessing clockwise or counter-clockwise the same as before the $180°$ pulse since all spins still experience the same local field. However, the relative advancing or lagging relationship among the spin magnetizaiton vectors had been changed by the $180°$ pulse, therefore the spin magnetization vectors are refocusing after the $180°$ pulse, see Figure 1-10 (d). At time $t = 2\tau$, all the magnetization vectors of different spin groups are refocused, resulting in a peak total magnetization and FID signal, see Figure 1-10 (e).

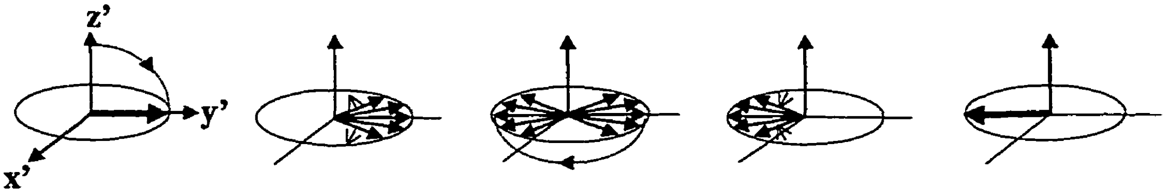

(a) 90° pulse (b) dephasing (c) 180° pulse (d) refocusing (e) echo

Figure 1-10 Spin phase diagram for the CP spin-echo pulse sequence

If we continue to apply $180°$ pulses at time $t = 3\tau, 5\tau, \cdots$, spin echoes also occur at $t = 4\tau, 6\tau, \cdots$. The signal amplitudes of the echoes decay at a rate determined by T_2 since the decay caused by field inhomogeneity has been eliminated by spin-echoes. The signal amplitudes of the echoes are given by the following relation

$$S(2n\tau) = S(0)\exp(-2n\tau / T_2), \qquad n = 0,1,2,\cdots \qquad (1\text{-}42)$$

where S is the signal amplitude. This relation is illustrated in Figure 1-11.

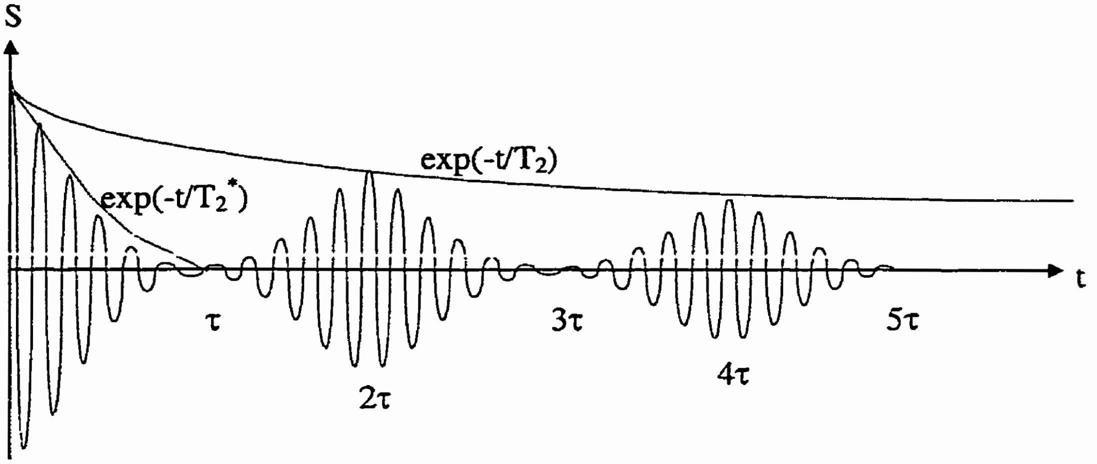

Figure 1-11 Signal decay curve for a train of spin echoes

From the above curve, T_2 can be measured correctly. In the above analysis, we ignored the chemical shift. In fact, different spin groups belongs to different substances can precess with different frequencies at the same external field strength due to their different chemical shifts. This will also cause spin dephasing. Spin-echo can refocus the dephasing caused by both chemical shift and field inhomogeneity. Thus Spin-echo can significantly reduce signal loss caused by spin dephasing and is frequently used in NMR spectroscopy and imaging.

1.7 Magnetic Resonance Imaging (MRI)

In the early years of NMR development, spectroscopy played a central role. Through NMR spectroscopy, scientists can gain a great deal of knowledge about the molecular structures of a substance. Nevertheless, NMR spectroscopy provides very limited spatial information. With the advent of MRI, we are able to obtain excellent 2D or 3D magnetic resonance (MR) images of the human body, which is of great use for medical diagnosis. Today, MRI has become one of the most important applications of NMR. In this section, we will use an open field magnetic resonance (MR) imager to introduce the basic principles of spin warp MR imaging.

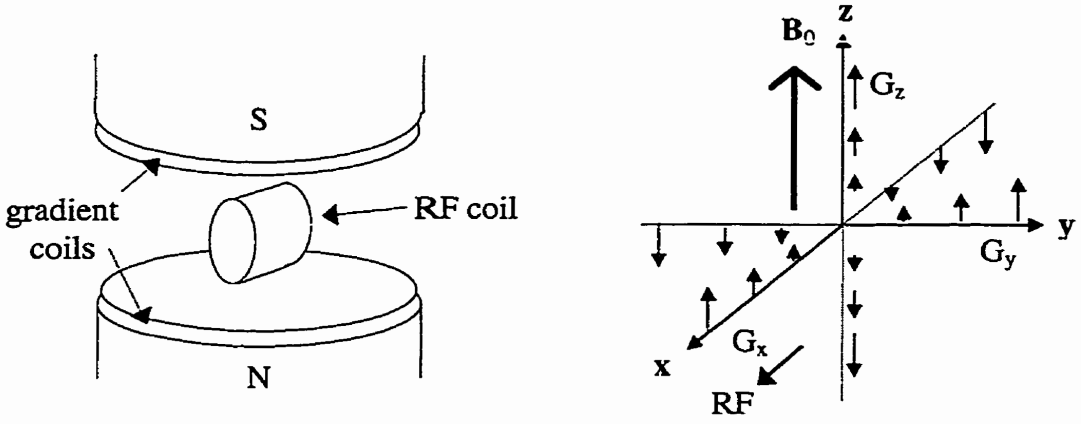

Figure 1-12 An open field magnet and its magnetic fields

Figure 1-12 schematically shows the main magnet, the gradient coils, and the RF coil of an open field MR imager. This imager has the main magnetic field $\mathbf{B}_0$ in the vertical direction and directed upward. The main magnet could be a permanent magnet, a resistive electromagnet, or a superconducting electromagnet. There are three sets of biplanar gradient coils for generating magnetic field gradients G_x, G_y, and G_z. Note that the magnetic fields generated by the three sets of gradient coils are all in the **z** direction but the gradients of the magnetic field strength are in three orthogonal directions, i.e. **x**, **y** and **z**. The total magnetic field strength in the z direction has the following form

$$B(r) = B_0 + \mathbf{r} \cdot \mathbf{G} = B_0 + xG_x + yG_y + zG_z \qquad (1\text{-}43)$$

The field gradients can be switched on and off rapidly and altered in magnitude by changing the currents flowing through the gradient coils. By controlling the currents in the three sets of gradient coils, G_x, G_y, and G_z can be adjusted separately and combined into a vector **G** that can be in any direction. A typical value of the maximum field gradient in each direction is 1 gauss/cm.

In 2D imaging schemes, signal response in the third dimension needs to be restricted. This is accomplished by selectively exciting only the spins in a well-defined slice of tissue [16]. In order to achieve this, a field gradient in the normal direction of the chosen slice is applied, causing a linear variation of Larmor frequencies of the spins along the gradient direction. All the spins on the chosen slice will have the same Larmor frequency, say ω_0 for example. Then an RF pulse with center frequency ω_0 is applied in a direction perpendicular to $\mathbf{B}_0$, say the **x** direction. Only the spins on the chosen slice are on resonance and can be tipped down onto the transverse plane (being excited). The RF pulse will not affect all the spins outside the chosen slice. In practice, the RF pulse has a bandwidth $\Delta\omega$, resulting in a finite slice thickness d. To the first order approximation, the slice profile is the frequency spectrum of the RF pulse. So a "sinc-shaped" RF pulse will give a rectangular slice profile. The RF bandwidth $\Delta\omega$, the slice selective gradient amplitude G_{slice}, and slice thickness d is related by

$$\Delta\omega = \gamma G_{slice} d \tag{1-44}$$

which shows that the slice thickness is controlled by both the RF bandwidth and slice selective gradient amplitude. The slice orientation is determined by the direction of the slice selective gradient. The slice location is usually shifted by offsetting the RF center frequency. In MRI, it is customary to introduce a new logical coordinate system (**x**, **y**, **z**). The old coordinate system (x, y, z) is called the physical coordinate system. The **z** direction of the logical system is in the normal direction of the chosen slice, see Figure 1-13.

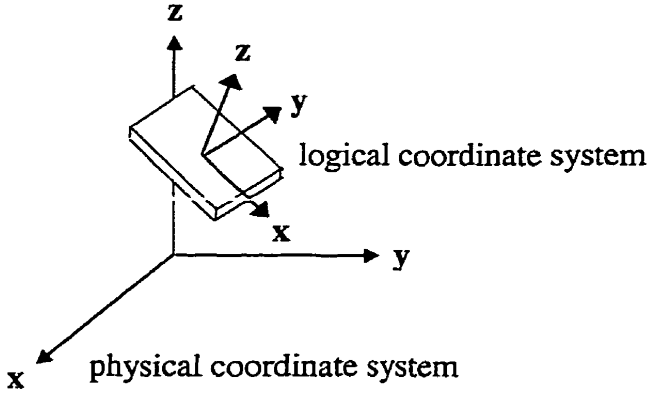

Figure 1-13 Physical and logical coordinate systems

The slice selective gradient G_{slice} can also be denoted as G_z in the logical coordinate system. A pulse sequence of slice selection is plotted in Figure 1-14.

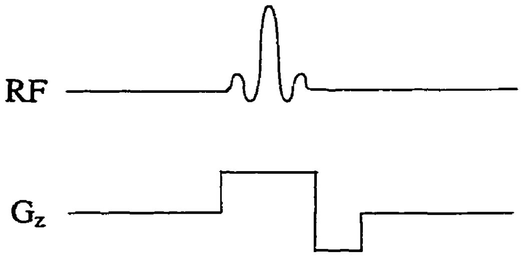

Figure 1-14 A pulse sequence for slice selection

As shown above, an RF pulse with a sinc waveform is applied when a slice selective gradient G_z is turned on. However, after the termination of the RF pulse, a negative gradient lobe is applied again. The reason for applying this negative lobe is to refocuse a linear phase dispersion across the slice thickness, see Figure 1-15.

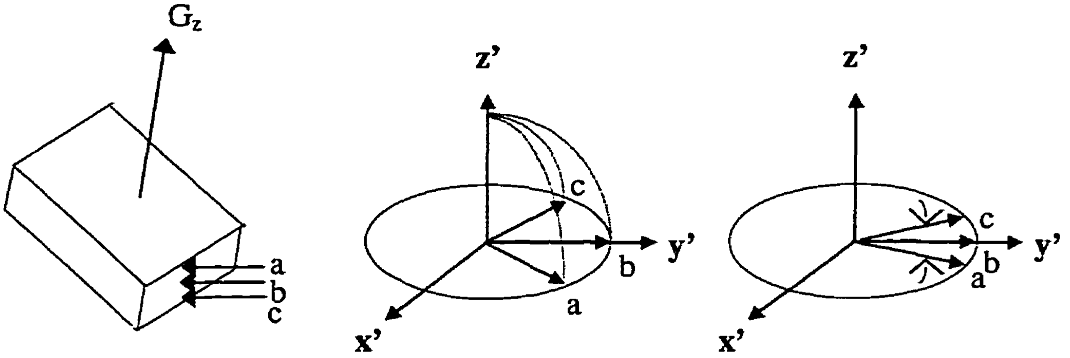

Figure 1-15 Dephasing and refocusing of the phase across the slice thickness viewed in the rotating frame

As shown in Figure 1-15, the spins at the top, middle, and bottom parts of the slice have different Larmor frequencies since they experience slightly different magnetic field strength caused by G_z. The spins are dephasing while they are being tipped away from the main field direction. The negative gradient lobe can bring the spins in phase. The area of the negative lobe should be about half of that of the positive lobe.

After a slice has been selected, the next task of imaging is to encode spatial information within the excited slice. Two distinctive processes are used for encoding the two dimensional information, which are frequency encoding and phase encoding. Frequency encoding will be discussed first, see Figure 1-16.

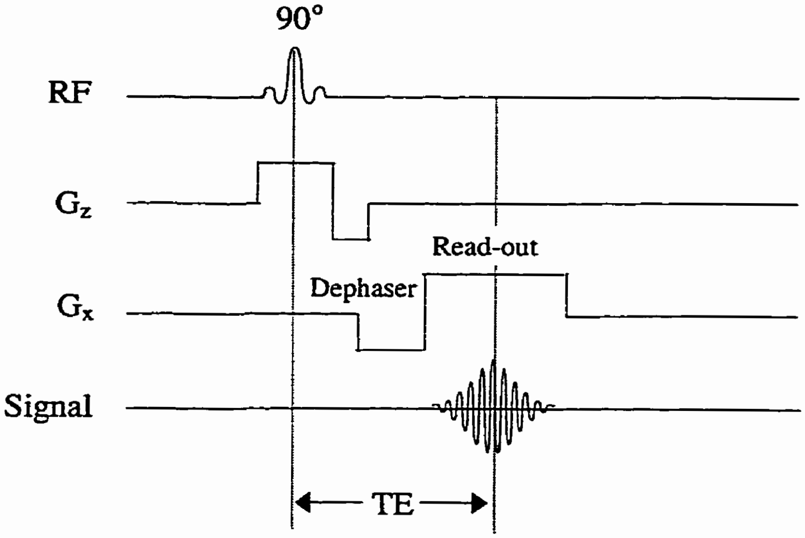

Figure 1-16 A pulse sequence for slice selection and frequency encoding

The frequency encoding gradient G_x is applied in the logical x direction and has a negative lobe called dephaser and a positive lobe called read-out. During the read-out period, the MR signal is sampled. The area of the dephasor is half of the area of the read-out gradient, so that the center of the echo is formed in the middle of the readout since all the spins will be refocused at the middle point. The time period from the center of the RF to the echo center is referred to as the time-of-echo (TE). During the read-out, the precessional frequencies of the spins vary linearly along the x direction. Therefore, spins at different x locations contribute to different frequencies in the MR signal. In other words, the spatial information x is encoded into the frequencies of the MR signal. A Fourier transform of the MR signal will give the x distributions of spins within the excited slice.

In order to encode 2D information into the MR signal, another gradient field G_y, called the phase encoding gradient, is used to make a systematic variation in the phase of the MR signals. A complete pulse sequence for gradient-echo imaging is shown in Figure 1-17.

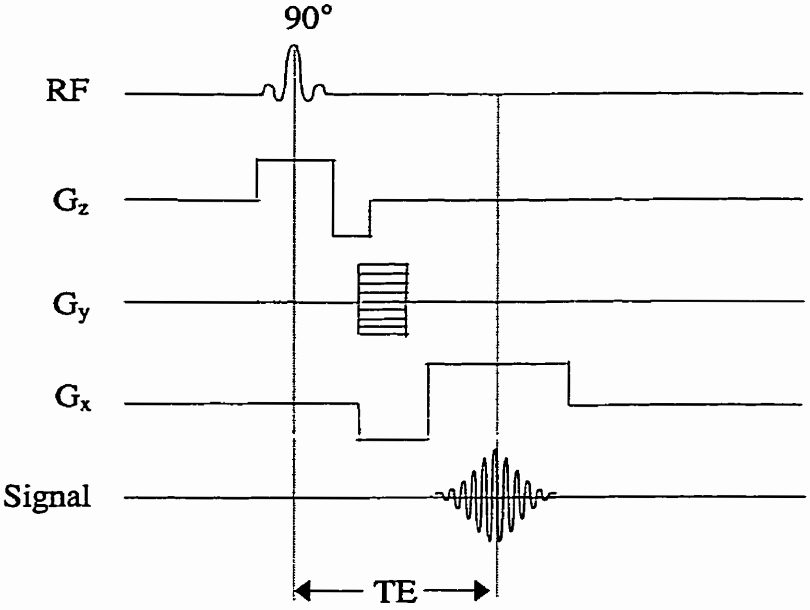

Figure 1-17 Pulse sequence for 2D gradient-echo imaging

In Figure 1-17, the only addition to the pulse sequence relative to that shown in Figure 1-16 is a single gradient G_y in the logical **y** direction. The complete pulse sequence is played out many times (typically 128 to 256 times) with the amplitude of G_y changing in a step-wise manner for each repetition. The time spent for each phase-encoding step is referred to as the time-of-repetition (TR). The MR signal sampled during each readout is stored in computer as one row of data. The number of rows for a whole dataset will be the same as the number of readouts or the number of phase encoding steps. Figure 1-18 (a) shows the magnitude of one such MR dataset. Since G_y is not turned on during the readout, it does not affect the precessional frequencies of the spins. However, spins at different y locations will have different phase twists or 'warps' due to G_y prior to each read-out. In other words, the spatial information y is encoded in the phase of the spins. Spin distribution in the y direction can be resolved from all the read-out signals by Fourier transforming the dataset in the y direction. Overall, a discrete 2D Fourier transform of the MR dataset will yield an MR image, which is a complex image. Figure 1-18 (b) shows the magnitude of the complex image.

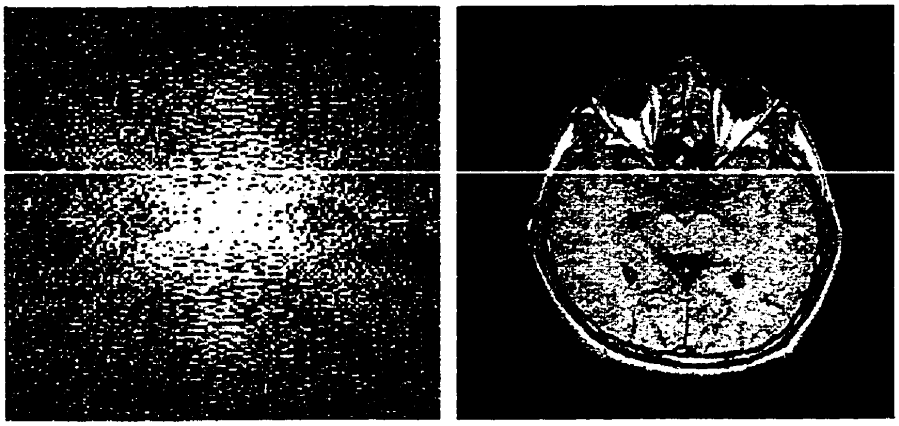

(a) (b)

Figure 1-18 (a) MR signal dataset (b) Reconstructed MR image

In order to illustrate the Fourier relation between a MR dataset and a MR image clearly, we give a more detailed derivation. We can label the demodulated MR signal as $S(t, G_y)$. According to equation (1-34), $S(t, G_y)$ is expressed as

$$\begin{aligned} S(t, G_y) &= \iint M_T(x, y)\exp[i\phi(x, y)]\,dxdy \\ &= \iint M_T(x, y)\exp[-i(\gamma x G_x)t - i(\gamma y G_y)\tau]\,dxdy \end{aligned} \tag{1-45}$$

where constant τ is the duration of phase-encoding gradient G_y. The T_1 and T_2 relaxations during signal acquisitions are ignored, thus the transverse magnetization magnitude $M_T(x, y)$ is not a function of time. If we introduce two new variables

$$\begin{aligned} k_x &= \gamma G_x t \\ k_y &= \gamma G_y \tau \end{aligned} \tag{1-46}$$

$S(t, G_y)$ can be considered as a function of k_x and k_y, i.e. $S(k_x, k_y)$, which is given by

$$\begin{aligned} S(k_x, k_y) &= \iint M_T(x, y) \exp[-i\gamma(G_x t)x - i\gamma(G_y \tau)y]\, dxdy \\ &= \iint M_T(x, y) \exp[-i(k_x x + k_y y)]\, dxdy \end{aligned} \tag{1-47}$$

It is clear that $S(k_x, k_y)$ is the 2D Fourier transform of $M_T(x, y)$. An MR image $M_T(x, y)$ can be obtained by performing an inverse 2D Fourier transform on $S(k_x, k_y)$

$$M_T(x, y) = \frac{1}{2\pi} \iint S(k_x, k_y) \exp[i(k_x x + k_y y)] dk_x dk_y \tag{1-48}$$

In practice, $S(k_x, k_y)$ is a set of discrete digital signals stored in the computer. A 2D discrete fast Fourier transform (FFT) is performed to reconstruct the image. k_x and k_y constitute a space called K-space, k_x and k_y stand for the wave numbers in the x and y directions and are 2π times the spatial frequencies ν_x and ν_y, respectively. A general vector **k** is defined as

$$\mathbf{k}(t) = \gamma \int_{-\infty}^{t} \mathbf{G}(t')dt' \tag{1-49}$$

and the signal $S[\mathbf{k}(t)]$ is written as

$$S[\mathbf{k}(t)] = \int M_T(\mathbf{r}) \exp[-i\, \mathbf{r} \cdot \mathbf{k}(t)]\, d^3\mathbf{r} \tag{1-50}$$

The raw MR data is nothing but some discrete points in **k** space. The above gradient-echo pulse sequence is scanning the **k** space line by line. There are different ways of scanning the K-space. As long as the K-space is covered by enough sampling points, an MR image can be reconstructed.

For the gradient-echo pulse sequence, the spins are refocused at the middle of the readout by the use of a negative gradient lobe. However, in the presence of main magnetic field inhomogeneity and chemical shifts, the spins can not be totally refocused at the middle of readout, resulting in a loss of image signal-to-noise ratio (SNR) and artifacts in the image. To overcome this problem, the spin-echo imaging pulse sequence can be used. A spin-echo pulse sequence is shown in Figure 1-19. The slice selective gradient G_z has the same amplitude during the 90° RF and the 180° RF so that only the selected slice effectively experience both of the RF pulses. On the G_x axis, the dephaser has a positive amplitude instead of a negative one because it is applied before the 180° RF pulse. The imaging procedure for the spin-echo pulse is similar to that of the gradient-echo pulse sequence. Nevertheless, the spin-echo sequence can refocuse the dephasing caused by field inhomogeneity and chemical shift, thus is superior in image quality but has a longer TE.

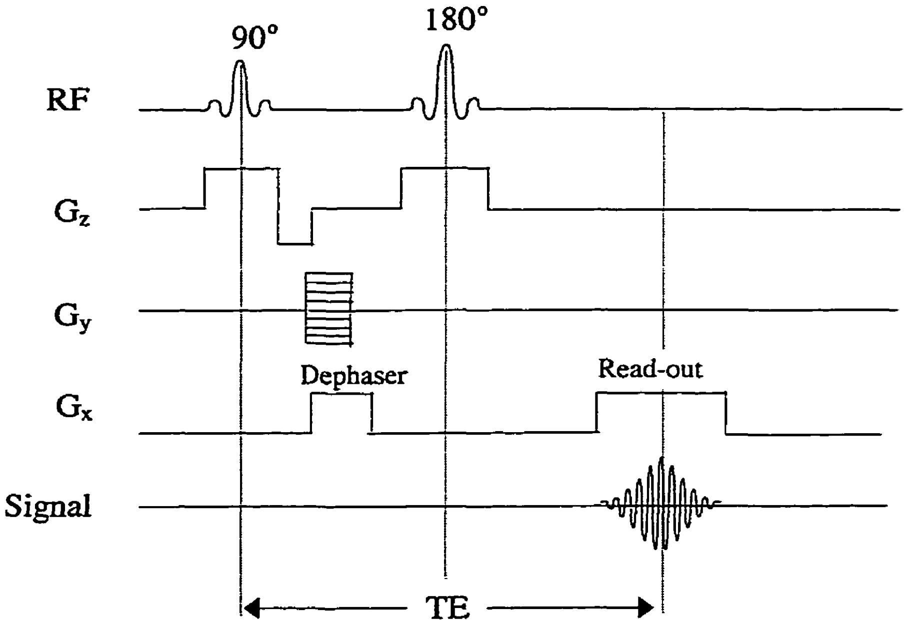

Figure 1-19 Pulse sequence for 2D spin-echo imaging

A gradient-echo pulse sequence for 3D imaging, as shown in Figure 1-20, can be derived from a 2D gradient-echo pulse sequence by replacing the slice selective gradient with another phase encoding in the Z-direction. The total number of readouts equals the number of phase encodings in y direction multiplied by the number of phase encodings in the z direction. Therefore, the imaging time is very long. However, this 3D imaging scheme, known as true 3D MRI, offers excellent spatial resolution in the third dimension and good SNR performance.

Generally, in gradient-echo sequences, the RF excitation pulse is not chosen to be 90° but a significantly smaller value, for example 30°. The reason for this reduced tip angle is to optimize the SNR when short TR is used for fast imaging [17].

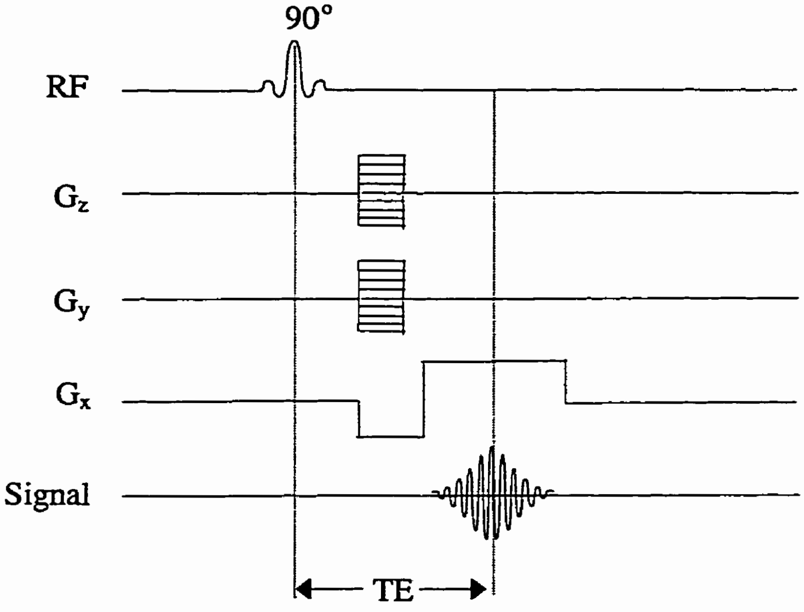

Figure 1-20 A gradient-echo pulse sequence for 3D imaging

In all the drawings of pulse sequences above, the gradients have been drawn as square waveforms. In reality, due to the limited inductance of gradient coils, the rising and falling edges of the gradient waveforms are digitally controlled to be linear ramps. A half-sinusoidal waveform is usually adopted for the phase-encoding gradient for the purpose of minimizing the quantization error of the gradient amplitude. A practical spin-echo pulse sequence is drawn in Figure 1-21.

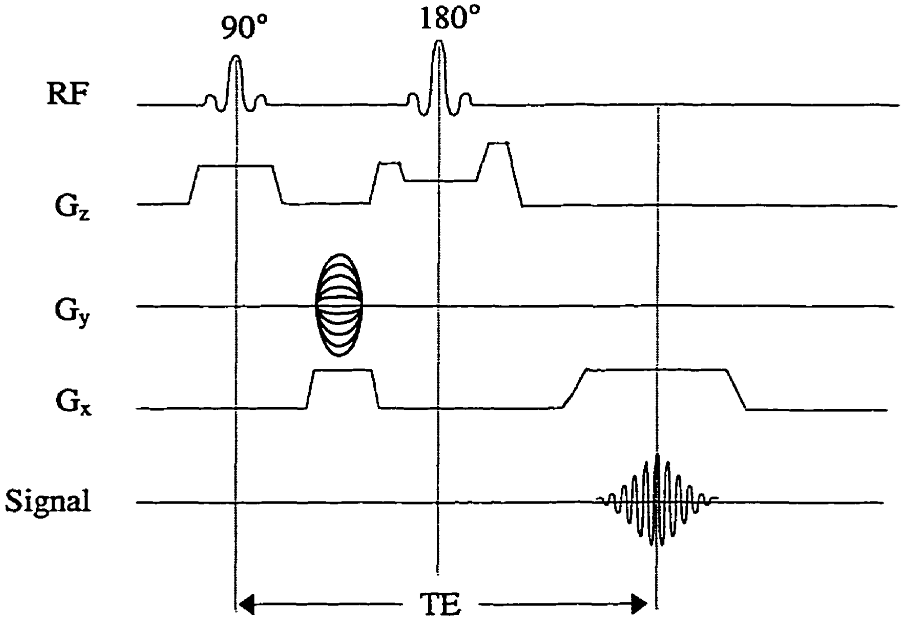

Figure 1-21 A practical spin-echo pulse sequence

It can be noticed that the negative refocusing lobe following the 90° RF is removed. To compensate this, the extra lobe on the right hand side of the 180° RF pulse is bigger than the one on the left-hand side. As long as the total area under the z gradient between the 90° pulse and data acquisition is zero, spins are in phase across the slice, provided that gradient before 180° pulse to be considered negative. The use of extra lobes on both sides of the 180° pulse is to destroy any signal contamination due to the imperfection of the 180° pulse.

Another imaging technique in daily scan practice is interleaved multi-slice acquisitions. As we know, TR is usually much longer compared to TE due to a long time period needed for the recovery of the longitudinal magnetization governed by the T_1 relaxation. Hence, for each readout, i.e. a phase encoding step, there is a long "dead time”. This “dead time” allows the imaging hardware to do slice selection, phase encoding and readout for other slices. Therefore, multi-slices can be simultaneously imaged during the time needed for a single slice. 2D multi-slice acquisitions can offer 3D information by stacking the 2D images into a 3D image. The speed of 2D multi-slice acquisitions is fast compared to a true 3D sequence, but the resolution in the third dimension is poor since the slice thickness can not be too thin due to limited SNR and imperfect slice profile.

CHAPTER 2

REVIEW OF WATER-FAT IMAGING TECHNIQUES

2.1 Introduction to Chemical Shift Imaging

For conventional proton MR imaging, the signal intensity recorded for each voxel is a weighted average of the signal contribution from several distinct proton species. This conventional approach produces images characterized by excellent spatial resolution and image SNR, but at the expense of reduced chemical information. On the other hand, NMR spectroscopy provides excellent chemical shift information but almost no spatial information. In some applications, one may want to have both spatial resolution and chemical shift information. This is the main motivation of the development of chemical shift imaging (CSI) techniques.

CSI was originally proposed in 1982 by Brown *et al* [18]. Maudsley *et al* suggested a similar procedure in 1983 [19]. In contrast to conventional MR imaging techniques, this CSI technique eliminates the readout gradient and uses the frequency encoding to acquire the chemical shift information, as in an NMR spectroscopy experiment. To compensate for the loss of spatial encoding in the frequency direction, a phase-encoding in this direction is added. A typical CSI sequence is shown below.

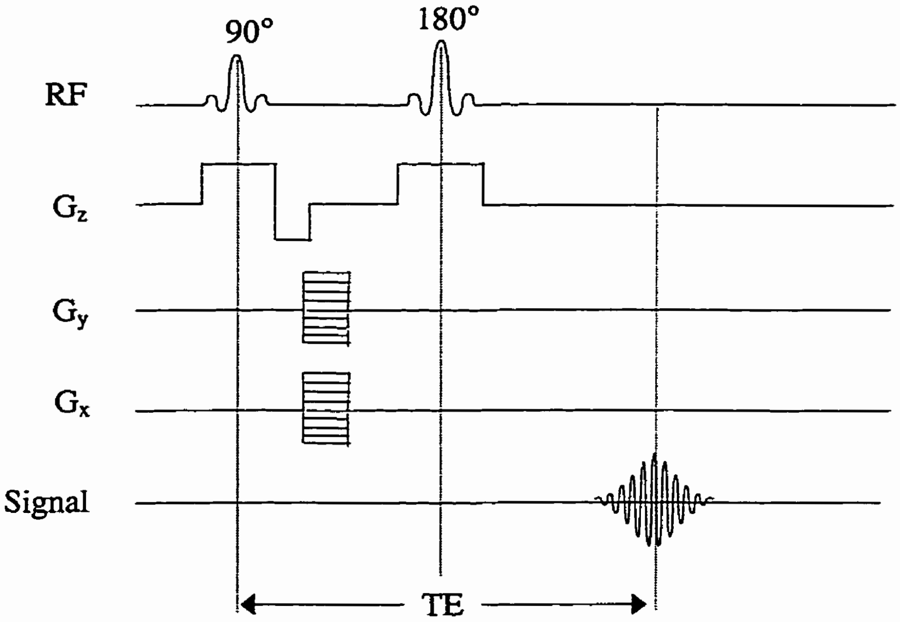

Figure 2-1 A CSI pulse sequence

The dataset acquired from this sequence is composed of $N_x \times N_y$ readouts, where N_x and N_y are the number of phase-encoding steps in the x and y directions, respectively. This dataset can be considered as being three dimensional, the readout being one dimension in time and the two phase-encodings being two dimensions in **k** space. Hence, the MR data can be written as $S(k_x, k_y, t)$. What we want to get from a CSI experiment is the magnetization distribution $M_T(x, y, \omega)$ which is a function of spatial location (x, y) and chemical shift measured by frequency ω of the proton species in the rotating frame. The MR signal is related to the magnetization distribution by

$$S(k_x, k_y, t) = \iiint M_T(x, y, \omega)\exp(-ik_x x)\exp(-ik_y y)\exp(-i\omega t)\, dxdyd\omega \qquad (2\text{-}1)$$

It is clear that the data $S(k_x, k_y, t)$ is the 3D FT of the magnetization distribution $M_T(x, y, \omega)$. Hence, a 3D inverse FT of $S(k_x, k_y, t)$ yields $M_T(x, y, \omega)$

$$M_T(x,y,\omega) = \frac{1}{(2\pi)^3} \iiint S(k_x, k_y, t) \exp(ik_x x) \exp(ik_y y) \exp(i\omega t)\, dk_x dk_y dt \qquad (2\text{-}2)$$

The result is composed of $N_x \times N_y$ spectra, each of which is associated with one pixel in the 2D image. A common way to display the result is to construct separate images for different proton species, i.e. to identify the peaks in the spectra and construct images corresponding to the peaks. Because of magnetic field inhomogeneity, the spectra for different pixels may have relative frequency shifts. Moreover, the spectra usually have non-zero baselines and very low SNR. These make the image constructions not straightforward. Because the amount of data is huge, an automatic procedure is required to do the peak identification, peak quantification, and baseline estimation. The whole procedure is very time consuming and not reliable. In addition to data processing problems, the imaging time is another concern. If the number of phase-encoding steps in x and y dimensions are both 128, and TR is 500 ms, then the total imaging time will be $128 \times 128 \times 500\text{ms}$, i.e. 136 minutes. In order to reduce imaging time, we have to sacrifice the spatial resolution by reducing the number of phase-encoding steps. A number of 16×16 phase-encoding steps is typically used, which takes about 2 minutes to do one scan. Reduced spatial resolution not only loses anatomical details but also causes some other problems. When each voxel becomes bigger, the field inhomogeneity per pixel becomes larger and the spectral resolution will be degraded. When **k** space coverage becomes smaller, truncation artifacts in the images will be more severe. Partial-volume artifacts will also be worsened when voxels become larger. All these problems are great impediments to the practical application of the conventional FT based CSI methods.

2.2 Early Water-Fat Imaging Methods

In the last decade or so, a lot of effort has been concentrated on water-fat chemical shift imaging due to the fact that most of the signal contributing to the MR images of the human body comes from water protons and fat (lipid methylene) protons. Signals from other proton species are so much smaller that they cannot be observed without special effort. The Larmor frequency of water is measured to be about 3.5 ppm higher than that of fat. At a magnetic field of 1.5 Tesla, the Larmor frequency difference between water and fat is about 220 Hz. Hence, in every 4.5 ms, the transverse magnetization vector of water will rotate one full cycle relative to the magnetization vector of fat. A water-fat spectrum is schematically illustrated in Figure 2-2.

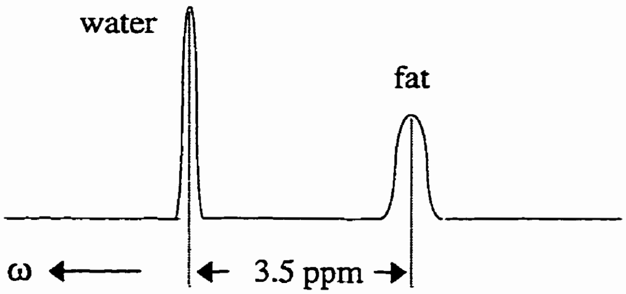

Figure 2-2 Sketch of proton chemical shift spectrum

The use of FT based CSI methods on water-fat proton spectrum was first reported by Rosen *et al* [20]. Despite the early interest in this technique, this CSI method is not widely incorporated into clinical imaging because of the reasons we pointed out in the previous section.

Another way to exploit the chemical shift between water and fat is known as fat-suppression or water-suppression. In these methods, narrow-bandwidth RF pulses are used prior to the image acquisition to suppress the signal from fat (or water), allowing the other chemical component to be imaged separately. In clinical imaging, fat suppression is more frequently used to suppress the strong signal from fatty tissues for an improved image contrast. An example of fat suppression pulse sequence can be described as follows. First, a narrow-bandwidth RF pulse tuned at fat resonance is used to rotate the fat magnetization vector 90° into the transverse plane. Then a spoiling gradient is immediately applied to disperse the transverse magnetization vector so that the net transverse magnetization is averaged to zero. The unexcited water magnetization remains in the z axis and is subsequently imaged using a conventional imaging pulse sequence. The images with fat-suppression are often damaged to some degree by field inhomogeneity. This is because spatial variations of the field will cause the resonance frequencies of fat vary spatially. When the field spatial variations are greater than the chemical shift between water and fat (3.5 ppm), water and fat resonance frequencies in the whole field-of-view (FOV) will be mixed together. As a result, fat cannot be selectively suppressed uniformly in the whole FOV. Therefore, very high B_0 homogeneity is required for fat-suppression. However, even if the original B_0 field is perfectly homogeneous, once the patient is inserted, there can be significant induced field variations due to the magnetic susceptibility variations in the tissues. Usually, magnetic field shimming is performed after the patient is inserted and before scanning. However, the success of shimming is often limited to a small localized region.

In 1984, Sepponen *et al* proposed a new method for water-fat CSI, in which the spectral information is phase-encoded instead of being frequency-encoded [21]. The imaging time can be shortened using this method. The pulse sequence is shown in Figure 2-3.

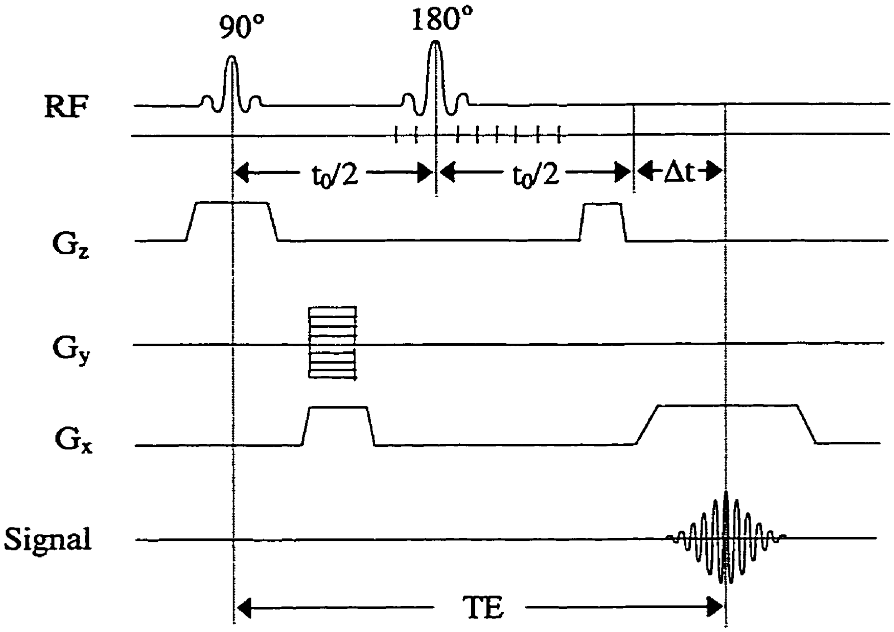

Figure 2-3 Pulse sequence for Sepponen's water-fat imaging method

For each phase-encoding step, a series of acquisitions are performed with a fixed TE but varying time intervals between the 90° and 180° pulses. According to spin-echo principles, all the spectral components at the same spatial location will refocus at time t_0 which is twice the time interval between the 90° and 180° pulses. At time TE, the spectral component with angular frequency ω in the rotating frame will acquire a phase approximately being $\omega\Delta t$, where Δt is the time difference between TE and t_0. In the above calculation, the effects of the phase-encoding gradient and readout gradient on the Larmor frequency of the chemical component were ignored since the gradient fields are several orders smaller than the main magnetic field. Therefore, the spectral encoding depends only on Δt and can be separated from spatial encodings. In each phase-encoding step, every acquisition scans one **k** space line at the same **k** space location for a different spin-echo image. After all the phase-encoding steps, a series of datasets are acquired and the corresponding spin-echo images are reconstructed by simply performing 2D FT on the datasets separately. These reconstructed complex valued images have the same spatial information but different phase-encodings of spectral components. A 1D FT of all the images in the third dimension will yield a train of 2D images along the chemical shift axis, see Figure 2-4.

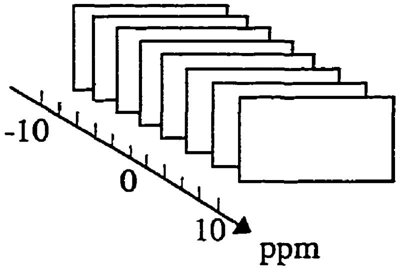

Figure 2-4 A train of chemical shift images

In the experiment described in the literature [21], 16 images in the spectral direction were scanned. The spectral resolution is 2.4 ppm. Hence, water and fat can be roughly distinguished since their chemical shift difference is 3.5 ppm. The spectral information is phase encoded by shifting the 180° refocusing pulse and makes it possible to reduce imaging time by sacrificing spectral resolution. Due to the poor spectral resolution, truncation artifacts and partial volume artifacts are very severe in the spectral direction.

In the same year of 1984, Dixon published his famous paper [22]. In his method, the spectral information is also encoded by shifting the 180° refocusing pulse, same as in Sepponen's method. However, rather than acquiring multiple phase offset images, only a pair of images were collected in Dixon's approach, see Figure 2-5.

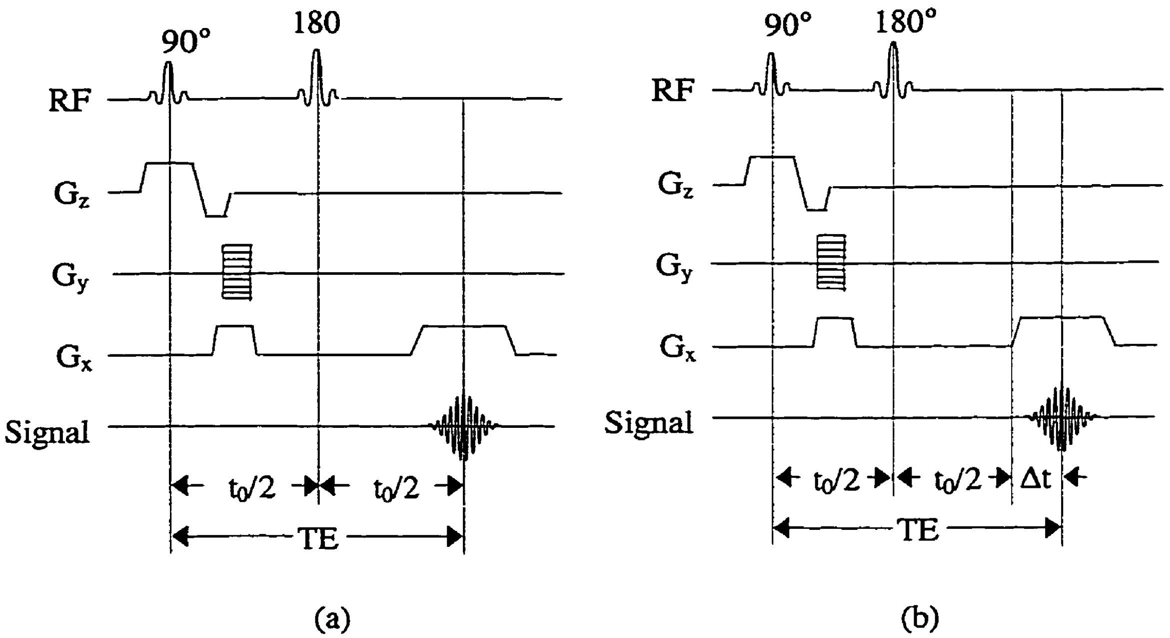

Figure 2-5 Dixon method for water-fat imaging (a) Pulse sequence for the in-phase image (b) Pulse sequence for the opposed-phase image

The first image of the pair, usually called an in-phase image, is a conventional spin-echo acquisition with normal timing of the 180° refocusing pulse. The transverse magnetization vectors of water and fat are aligned in the same direction for all the pixels in the image. The second image of the pair, usually called an opposed-phase image, is acquired with the 180° refocusing pulse shifted 5ms earlier for a 0.35T scanner so that the transverse magnetization vectors of water and fat are in opposite directions. Simple addition of the two complex images would yield an image of water and simple subtraction of the two images would yield an image of fat. The Dixon method is a milestone in simple proton chemical shift imaging since it is the first model based CSI method. Dixon actually modeled the proton spectrum as two δ-function shaped peaks with one peak being water and the other being fat. The chemical shift between the two peaks is a known value from spectroscopy experiments, which is 3.5ppm. This known chemical shift value was used to determine the time shift of the 180° refocusing pulse for the opposed-phase image. This is the key to the high imaging efficiency for Dixon method.

As Dixon pointed out himself in his original paper [22], the worst problem with his method comes from magnetic field inhomogeneities which, over a whole image, are many times as large as the chemical shift difference between water and fat. A pair of water and fat images reconstructed with the Dixon method is shown in Figure 2-6. Because of off-resonance and field inhomogeneity errors, water and fat are not successfully separated. Another disadvantage with the original Dixon pulse sequence is that patient motion between the two independent scans is translated into spatial misregistration artifacts. This problem can be largely overcome by interleaving the two acquisitions in each phase-encoding step, similar to Sepponen's method.

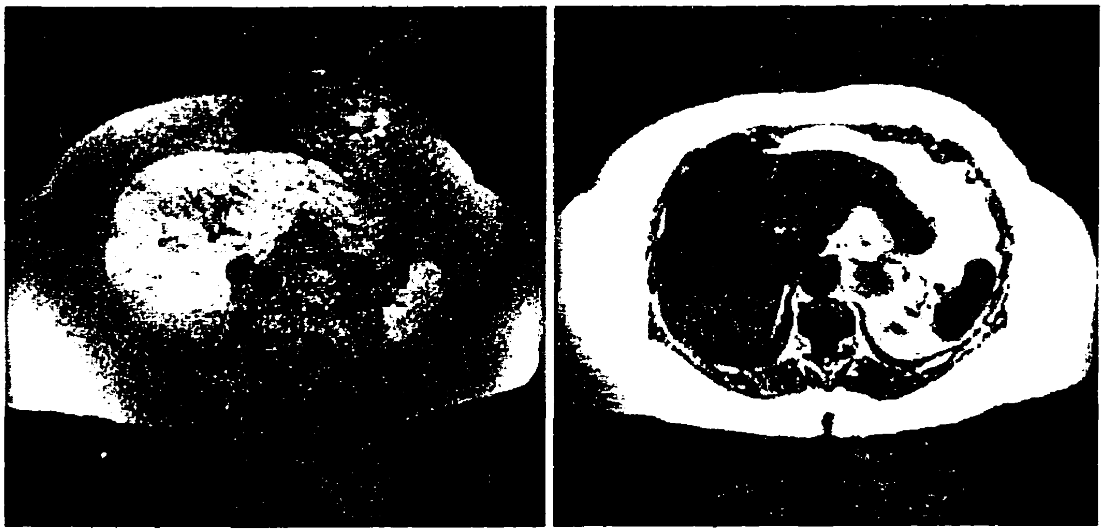

(a) (b)

Figure 2-6 Transverse water (a) and fat (b) images of the abdomen, reconstructed with the Dixon method.

2.3 General Phase Behavior of Water and Fat Magnetization Vectors

After Dixon's original work, the theory of the general phase behavior of water and fat were gradually developed. In this section, we will systematically analyze the general phase behavior of water and fat magnetization vectors.

In the presence of a main magnetic field B_0 with inhomogeneity $\Delta B_0(x,y)$, the transverse magnetization vector of water, **W**(x,y), and of fat, **F**(x,y), will rotate clockwise at angular velocities of $\gamma_W[B_0+\Delta B_0(x,y)]$, and $\gamma_F[B_0+\Delta B_0(x,y)]$, respectively, where γ_W is the gyro-magnetic ratio for water and γ_F for fat. As we know, the rotating frame of reference is usually selected to be rotating at the center frequency of RF pulse. If we tune the RF center frequency at the Larmor frequency of water, the rotating frame will rotate clockwise at an angular velocity of $\gamma_W B_0$. For a pulse sequence with shifted 180°RF refocusing pulse, as shown in Figure 2-5 (b), the MR signal is the sum of contributions from water and fat magnetization vectors in the rotating frame and can be expressed as

$$\begin{aligned}
S(t,G_y,\Delta t) &= \iint W(x,y)\exp\left\{-i\int \gamma_W[B_0+\Delta B_0(x,y)+\mathbf{G}\cdot\mathbf{r}]-\gamma_W B_0\,dt\right\} \\
&\qquad + F(x,y)\exp\left\{-i\int \gamma_F[B_0+\Delta B_0(x,y)+\mathbf{G}\cdot\mathbf{r}]-\gamma_W B_0\,dt\right\}dxdy \\
&= \iint W(x,y)\exp\left\{-i[\gamma_W\Delta B_0(x,y)(t+\Delta t)+\gamma_W G_x xt+\gamma_W G_y y\tau]\right\} \\
&\qquad + F(x,y)\exp\left\{\begin{matrix}-i[(\gamma_F-\gamma_W)B_0(t+\Delta t) \\ +\gamma_F\Delta B_0(x,y)(t+\Delta t)+\gamma_F G_x xt+\gamma_F G_y y\tau\end{matrix}\right\}dxdy \qquad (2\text{-}3) \\
&= \iint \{W(x,y)+F(x,y)\exp[i(\gamma_W-\gamma_F)B_0(t+\Delta t)] \\
&\qquad \exp[-i(\gamma_F-\gamma_W)\Delta B_0(x,y)(t+\Delta t)-i(\gamma_F-\gamma_W)G_x xt-i(\gamma_F-\gamma_W)G_y y\tau]\} \\
&\qquad \exp[-i\gamma_W\Delta B_0(x,y)\Delta t]\exp[-i(\gamma_W G_x xt+\gamma_W G_y y\tau)]\exp[-i\gamma_W\Delta B_0(x,y)t]dxdy
\end{aligned}$$

The term $\exp[-i(\gamma_F-\gamma_W)\Delta B_0(x,y)(t+\Delta t)-i(\gamma_F-\gamma_W)G_x xt-i(\gamma_F-\gamma_W)G_y y\tau]$ can be approximated to 1 since all the phase terms inside the exponential are extremely small.

The last term in the above equation, $\exp[-i\gamma_W \Delta B_0(x,y)t]$, will result in a small spatial shift and distortion of the image as in any spin-warp imaging modality. This term works on water and fat the same way and will not affect the water-fat chemical shift result, subsequently, it is not our concern here and is ignored. The term $(\gamma_W - \gamma_F)B_0$ is the chemical shift between water and fat, it can be labeled by $\Delta\omega$. The above equation can be simplified as

$$\begin{aligned} S(t,G_y,\Delta t) &= \iint [W(x,y) + F(x,y)\exp(i\Delta\omega\Delta t)\exp(i\Delta\omega\, t)]\exp[-i\gamma_W \Delta B_0(x,y)\Delta t] \\ &\qquad \exp[-i(\gamma_W G_x x t + \gamma_W G_y y \tau)]dxdy \\ &= \iint \{W(x,y) + F(x,y)\exp(i\Delta\omega\Delta t)\exp[ik_x(\Delta\omega / \gamma_W G_x)]\} \\ &\qquad \exp[-i\gamma_W \Delta B_0(x,y)\Delta t]\exp[-i(k_x x + k_y y)]dxdy \end{aligned} \tag{2-4}$$

where $k_x = \gamma_W G_x t$ and $k_y = \gamma_W \tau G_y$. The reconstructed spin-echo image I(x,y) is the inverse Fourier transformation of $S(t,G_y,\Delta t)$,

$$I(x,y) = \frac{1}{2\pi^2}\iint S(t,G_y,\Delta t)\exp[i(k_x x + k_y y)]dk_x dk_y \tag{2-5}$$

that can be proved to be

$$I(x,y) = [W(x,y) + F(x - \Delta\omega / (\gamma_W G_x),\ y)\exp(i\Delta\omega\Delta t)]\exp[-i\gamma_W \Delta B_0(x,y)\Delta t] \tag{2-6}$$

We can notice that water and fat has a small relative spatial shift of $\Delta\omega / (\gamma_W G_x)$ in the frequency encoding direction. Consider a main field strength of 1.5 T and a readout gradient of 0.4 Gauss/cm, the value of the shift equals 1.3 mm, which usually corresponds to one to two pixels in the image. There is also another relative shift between water and fat in the slice selection direction, with value of $\Delta\omega / \gamma_W G_z$. These misregistrations are usually small for water-fat imaging and could be ignored. Due to phase offset resulting from RF penetration effects and other systematic phase shifts such as data sampling window off-centering, another phase term exp[iΦ(x,y)] is multiplied to I(x,y), So I(x,y) can be written as [28-32]

$$I(x,y) = [W(x,y) + F(x,y)\exp(i\alpha)]\exp(i\Phi)\exp(i\Theta) \tag{2-7}$$

where $\alpha = \Delta\omega\Delta t$, $\Theta = -\gamma_w \Delta B_0(x,y)\Delta t$. α is the phase angle between W and F due to chemical shift effect. Θ is the phase error due to magnetic field inhomogeneity. Both α and Θ are proportional to the time shift Δt. Φ does not change with time shift Δt. Equation (2-7) is the master equation for the general phase behavior of water and fat in a complex image.

In the Dixon method, a pair of images $I_1(x,y)$ and $I_2(x,y)$ are acquired with α equals 0 (in-phase) and π (opposed-phase) respectively. This sampling scheme is labeled as $(0,\pi)$ or $(0, 180°)$ according to the angle between the **W** and **F** vectors. The differential Larmor frequency between water and fat $\Delta\omega$ is 3.5 ppm of the resonance frequency. At a field strength of 1.5 T, the resonance frequency is 63.9 MHz and the Larmor frequency difference between water and fat is 224 Hz. Hence, Δt needs to be 0 and 2.24 ms to make **W** and **F** in-phase and opposed-phase. The two images can be written as

$$\begin{aligned} I_1 &= (W + F)\exp(i\Phi) \\ I_2 &= (W - F)\exp(i\Phi)\exp(i\Theta) \end{aligned} \tag{2-8}$$

If the magnetic field is perfectly homogeneous, the phase error Θ will be zero everywhere. Then, the term $\exp(i\Theta)$ is a constant 1. The water image W and fat image F can be simply solved by

$$\begin{aligned} W &= | I_1 + I_2 | / 2 \\ F &= | I_1 - I_2 | / 2 \end{aligned} \tag{2-9}$$

When the field inhomogeneity term $\exp(i\Theta)$ is too large to be ignored, we cannot get a correct water-fat result from Dixon method.

2.4 Water-Fat Imaging with Single Quadrature Sampling

Shortly after Dixon's original work, a new water-fat imaging method was proposed by several authors [23-25]. This method acquires only a single image with the magnetization vectors of water and fat placed orthogonal to each other by properly setting the time shift Δt. The complex image can be written as

$$I_1 = (W + iF)\exp(i\Psi) \qquad (2\text{-}10)$$

where Ψ comprises all the phase errors. If Ψ is small enough to be ignored, W will be the real part of I_1 and F will be the imaginary part of I_1. So ideally, water and fat can be separated and distinguished by a single image acquisition. However, the phase errors cannot be ignored in most cases, which prevents a clean separation of water and fat. Although a phase correction method has been proposed [26] and there is a renewed interest in this approach [27], this method is still not clinically feasible. The main difficulty lies in the lack of information necessary for phase correction. Despite the problems caused by phase errors, this asymmetric sampling scheme points to later developments of water-fat imaging methods.

2.5 Variations of Dixon method

In the last decade, many methods have been proposed to correct the field inhomogeneity problem by using additional data acquisitions [28-36] to sample the water and fat vectors at angles of multiple of π radians. Among these methods, a representative sampling scheme is $(-\pi, 0, \pi)$ [31]. Three complex images $I_1(x,y)$, $I_2(x,y)$, and $I_3(x,y)$ are acquired with Δt being $-\tau$, 0, and τ respectively, where τ is set to satisfy $\Delta\omega\tau = \pi$. The acquired images can be written as

$$\begin{aligned} I_1 &= (W - F)\exp(i\Phi)\exp(-i\Theta) \\ I_2 &= (W + F)\exp(i\Phi) \\ I_3 &= (W - F)\exp(i\Phi)\exp(i\Theta) \end{aligned} \tag{2-11}$$

where Θ is given by $\Theta = -\gamma\Delta B_0\tau$. Because W and F should have positive real values, the phase error term $\exp(i\Phi)$ is actually the phasor of I_2, where the phasor of a complex number can be calculated by normalizing the magnitude of the complex number to unit 1. Phase corrected images I_1', I_2', I_3' are obtained after $\exp(i\Phi)$ are removed from I_1, I_2 and I_3, respectively

$$\begin{aligned} I_1' &= (W - F)\exp(-i\Theta) \\ I_2' &= (W + F) \\ I_3' &= (W - F)\exp(i\Theta) \end{aligned} \tag{2-12}$$

The solutions of W and F are given by

$$\begin{aligned} W &= \frac{1}{2}(I_2' + p\sqrt{I_1' I_3'}) \\ F &= \frac{1}{2}(I_2' - p\sqrt{I_1' I_3'}) \end{aligned} \tag{2-13}$$

where $p = \pm 1$ is a switch function which contains the sign of the square root. For each pixel, there is an ambiguity between W and F due to the sign of p. To solve this problem, the following procedure is adopted. It is straightforward to see that

$$I_3' I_1'^{*} = (W - F)^2 \exp(i2\Theta) \tag{2-14}$$

where "*" represents the complex conjugate of a complex number. The principle value of the phase angle 2Θ can be calculated by

$$(2\Theta)_{\text{principle value}} = \arg(I_3' I_1'^{*}) \qquad (2\text{-}15)$$

where the operator "arg" returns the phase angle, within $(-\pi, \pi)$, of a complex number. When $|2\Theta|$ is less than π, 2Θ is the same as its principle value. When $|2\Theta|$ is larger than π, 2Θ cannot be uniquely determined as the argument of $I_3' I_1'^{*}$ because it can have a multiple of 2π difference. Phase unwrapping techniques are needed to obtain the 2Θ map, which will be discussed in the next section. After 2Θ is known, Θ is simply obtained as half of 2Θ. When $\arg[I_1'\exp(i\Theta)]$ equals 0, W is larger than F, p should be 1; When $\arg[I_1'\exp(i\Theta)]$ equals π, W is smaller than F, p should be -1. After p is determined for every pixel, water and fat images are successfully separated. One problem with this method is that 2Θ is undetermined for voxels containing identical amounts of water and fat because of signal cancellation on the two opposed-phase images which were used to calculate 2Θ. In order to overcome this problem, a similar method with a sampling scheme of $(0,\pi,2\pi)$ was proposed [32]. In the $(0,\pi,2\pi)$ scheme, the first and third images are both water fat in-phase images. However, compared to the first image, the third image has an extra term $\exp(2\Theta)$ due to field inhomogeneity. Therefore, $\exp(2\Theta)$ can be easily obtained by multiplying the complex conjugate of the first image to the third image. Because the first and third images are both in-phase images, there is no phase indetermination problem.

We [37] and others [38-43] have found that the third image in the $(-\pi, 0, \pi)$ scheme is very much redundant except for some gain in SNR. This can be seen from equation (2-12), where I_3' is simply the complex conjugate of I_1'. The third image in a $(0,\pi,2\pi)$

scheme also has this redundancy even though it can provide some information on relaxation effects and avoid 2Θ indetermination problem for some pixels. In fact, the original 2-point Dixon method can provide us almost the same amount of information as the (-π, 0, π) method does. It can be seen from equation (2-8), a wrapped 2Θ map can be obtained by

$$(2\Theta)_{\text{principle value}} = \arg[(I_2 I_1^*)^2] \qquad (2\text{-}16)$$

Similar to the previous 3-point method, successful phase unwrapping is needed to get a unique answer of Θ.

2.6 Introduction to Phase Unwrapping Techniques

The argument of a complex number is defined within a range of 2π radians, typically from -π to +π. As a result, the argument of a complex number can only represent the principle value of a phase angle. Phase wrap or phase aliasing occurs if the absolute value of the phase angle is greater than π. For example, in the previous discussion, phase error 2Θ is caused by field inhomogeneity and it can be larger than π or smaller than -π. However, the principle value of 2Θ, calculated by $(2\Theta)_{\text{principle value}} = \arg(I_3' I_1'^*)$, is limited in the range from -π to +π, and it can have a multiple of 2π difference from the real phase value of 2Θ. To obtain the real phase map from a wrapped phase map is called phase unwrapping. Figure 2-7 shows a wrapped 2Θ map and the corresponding unwrapped phase map.

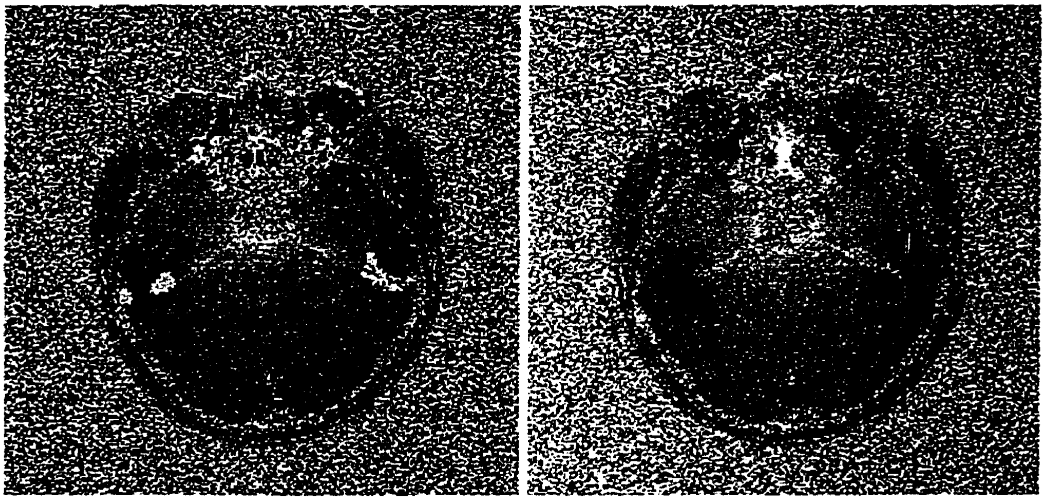

(a) (b)

Figure 2-7 (a) A wrapped 2Θ phase map (b) The unwrapped 2Θ phase map

Phase unwrapping is still a new topic in MRI, but it has been actively developed for a long time in other areas such as optical engineering and radar signal processing [44]. Some of the phase unwrapping methods used in MRI and other areas are listed below:

- Phase unwrapping by polynomial fitting [31,45]
- Simple region growing phase unwrapping [33,39,40]
- Phase fringe counting / scanning approach to phase unwrapping [46]
- Cellular automata method for phase unwrapping [47]
- Noise-immune cut methods of phase unwrapping [48]
- Flood phase unwrapping algorithm [49]
- Phase unwrapping by regions [50]
- Temporal phase unwrapping [51-53]
- Iterative least-squares phase unwrapping methods [54,55,41]

- Phase unwrapping using a priori knowledge about the band limits of a function [56]
- Minimum spanning tree methods [57]
- Phase unwrapping based on dipole connections [58]

For water-fat imaging, polynomial fitting [31], simple region growing [33,39,40], and iterative least-squares phase unwrapping methods [41] have been used. Instead of analyzing these phase unwrapping methods, we will discuss some basic theory of phase unwrapping in order to understand the limitations of phase unwrapping.

The difficulty of phase unwrapping lies in the existence of 'poles' [58] or "isolated zero points" [54]. Given a wrapped phase map $\phi_w(x,y)$, a pole criterion c(x,y) is defined as the sum of wrapped phase differences around a 2×2 pixel loop

$$\begin{aligned} c(x,y) = & W[\phi_w(x+1,y)-\phi_w(x,y)] + W[\phi_w(x+1,y+1)-\phi_w(x+1,y)] \\ & + W[\phi_w(x,y+1)-\phi_w(x+1,y+1)] + W[\phi_w(x,y)-\phi_w(x,y+1)] \end{aligned} \tag{2-17}$$

where the wrapping operator "W" represents taking the principle value of a phase angle. Since the result of the subtraction of two wrapped phase angles is between -2π and 2π, $W(\Delta\phi)$ can be simply calculated by

$$W(\Delta\phi) = \begin{cases} \Delta\phi + 2\pi & \text{if}\, \Delta\phi < -\pi \\ \Delta\phi - 2\pi & \text{if}\, \Delta\phi > \pi \\ \Delta\phi & \text{otherwise} \end{cases} \tag{2-18}$$

where $\Delta\phi$ is a phase angle in the range of -2π to 2π. The pole criterion c(x,y) has three possible values: 0, 2π, or -2π. If c(x,y) equals 0, pixel (x,y) is not a pole; If c(x,y) equals 2π, pixel (x,y) is a positive pole; If c(x,y) equals -2π, pixel (x,y) is a negative pole. Another useful concept in phase unwrapping is the phase gradient map **G**(x,y) [54], whose two components $G_x(x,y)$ and $G_y(x,y)$ are defined as

$$\begin{aligned} G_x(x,y) &= \frac{\partial \phi_w}{\partial x} = W[\phi_w(x+1,y) - \phi_w(x,y)] \\ G_y(x,y) &= \frac{\partial \phi_w}{\partial y} = W[\phi_w(x,y+1) - \phi_w(x,y)] \end{aligned} \qquad (2\text{-}19)$$

The curl of the 2D map **G**(x,y) is in the z direction and can be calculated by

$$\begin{aligned} [\nabla \times \mathbf{G}(x,y)]_z &= \frac{\partial G_y}{\partial x} - \frac{\partial G_x}{\partial y} \\ &= [G_y(x+1,y) - G_y(x,y)] - [G_x(x,y+1) - G_x(x,y)] \end{aligned} \qquad (2\text{-}20)$$

Substituting the definitions of G_x and G_y into equation (2-20), it is easy to prove that

$$c(x,y) = [\nabla \times \mathbf{G}(x,y)]_z \qquad (2\text{-}21)$$

Therefore the pole criterion c(x,y) is nothing but the curl of the phase gradient map. Being a vector field, **G**(x,y) satisfies

$$\oint \mathbf{G}(x,y) \cdot d\mathbf{l} = \iint [\nabla \times \mathbf{G}(x,y)] \cdot d\mathbf{A} = \iint c(x,y)dA \qquad (2\text{-}22)$$

where **dl** is a unit step from one pixel to a neighbouring pixel in the horizontal or vertial direction; dA is a unit area. The above equation means that the integral of phase gradient along any closed path equals the sum of pole values in the region enclosed by the path. If the integral equals zero, it means there are no net poles in the region, i.e. there are no poles or the number of positive poles and the number of negative poles are equal in the region. If there is no pole in the wrapped phase map, the curl of the gradient map **G**(x,y) is zero everywhere. Therefore, **G**(x,y) is a conservative vector field and a potential ϕ(x,y) can be defined as

$$\phi(x,y) = \int_{(x_0,y_0)}^{(x,y)} \mathbf{G}(x,y) \cdot d\mathbf{l} \qquad (2\text{-}23)$$

where (x_0, y_0) is the initial point. The potential $\phi(x,y)$ is in fact the unwrapped phase map of $\phi_w(x,y)$. Therefore, phase unwrapping for a wrapped phase map without any poles is straightforward. In reality, however, the wrapped phase maps usually have poles, which means the curl of the **G**(x,y) has non-zero points. Consequently, **G**(x,y) is not a conservative field and no potential can be defined in the whole field since the above integration will be dependent on the integral path. However, a potential can still be defined in a region that has no poles and it does not enclose any inner region that has net poles.

There are two kinds of poles in a wrapped phase map. The first kind of poles are in the background noise. If the noise distribution in a phase map is uniform, it can be proved that 1/6 of the noise pixels are positive poles and 1/6 negative poles. These poles in the noise pose a lot of difficulties to phase unwrapping but could be overcome by the use of a proper phase unwrapping method. The second kind of poles are in the signal region. A main reason of causing these poles is under-sampling of the image. For this kind of poles, there is no guarantee that the unwrapped phase map is the true phase map. A good phase unwrapping method can only give a result that has a higher probability to be correct. Phase unwrapping has been and will still be a problem seeking better solutions for different applications.

All the water-fat imaging methods we mentioned previously rely on a successful phase unwrapping of the 2Θ map, which is often difficult and not robust in clinical applications. Phase unwrapping of the 2Θ map is especially difficult if not impossible when the tissues are imaged as disconnected pieces in the FOV. Even if the phase unwrapping is successful, water fat can be separated but cannot be uniquely identified. This may cause the water images and fat images displayed inconsistently when multi-slice images are to be displayed. Inconsistent water and fat separation can also occur between disconnected pieces of tissues in the FOV.

2.7 Thesis Outline

In chapter 3, we will introduce a new method for water-fat imaging. With three image acquisitions, a general direct phase encoding (DPE) of the chemical shift information is achieved, which allows an unambiguous determination of water and fat on a pixel by pixel basis. We have three publications [59,60,61] about this method.

In chapter 4, new improvements in image SNR for the DPE method will be introduced and details of noise performance analysis will be discussed.

In chapter 5, a special DPE sampling scheme will be introduced. With three-orthogonal phase (TOP) image acquisitions, it allows a correction of image magnitude errors caused by factors such as T_2^* relaxation. We have one publication [67] about this method. A US patent application of the techniques described in chapter 3, chapter 4, and chapter 5 has been filed.

In chapter 6, we will introduce a new two-point water-fat imaging method. By sampling water and fat asymmetrically and minimizing the gradient energy in a phase map, this method determines water and fat without ambiguity and handles disconnected tissues well. We have one publication [70] about this method.

In chapter 7, we will introduce a new general method of chemical shift imaging with spectrum modeling (CSISM). This method models a spectrum as several peaks with known resonance frequencies but unknown peak amplitudes which can be resolved from a set of spin-echo images. We have one publication [72] about this method. A US patent application of this technique has been filed.

In chapter 8, the general ideas, results and conclusions of all the methods we introduced in this thesis will be discussed, compared, and summarized.

2.8 Glossary

CSI: Chemical Shift Imaging

CSISM: Chemical Shift Imaging with Spectrum Modeling

DPE: Direct Phase Encoding

FOV: Field Of View

GOF: Global Orientation Filter

LOF: Local Orientation Filter

LSE: Least Square Error

MGE: Minimized Gradient Energy

MRI: Magnetic Resonance Imaging

MST: Minimum Spanning Tree

NMR: Nuclear Magnetic Resonance

NSA^*: effective Number of Signals Averaged

RF: Radio-Frequency

RMST: Regional Minimum Spanning Tree

SNR: Signal to Noise Ratio

SRF: Spin Reversal Filter

TE: Time of Echo

TOP: Three Orthogonal-Phase

TR: Time of Repetition

CHAPTER 3

WATER-FAT IMAGING WITH DIRECT PHASE ENCODING (DPE)

3.1 Data Acquisition and Direct Solutions to the Complex Equations

We developed a new 3-point water-fat imaging method that allows a direct solution of water and fat at the pixel level. The two rotating vectors of water and fat were sampled asymmetrically instead of sampling them only at angles of multiple of π radians. At the beginning of our research, a $(0, \pi/2, \pi)$ sampling scheme was adopted [59]. Several months later, a general DPE sampling scheme $(\alpha_0, \alpha_0+\alpha, \alpha_0+2\alpha)$ and corresponding processing algorithm were developed [60,61]. For DPE, either a spin-echo or a gradient-echo pulse sequence can be used to acquire three complex images with time shift $\Delta t = \tau_0$, $\tau_0+\tau$, and $\tau_0+2\tau$. As shown in Figure 3-1 (a) and (b), the time shift Δt is measured from the refocusing time t_0 to the echo-time TE, where t_0 has different definitions in spin-echo and gradient-echo pulse sequences. In a spin-echo sequence, the refocusing time t_0 is simply the Hahn echo position; in a gradient-echo sequence, the refocusing time t_0 must be one of those time instances when the water and fat vectors are in-phase, i.e. t_0 must satisfy that

$$\Delta\omega\, t_0 = n\, 2\pi \qquad (n = \text{integer}) \qquad (3\text{-}1)$$

In a spin-echo sequence, Δt can be adjusted by either changing the location of the 180° refocusing pulse or the TE, or both. In a gradient-echo sequence, Δt is adjusted by changing the TE.

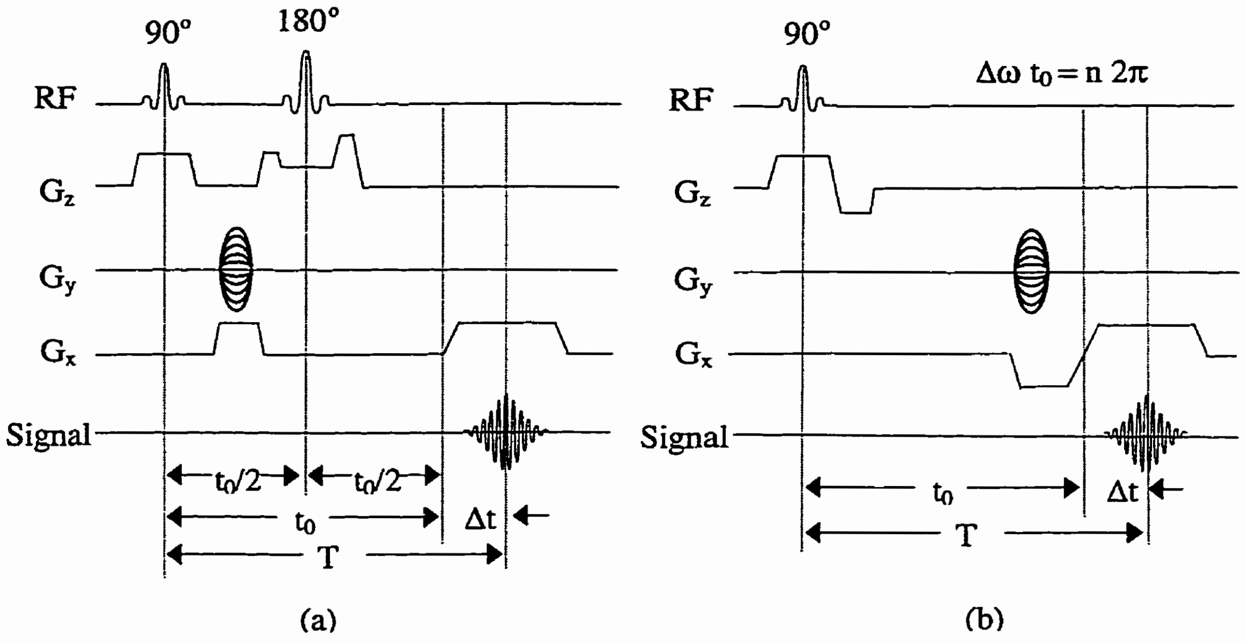

Figure 3-1 (a) Spin-echo and (b) gradient-echo pulse sequences for DPE

Three acquisitions with different amount of time shift Δt are performed for each phase encoding step. After ordinary image reconstruction, three complex images I_1, I_2, and I_3 are obtained and expressed as

$$\begin{aligned} I_1 &= [W + F\exp(i\alpha_0)]\exp(i\Phi)\exp(i\Theta_0) \\ I_2 &= [W + F\exp(i\alpha_0)\exp(i\alpha)]\exp(i\Phi)\exp(i\Theta_0)\exp(i\Theta) \\ I_3 &= [W + F\exp(i\alpha_0)\exp(i2\alpha)]\exp(i\Phi)\exp(i\Theta_0)\exp(i2\Theta) \end{aligned} \tag{3-2}$$

where $\alpha_0 = \Delta\omega\,\tau_0, \alpha = \Delta\omega\,\tau$, $\Theta_0 = -\gamma\Delta B_0\tau_0$, and $\Theta = -\gamma\Delta B_0\tau$; Φ is still the constant phase error caused by systematic errors such as RF inhomogeneity and data acquisition window off-centering. For a gradient-echo sequence, Φ also contains an additional component $\gamma\Delta B_0 t_0$ due to B_0 inhomogeneity. The above equation can be transformed into

$$\begin{aligned} I_1 &= (W + C\,F)\,P_0 \\ I_2 &= (W + C\,A\,F)\,P_0P_1 \\ I_3 &= (W + C\,A^2\,F)\,P_0P_1^{\,2} \end{aligned} \tag{3-3}$$

by defining four complex factors C, A, P_0, and P_1 as follows

$$\begin{aligned} C &= \exp(i\alpha_0) \\ A &= \exp(i\alpha) \\ P_0 &= \exp(i\Phi)\exp(i\Theta_0) \\ P_1 &= \exp(i\Theta) \end{aligned} \tag{3-4}$$

It is helpful to introduce two new complex variables X and Y as

$$\begin{aligned} X &= W P_0 P_1 \\ Y &= F C A P_0 P_1 \end{aligned} \tag{3-5}$$

Obviously, W and F are the magnitudes of X and Y. From equations (3-3), we have

$$\begin{aligned} I_2 &= X + Y \\ I_1 I_3 &= X + Y + X Y(A + 1 / A) \end{aligned} \tag{3-6}$$

This set of complex equations has two possible solutions for X and Y

$$\begin{aligned} X &= \frac{1}{2}(I_2 \pm \Delta I) \\ Y &= \frac{1}{2}(I_2 \mp \Delta I) \end{aligned} \tag{3-7}$$

where ΔI is defined as

$$\Delta I = \sqrt{(A+1)^2 I_2{}^2 - 4AI_1I_3} \Big/ (A-1) \tag{3-8}$$

The ambiguity in the solutions of X and Y is caused by the complex square-root operation. This ambiguity is expected since X and Y hold symmetric positions in equations (3-5). However, this symmetry between X and Y can be broken by using the definitions of X and Y in equations (3-5), provided that

$$CA \neq \pm 1 \tag{3-9}$$

The phasor CA is given by $CA = \exp(\alpha_0 + \alpha)$, where $\alpha_0 + \alpha$ is determined by the parameter $\tau_0 + \tau$. It can be seen from equations (3-5) that vectors Y and $(CA)X$ are in the same direction. Therefore, vector Y is leading X by the angle of $\alpha_0 + \alpha$. When CA is

1 or -1, X and Y are parallel or anti-parallel and cannot be distinguished by the leading and lagging relationship. Therefore, we should avoid making $\alpha_0 + \alpha$ multiples of π in data acquisitions. As a matter of fact, X and Y represent the water and fat magnetization vectors in the second image. Because fat has a lower precession frequency than water does, fat magnetization rotates counter-clockwise relative to water magnetization. Therefore, the fat magnetization vector should be leading the water magnetization vector by an angle of $\alpha_0 + \alpha$ at time shift $\Delta t = \tau_0 + \tau$. According to this leading and lagging phase relationship, the correct X and Y solution can be determined from the two possible solutions. This binary choice of solutions is schematically illustrated below.

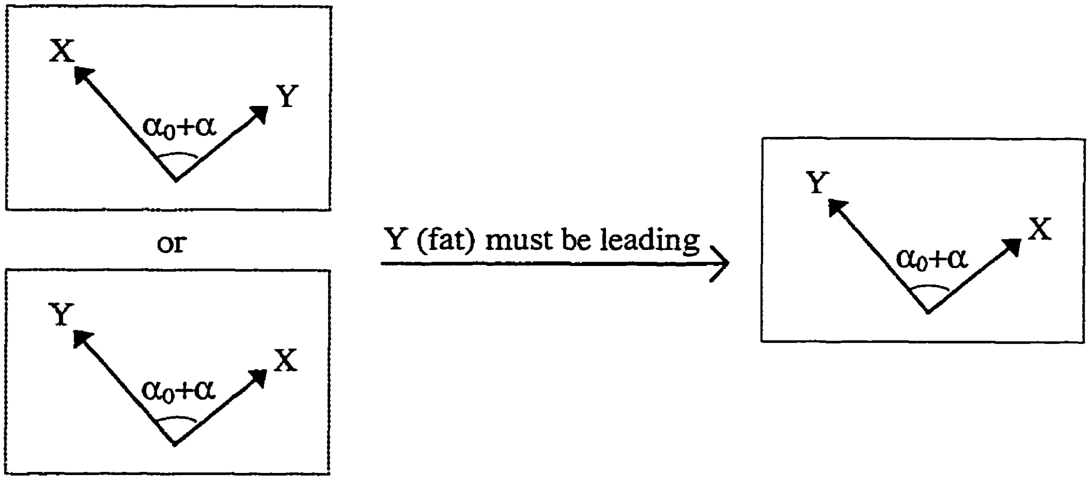

Figure 3-2 Binary choice between the two solutions

This binary choice between the two solutions is implemented in the computer program as follows. First, one set of solutions for X and Y in equations (3-7) is taken temporarily as the right answer. Then, two dot products D_1 and D_2 are calculated by

$$\begin{aligned} D_1 &= X \cdot [Y/(CA)] = \mathrm{real}(X)\,\mathrm{real}[Y/(CA)] + \mathrm{imag}(X)\,\mathrm{imag}[Y/(CA)] \\ D_2 &= Y \cdot [X/(CA)] = \mathrm{real}(Y)\,\mathrm{real}[X/(CA)] + \mathrm{imag}(Y)\,\mathrm{imag}[X/(CA)] \end{aligned} \qquad (3\text{-}10)$$

where "real" and "imag" represent taking the real part and imaginary part of a complex number, respectively. If D_1 is greater than or equal to D_2, it means the choice of solution is correct and X and Y remains unchanged; If D_1 is less than D_2, it means the choice of solution is wrong and X and Y should be swapped. This binary choice procedure is performed for every pixel in the FOV.

3.2 Special Treatment for Pixels with A Single Component

The above solution of water and fat vectors works well if both W and F are significantly larger than noise in a pixel. However, it is possible that one of the two components in a pixel is so small that it is embedded in the noise. This corresponds to the troublesome "single peak" situation even in localized spectroscopy, where we cannot tell which chemical the peak represents since the relative relationship between peaks is not available. In our case, when a pixel has only a single component, the binary choice of water and fat based on their relative phase relationship becomes unreliable, with about 50% chance to be incorrect depending on the local SNR. However, a voxel containing pure fat is not realistic in living tissue [62]. If one of the two variables X and Y is nearly zero, one can simply assign this pixel to be pure water. In our implementation, we simply compared the magnitudes of X and Y. If one is less than a small fraction (e.g. 7 %) of the other, the longer vector will be determined as water and the shorter one as fat. This operation is used to introduce a statistical bias towards water for those single peaked pixels. The specific value of the threshold is not critical if the "global orientation filter (GOF)" described in the next section is used.

3.3 Orientation Filtering

After the steps described in the previous two sections, X and Y have been determined for most of the pixels. Some pixels, many of which are single peaked pixels, could be given swapped (X, Y) solutions due to poor SNR or artifacts. These wrong assignments can be corrected for based on the fact that the complex phasors P_0 and P_1, although unknown, are usually smoothly changing spatial functions.

A local orientation filter (LOF) was first developed. An orientation vector O is defined as

$$O = X + Y / (CA) \tag{3-11}$$

From the equations (3-4), we see that O is parallel to P_0P_1 if X and Y has been correctly determined. A mean value <O> of the orientation vector O is calculated in a sliding window (e.g. 7×7 pixels). Then, two possible values of O for the central pixel, O_1 and O_2, are computed by

$$\begin{aligned} O_1 &= X + Y / (CA) \\ O_2 &= Y + X / (CA) \end{aligned} \tag{3-12}$$

These two orientation vectors are compared with <O> by computing two dot products

$$\begin{aligned} D_1 &= O_1 \cdot < O > \\ D_2 &= O_2 \cdot < O > \end{aligned} \tag{3-13}$$

If D_1 is greater than or equal to D_2, X and Y keeps unchanged; If D_1 is less than D_2, X and Y are swapped. The basic assumption here is that the majority of the pixels everywhere in the FOV have correct (X,Y) assignment before filtering. Hence, <O> represent the correct direction of O for the central pixel in the sliding window. If O_1 agrees better with <O>, as reflected in a greater D_1 value, the original assignment of (X,Y) for the central pixel would be correct; But if O_2 agrees better with <O>, it means that the original (X,Y) assignment for the central pixel is wrong, thus X and Y need to be swapped.

LOF has been successfully used to reconstruct many water-fat images. In a few cases, LOF failed for some regions where the majority of pixels have wrong (X,Y) assignments before filtering. These regions were contaminated by artifacts and some unknown factors. In such a situation, information from more distant pixels can be helpful in getting the correct (X,Y) assignments for pixels in the troubled regions. Global orientation filter (GOF) was developed to achieve this goal.

GOF is a statistical operator based on repeated region growing from randomly distributed seeds. Initially, a pixel is chosen at random as a seed and its normalized orientation vector O_s defined as

$$O_s = \text{phasor}[X_s + Y_s / (CA)] \tag{3-14}$$

is computed, where X_s and Y_s are the X and Y vectors for the seed. Two normalized orientation vectors O_1 and O_2 defined as

$$\begin{aligned} O_1 &= \text{phasor}[X + Y / (CA)] \\ O_2 &= \text{phasor}[Y + X / (CA)] \end{aligned} \tag{3-15}$$

are computed for the surrounding 4-connected neighboring pixels and compared with that of the seed. The comparison is done by computing the dot products D_1 and D_2 defined as

$$\begin{aligned} D_1 &= O_s \cdot O_1 \\ D_2 &= O_s \cdot O_2 \end{aligned} \tag{3-16}$$

If D_1 is greater than a threshold T $(\text{e.g.}\, T = 0.985)$, the pixel is grown with X and Y unchanged; If D_2 is greater than the threshold T, the pixel is grown with X and Y swapped; If both D_1 and D_2 are greater than or smaller than the threshold T, the pixel is not grown. The use of the threshold T is to prevent growing in the background noise, as we can see that the neighboring pixel will not be grown unless O_1 or O_2 is nearly parallel to O_s (within $\pm 10^0$ range for T=0.985). This range is to accommodate the impact of noise and artifacts on the solutions, as well as the finite line-width of fat in the chemical shift spectrum. After the 4-connected neighboring pixels have been visited, the grown pixels are used as new seeds for the growing of the next layer. The grown pixels will not be visited again. This process continues until no more pixels can be grown. To monitor the operation of the global orientation filtering, a consistency score has been accumulated as

$$S_{n+1} = \begin{cases} S_n + 1 & \text{if X and Y are not swapped at the (n + 1)th pixel} \\ S_n - 1 & \text{if X and Y are swapped at the (n + 1)th pixel} \end{cases} \qquad (3\text{-}17)$$

where S_n and S_{n+1} are the consistency scores after the nth and (n+1)th pixel are grown, respectively. S is the differential number of pixels without and with (X,Y) swaps, reflecting the reliability of the original X and Y solutions at the seed, as well as the performance of the growing process. For instance, if the seed is a "bad" pixel with a wrong assignment of X and Y, one can expect a large number of (X,Y) swaps due to the data inconsistencies, and the score S will be negative. In contrary, if the seed is a "good" pixel with a correct (X,Y) assignment, there will be less (X,Y) swaps, and the score S will be positive. If at any step the score S is negative, the growing process is considered invalid and will be terminated and the process will start again with a new seed.

A grown region usually covers one piece of isolated tissue. There can be many pieces of isolated tissue in the whole FOV. Hence, the above growing process is repeated with many different candidates of seeds. They are chosen at random and are evenly distributed in the FOV with sufficient density so that every piece of isolated tissue is covered. A predetermined integer N (e.g. N=7) is used to limit the processing time: for a seed to qualify to grow, the pixel must be visited less than N times by the previous growths.

From the results of all the valid growths, a "vote" is taken at each pixel to decide whether the X and Y values should be swapped or not: They are swapped if more than half votes indicate so.

Theoretically, the GOF requires only more than half of the pixels on each isolated piece of tissue to be correct in the original X and Y assignments. Usually this condition is satisfied in tissues, as pixels containing both water and fat are well determined. These double peaked pixels constitute a significant fraction of the total, and the rest are about 50% to be incorrect. The statistical bias introduced by no-pure-fat assumption is only necessary to handle challenges created by an entire isolated piece of fat free tissue, which seldom happens in a realistic clinical MRI scan.

Because the GOF uses the global statistical properties of the original X and Y images, it is much less sensitive to local image artifacts than the LOF. However, due to the threshold in GOF, some isolated noisy pixels may not be corrected by GOF. In this case, LOF after GOF can be helpful to correcting for these isolated noisy pixels.

3.4 Second Pass Solution and Optimal Averaging

After the X and Y images are treated by the GOF and LOF, they can be directly used to produce water and fat images by simply taking their magnitudes. Alternatively, W and F which are the magnitudes of X and Y, can be substituted back into equations (3-3) to obtain the unknown phasors P_0, P_0P_1, and $P_0P_1^2$, allowing a second pass solution of water and fat components. The latter option is much superior in terms of SNR in the final results. The phasors P_0, P_0P_1, and $P_0P_1^2$ are calculated by

$$P_0 = \frac{I_1}{W+CF}$$
$$P_0P_1 = \frac{I_2}{W+CAF} \tag{3-18}$$
$$P_0P_1^2 = \frac{I_3}{W+CA^2F}$$

Ideally, the above phasors should be fairly smooth functions. In reality, they may have significant fluctuations as they were obtained pixel by pixel from a set of non-linear complex equations where the noise and artifacts can propagate in a complicated manner. A simple smoothing operation on these phasors with a standard $n \times n\,(\text{e.g.}\, 7 \times 7)$ pixel sliding window averaging should effectively reduce the standard deviation of the fluctuation by a factor of n. After the phasors P_0, P_0P_1, and $P_0P_1^2$ are smoothed, they can be removed from the original equations (3-3), resulting in the following phase corrected images

$$J_1 = W + CF$$
$$J_2 = W + CAF \tag{3-19}$$
$$J_3 = W + CA^2F$$

where J_1, J_2, and J_3 are obtained by multiplying I_1, I_2, and I_3 with the complex conjugate of the appropriate phasors, respectively. Three sets of solutions for W and F can be found from the three equation pairs formed from the above equation

$$W_{12} = \frac{J_1A - J_2}{A-1}$$
$$F_{12} = \frac{J_2 - J_1}{C(A-1)} \tag{3-20}$$

$$W_{23} = \frac{J_2A - J_3}{A-1}$$
$$F_{23} = \frac{J_3 - J_2}{CA(A-1)} \tag{3-21}$$

$$W_{13} = \frac{J_1 A^2 - J_3}{A^2 - 1}$$
$$F_{13} = \frac{J_3 - J_1}{C(A^2 - 1)} \tag{3-22}$$

These solutions should be essentially identical and differ only in noise and artifacts, therefore they can be averaged for an improved final result. Since the three solutions in general have different SNR, an optimally weighted averaging would be superior to a simple averaging [63]. Thus we have

$$< W >= \lambda W_{12} + \eta W_{23} + \xi W_{13}$$
$$< F > = \lambda F_{12} + \eta F_{23} + \xi F_{13} \tag{3-23}$$

where λ, η, and ξ are the optimal weighting factors which are shown to be [Appendix A]

$$\lambda = \eta = \frac{1}{2(2 + \cos\alpha)}$$
$$\xi = \frac{1 + \cos\alpha}{2 + \cos\alpha} \tag{3-24}$$

where α is the angular increment in the three acquisitions. The SNR equivalent "number of signal averaged" (NSA*) [32] of the optimal averaging is [Appendix A]

$$(\mathrm{NSA}^*)_{\mathrm{opt}} = \frac{4}{3}(2 + \cos\alpha)(1 - \cos\alpha) \tag{3-25}$$

Similarly, the NSA* for a simple averaging can be obtained as

$$(\mathrm{NSA}^*)_{\mathrm{simple}} = \frac{18\sin^2\alpha}{5 + 4\cos\alpha + 2\sin^2\alpha} \tag{3-26}$$

The two curves of $(\mathrm{NSA}^*)_{\mathrm{opt}}$ and $(\mathrm{NSA}^*)_{\mathrm{simple}}$ are plotted in Figure 3-3. The NSA* of the optimal averaging is higher everywhere than the simple averaging, except at points of 0° and 120°, where they are both 0 and 3 respectively. They are very close for α angles under 120°, but differ significantly for larger α angles. This is due to the fact that as α approaches 180°, solutions W_{13} and F_{13} become more noisy, therefore their weighting factor ξ should diminish for an optimal SNR, as can be seen from equation (3-24).

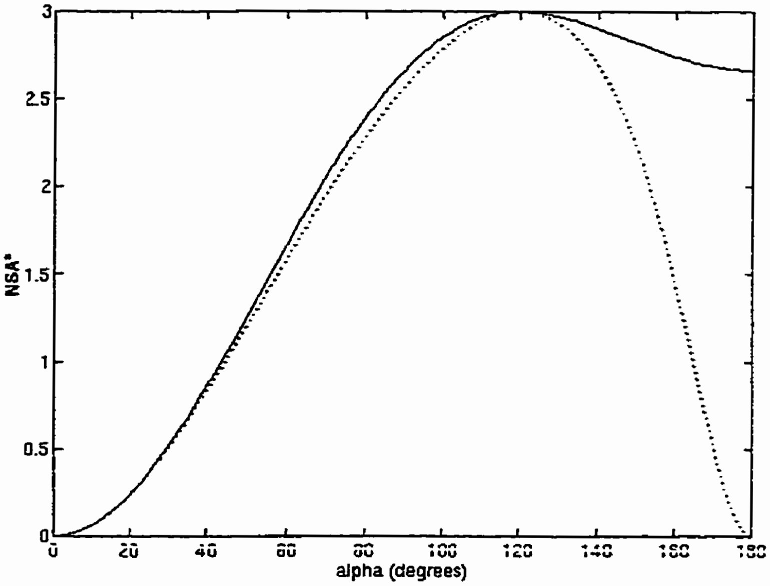

Figure 3-3 The NSA* curves as functions of angle α. Solid line is for optimal averaging, dotted line is for simple averaging.

The final output of water and fat images can be taken as the real parts of the optimal averaging <W> and <F>. By definition, any leakage in the imaginary channels is due to noise and artifacts. This allows another improvement of image quality because the energy of the noise and artifacts in the imaginary channel are discarded and not contributing to the total energy in the result. Similar ideas have been used to identify the spatial distribution of motion artifacts and consequently reducing them [63], or to reduce flow artifacts in MRI by replacing the conventional magnitude reconstruction with a phase-corrected real image reconstruction [64].

3.5 Solution Stability and Phase Error Tolerance

SNR is not the only parameter determining the quality of the water and fat images. If there is a systematic error in the first pass solution of W and F, say a reversed water and fat assignment, the final result will be degraded, which is not characterized by the SNR. This systematic error is related to the stability of the original (X,Y) solutions in equation (3-7), as well as the phase error tolerance in choosing the two sets of (X,Y) solutions and in the orientation filters. A minimized systematic error can be a more important factor than a maximized SNR, in terms of the general quality of the water and fat images.

The solution stability depends on the angular increment α that determines the parameter A in equation (3-8). For example, when α is so small that A is close to 1, the (X,Y) solutions in equation (3-7) become unstable since the denominator in equation (3-8) is nearly zero. On the other hand, $\alpha = 180^\circ$ (corresponding to $A = -1$) would be a good choice for a more stable (X,Y) solutions.

Equation (3-5) shows that the angle between vectors X and Y, or the water and fat magnetization vectors in the second acquired image, is equal to the combined angle $\alpha_0 + \alpha$. Correctly choosing this angle is crucial in determining the leading and lagging vectors, as well as performing the orientation filtering. Clearly, for these operations, the phase error tolerance in X and Y is maximized when this angle is 90° or -90°. A sampling scheme with water and fat being orthogonal in the second image would be optimal, i.e. the central point should be a quadrature sampling.

In situations where the first image is acquired with water and fat in-phase, then $\Theta_0=0$ and it is possible to perform an initial phase correction of the phase error Φ. The phase error Φ can be obtained as the phasor of the in-phase image and removed from all three complex images. This initial phase correction can be especially useful for gradient-echo sequences where the phase error Φ contains a major contribution of B_0 field inhomogeneity. This phase error, when very large and not corrected, may have negative impact on the orientation filters and the smoothing operations.

3.6 Experimental

Considering factors such as solution stability, phase error tolerance, SNR, span of Δt, and initial phase correction, we implemented a $(0°,90°,180°)$ version of DPE on several clinical imagers with field strengths ranging from 0.5T to 1.5T (SIGNA, GE Medical Systems, Milwaukee, WI; and EDGE, Picker International Inc., Highland Heights, OH). The standard spin-echo sequences were modified to perform a 3-point interleaved acquisition by shifting either the 180° RF pulse or the frequency encoding structure. With this sampling scheme, the more familiar "in-phase" and "opposed-phase" images are also easily available, which by themselves may be useful in certain applications [65]. Different parts of the body of volunteers and patients have been imaged in the past years, including head, neck, shoulder, abdomen, pelvis, thigh, knee, calf, ankle, and wrist, using various types of RF coils [66]. The NSA* for the $(0°,90°,180°)$ sampling scheme is 2.67.

Raw data or complex image data were saved and processed on UNIX based workstations (Sun Sparc 10, Sun Microsystems, Mountain View, CA; and DEC 3000/400, Digital Equipment Corporation, Maynard, MA). The algorithm was coded in the C and C++ programming language as a subroutine that inputs the three complex images and outputs the water and fat images with no user intervention. The operations are summarized as the following steps

- If C=1, remove phase error Φ in original images I_1, I_2, and I_3
- Find 2 sets of possible solutions for (X,Y)
- Choose the correct (X,Y) according to the leading or lagging phase relationship
- Single peak treatment
- Apply GOF & LOF to X & Y images to get the 1st pass W & F solutions
- Find 3 phasors and obtain phase corrected images J_1, J_2, and J_3
- Find 3 sets of 2nd pass W & F solutions
- Output W & F images as optimal averaging of the 3 sets of solutions

The data processing software has been made so user friendly that the water and fat images could be reconstructed by the technologists in minutes after each scan. With a current version of the software, the processing time per slice from the three complex images to the water and fat images on a Sparc 10 workstation is only 10-15 seconds, depending on the anatomical structure in the image. Experiments were also performed to test other sampling schemes such as (45°,90°,135°) or (0°,120°,240°) with both spin-echo and gradient-echo sequences on a 0.5T GE SIGNA system, as well as on a 1.5 T Picker EDGE system. In all the experiments, no special effort was spent to shim the magnetic field.

Hundreds of studies on volunteers and patients each of 5-32 slices have been performed in several local hospitals, mostly with T_1 Weighted but a few T_2 weighted scans. The results were excellent. Some typical results are shown in Figures 3-4 to 3-6. DPE is quite tolerant to noise and artifacts, therefore appears to be robust. In Figure 3-7, water-fat images from sampling schemes of (45°,90°,135°), (0°,90°,180°), and (0°,120°,240°) were compared. The SNR is consistent with the theoretical description in equation (3-25). DPE is also experimentally tested to be successful with gradient-echo sequences. Some typical results are given in Figure 3-8.

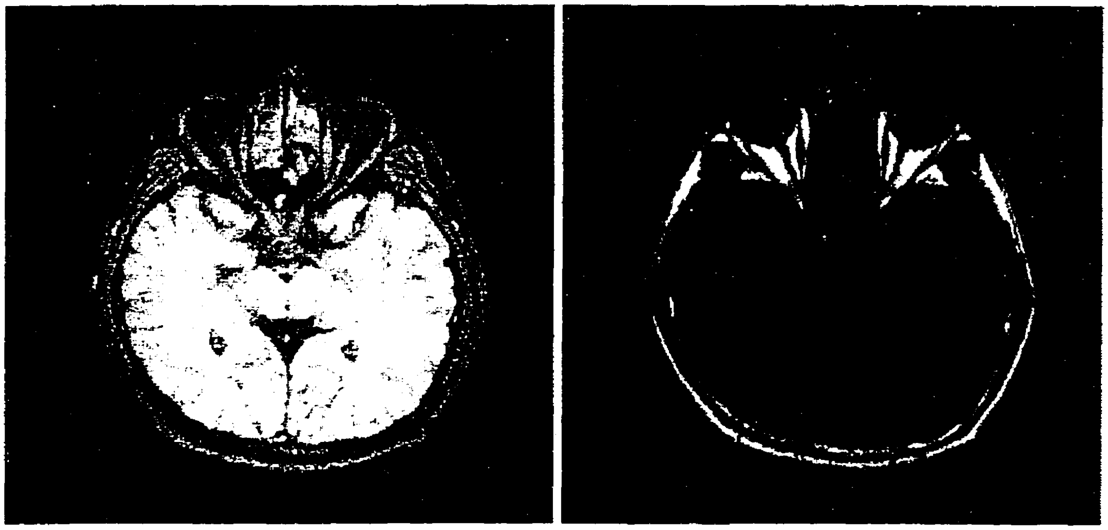

(a) (b)

Figure 3-4 Transverse water (a) and fat (b) images of the head acquired at 0.5 T. Spin-echo, TR=500ms, TE$\approx$ 15ms, sampling scheme (0°,90°,180°).

(a) (b)

Figure 3-5 Transverse water (a) and fat (b) images of the abdomen acquired at 0.5 T. Spin-echo, TR=600ms, TE$\approx$20ms, sampling scheme $(0°, 90°, 180°)$. The result is uniformly good over a large FOV, which is difficult for conventional RF fat saturation to achieve.

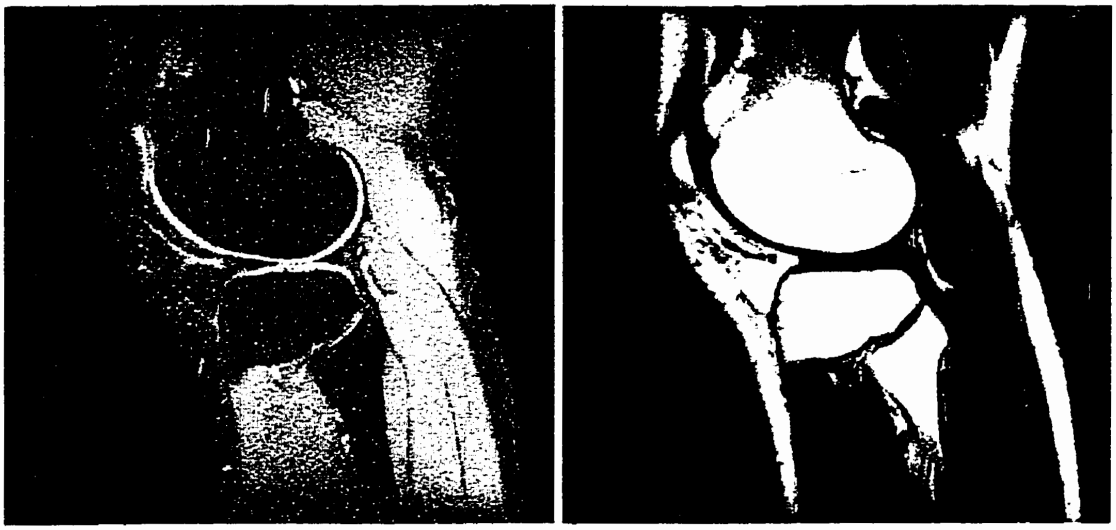

(a) (b)

Figure 3-6 Saggital water (a) and fat (b) images of the knee acquired at 0.5 T. Spin-echo, TR=600ms, TE$\approx$16ms, sampling scheme $(0°, 90°, 180°)$.

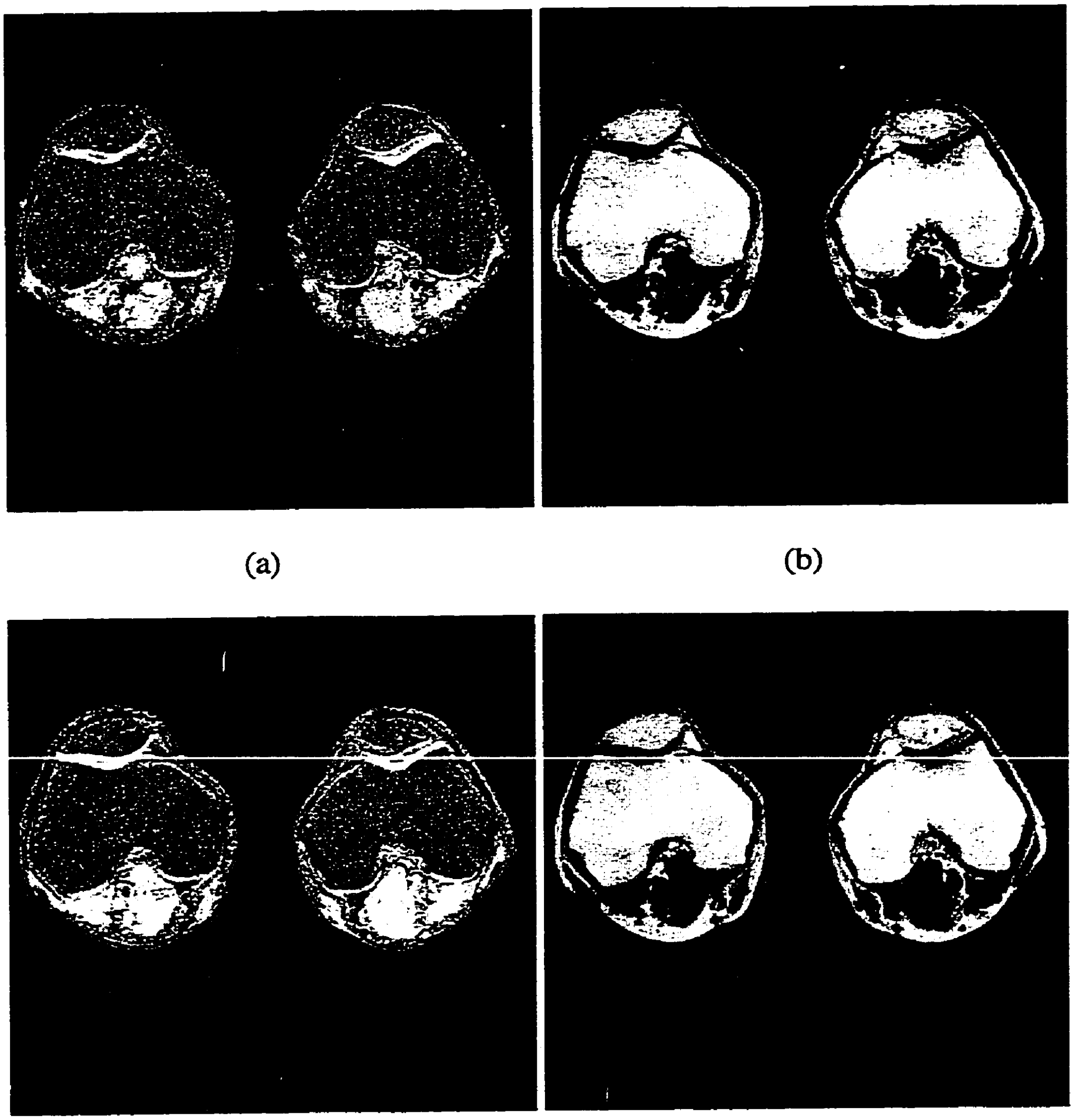

(a) (b)

(c) (d)

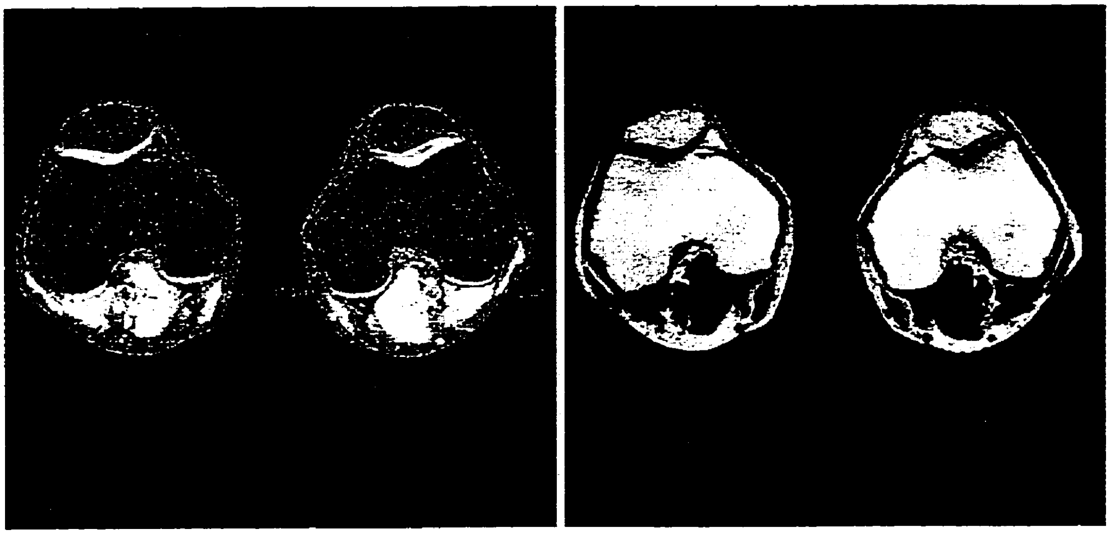

(e) (f)

Figure 3-7 Transverse water (a, c, e) and fat (b, d, f) images of the knee acquired at 0.5 T with different sampling schemes: (45°,90°,135°) for (a, b), (0°,90°,180°) for (c, d), and (0°,120°,240°) for (e, f). Spin-echo, TR=600ms, TE≈20ms.

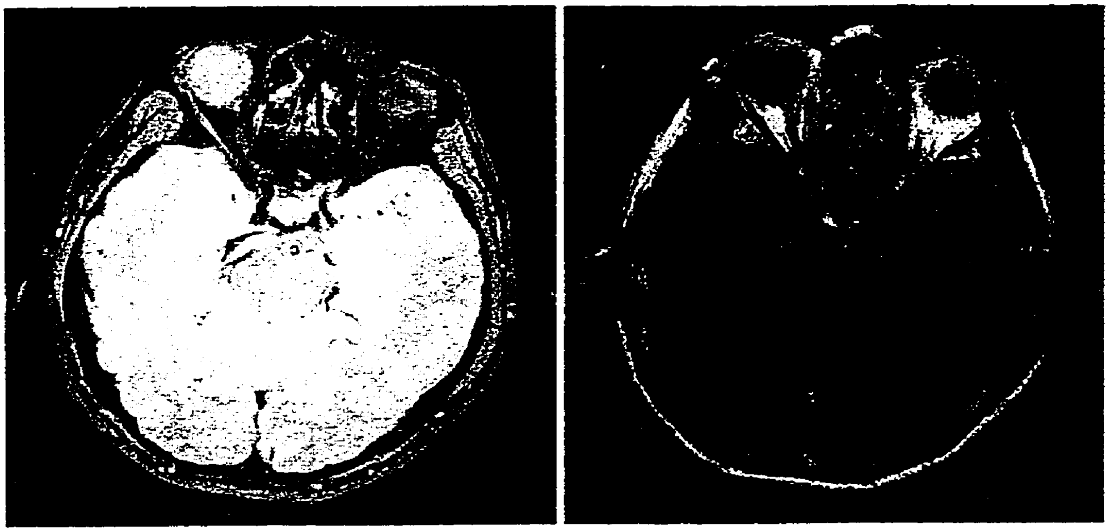

(a) (b)

Figure 3-8 Transverse water (a) and fat (b) images of the head, acquired with a gradient-echo sequence at 1.5 T. TR=500ms, TE=9.00, 10.13, and 11.25 ms, sampling scheme (0°,90°,180°).

3.7 Discussion

If two rotating vectors are sampled only at angles of multiples of π, their relative motion can not be determined without ambiguity. This is analogous to the impossibility of telling how the two hands on a clock exactly rotate if one only sees them being parallel or anti-parallel. DPE samples the rotating magnetization vectors of water and fat at other angles, which is the key to break the symmetry between them, and resolves them for each pixel unambiguously. DPE can not only adequately separate the two components, but also tell which image is water or fat.

A significant advantage of DPE is that it does not rely on the error-prone phase unwrapping, neither assumes global tissue connectivity as required by other methods. DPE determines the water and fat components directly for more than half of the pixels in the image, and we treat the rest by using orientation filters that are only based upon the fact that the phase errors are smoothly changing in tissues. This allows disconnected tissues in the FOV to be resolved without any additional effort.

For pixels containing only a single component, the shorter vector in (X,Y) would be at the noise level without a definite phase relationship relative to the longer vector. As a result, the direct solution of DPE for these pixels will have only about 50% chance to be correct. Although the overall fraction of correctly resolved pixels is still more than half as required by the GOF, the single peak treatment is useful, especially when the original images are of poor quality or there is a pure water phantom in the FOV. The single peak treatment is based on the fact that pure fat does not exist in living tissues. This assumption, however, is not quite true for some pixels that are chemically shifted in the frequency direction near the tissue boundary. The water-fat misregistration makes it possible for these pixels to contain only pure fat. Fortunately, since they have only a very small population and do not change the statistical balance between correctly and incorrectly resolved pixels, therefore their effect is negligible.

The data acquisition and utilization of DPE are very efficient. The three interleaved acquisitions not only provide a reliable water-fat determination, but also improve the SNR significantly. Since multiple averaging is often used for SNR anyway in clinical MRI, the water-fat determination can be considered as almost a bonus at very little or no cost of SNR.

CHAPTER 4

SNR IMPROVEMENT FOR THE DPE METHOD

4.1 Introduction

In the past year, we have gained some new understanding and made improvements to the DPE method. Firstly, we have realized that the final water-fat result obtained from optimal averaging is actually identical to the result obtained from a complex valued least square error (LSE) method. Furthermore, we have found a real valued LSE method that allows a higher SNR for the final water-fat images.

4.2 Complex Valued LSE Method

The equations (3-19) are a set of over-determined linear equations since they have three equations but only two unknowns, i.e. W and F. It is a common practice to solve a set of over-determined linear equations by least square error (LSE) algorithm. Equations (3-19) can be expressed in matrix form as

$$U = MV \tag{4-1}$$

where V is an unknown vector with elements W and F

$$V = \begin{pmatrix} W \\ F \end{pmatrix} \tag{4-2}$$

U is an known vector representing the phase corrected images

$$U = \begin{pmatrix} J_1 \\ J_2 \\ J_3 \end{pmatrix} \tag{4-3}$$

M is a 3×2 matrix given by

$$M = \begin{pmatrix} 1 & C \\ 1 & CA \\ 1 & CA^2 \end{pmatrix} \tag{4-4}$$

The LSE solution [68] of equation (4-1) is given by

$$V = L\,U \tag{4-5}$$

In the above equation, L is a 2×3 matrix given by

$$L = (M^{+}M)^{-1}M^{+} \tag{4-6}$$

where "+" represents the complex conjugate of the transpose of a matrix; "-1" represents the inverse of a matrix. Equation (4-5) can be written more clearly as

$$\begin{pmatrix} W \\ F \end{pmatrix} = L \begin{pmatrix} J_1 \\ J_2 \\ J_3 \end{pmatrix} \tag{4-7}$$

From equation (4-7), W and F can be calculated numerically. The final result of water and fat images can be taken as the real parts of W and F, respectively.

Through analytical derivations, we can prove that the final water-fat result given by the optimal averaging method and the above complex valued LSE method are identical [APPENDIX B]. Due to its simplicity and popularity, the LSE approach appears more attractive. Nevertheless, the equivalence of the optimal averaging method and the complex valued LSE method shows that LSE method is optimal in SNR because the optimal averaging method is designed to maximize SNR.

4.3 Real Valued LSE Method

In the previous section, three complex equations are solved with LSE method to give a complex valued water-fat solution. Then the knowledge of W and F being non-negative real numbers is used to take the real parts of W and F as the final result. In this section, a new approach is adopted to calculate the final water-fat result. First of all, the knowledge of W and F being a non-negative real number is used to split the three complex equations into six real valued equations. Then the LSE solution of (W,F) is calculated from the six real valued equations.

Complex equations (3-19) can be split into the following real valued equations

$$\begin{aligned}
\mathrm{real}(J_1) &= W + F\cos(\alpha_0) \\
\mathrm{imag}(J_1) &= F\sin(\alpha_0) \\
\mathrm{real}(J_2) &= W + F\cos(\alpha_0 + \alpha) \\
\mathrm{imag}(J_2) &= F\sin(\alpha_0 + \alpha) \\
\mathrm{real}(J_3) &= W + F\cos(\alpha_0 + 2\alpha) \\
\mathrm{imag}(J_3) &= F\sin(\alpha_0 + 2\alpha)
\end{aligned} \tag{4-8}$$

The equations (4-8) can be written in matrix form as

$$U = MV \tag{4-9}$$

where V is an unknown vector with unknown elements W and F

$$V = \begin{pmatrix} W \\ F \end{pmatrix} \tag{4-10}$$

U is a known vector given by

$$U = \begin{pmatrix} \mathrm{real}(J_1) \\ \mathrm{imag}(J_1) \\ \mathrm{real}(J_2) \\ \mathrm{imag}(J_2) \\ \mathrm{real}(J_3) \\ \mathrm{imag}(J_3) \end{pmatrix} \tag{4-11}$$

M is a 6×2 matrix given by

$$M = \begin{pmatrix} 1 & \cos(\alpha_0) \\ 0 & \sin(\alpha_0) \\ 1 & \cos(\alpha_0 + \alpha) \\ 0 & \sin(\alpha_0 + \alpha) \\ 1 & \cos(\alpha_0 + 2\alpha) \\ 0 & \sin(\alpha_0 + 2\alpha) \end{pmatrix} \tag{4-12}$$

The LSE solution of equation (4-9) is given by

$$V = L\,U \tag{4-13}$$

In the above equation, L is a 2×6 matrix given by

$$L = (M^T M)^{-1} M^T \tag{4-14}$$

where "T" represents the transpose of a matrix. Equation (4-13) can be written more clearly as

$$\begin{pmatrix} W \\ F \end{pmatrix} = L \begin{pmatrix} \mathrm{real}(J_1) \\ \mathrm{imag}(J_1) \\ \mathrm{real}(J_2) \\ \mathrm{imag}(J_2) \\ \mathrm{real}(J_3) \\ \mathrm{imag}(J_3) \end{pmatrix} \tag{4-15}$$

From the above equation, W and F can be calculated numerically and output as the final water and fat images.

Now, we want to calculate the NSA* of the second pass (W,F) solution. From equation (4-15), The solutions of W and F can be written in more detail as,

$$\begin{aligned} W = {} & L_{1,1}\,\mathrm{real}(J_1) + L_{1,2}\,\mathrm{imag}(J_1) + L_{1,3}\,\mathrm{real}(J_2) + L_{1,4}\,\mathrm{imag}(J_2) \\ & + L_{1,5}\,\mathrm{real}(J_3) + L_{1,6}\,\mathrm{imag}(J_3) \\ F = {} & L_{2,1}\,\mathrm{real}(J_1) + L_{2,2}\,\mathrm{imag}(J_1) + L_{2,3}\,\mathrm{real}(J_2) + L_{2,4}\,\mathrm{imag}(J_2) \\ & + L_{2,5}\,\mathrm{real}(J_3) + L_{2,6}\,\mathrm{imag}(J_3) \end{aligned} \tag{4-16}$$

where $L_{m,n}$ is the matrix element of L at the mth row and nth column. The phase corrected images J_1, J_2, and J_3 have the same noise variances as their original counterparts I_1, I_2, and I_3, i.e. $\sigma_1^2 = \sigma_2^2 = \sigma_3^2 = \sigma_0^2$, since the noise variances in the phasors P_0, P_0P_1, and $P_0P_1^2$ are greatly reduced by heavy smoothing operations. The noise variance of the real part and imaginary part of J_1, J_2, and J_3 is $\sigma_0^2/2$, because the noises in the real part and imaginary part of J_1, J_2, and J_3 are independent of each other and they should add to σ_0^2. Then the noise variance in W, σ_W^2, and the noise level in F, σ_F^2, are given by

$$\begin{aligned} \sigma_W^2 &= (L_{1,1}^2 + L_{1,2}^2 + L_{1,3}^2 + L_{1,4}^2 + L_{1,5}^2 + L_{1,6}^2)(\sigma_0^2/2) \\ \sigma_F^2 &= (L_{2,1}^2 + L_{2,2}^2 + L_{2,3}^2 + L_{2,4}^2 + L_{2,5}^2 + L_{2,6}^2)(\sigma_0^2/2) \end{aligned} \tag{4-17}$$

From numerical calculation, it can be proved that σ_W^2 is always equal to σ_F^2. Therefore, NSA* of the water image and fat image can both be calculated by

$$\begin{aligned} NSA^* &= \frac{1}{\sigma_W^2/(\sigma_0^2/2)} \\ &= \frac{1}{L_{1,1}^2 + L_{1,2}^2 + L_{1,3}^2 + L_{1,4}^2 + L_{1,5}^2 + L_{1,6}^2} \end{aligned} \tag{4-18}$$

The curves of NSA* versus phase increment angle α with different initial phase angle α_0 are plotted in the Figure 4-1.

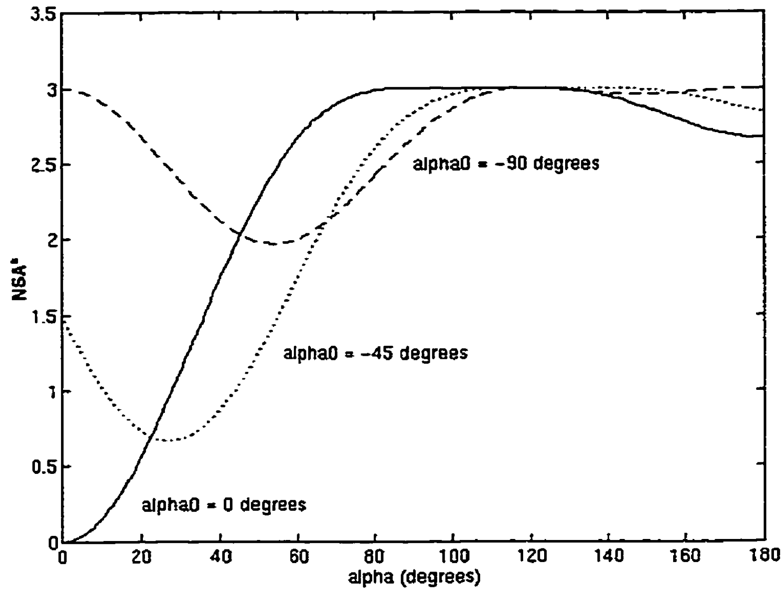

Figure 4-1 NSA* curves as functions of phase increment angle α with different initial phase angle α_0.

For the purpose of comparison, the curve of optimal averaging method (complex valued LSE method) in Figure 3-3 and the curve for real valued LSE method with $\alpha_0 = 0°$ in Figure 4-1 are plotted in Figure 4-2

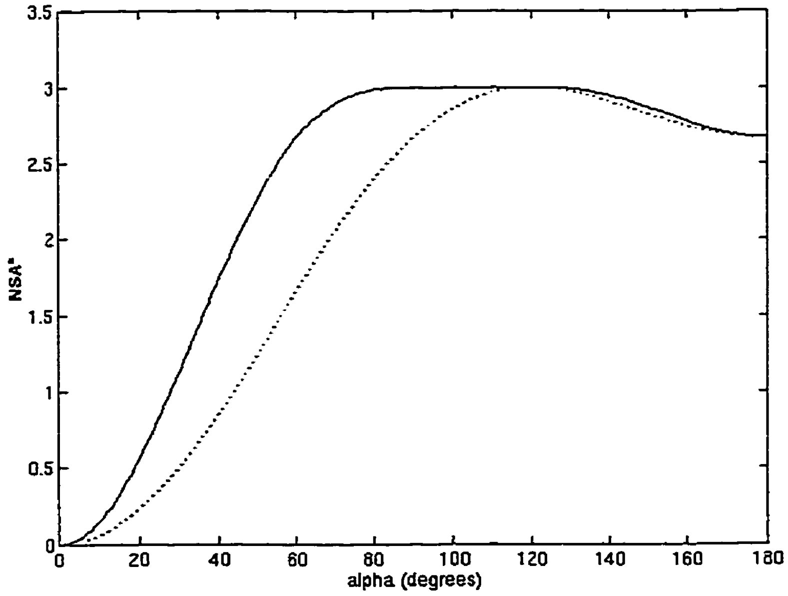

Figure 4-2 NSA* curves for the optimal averaging method (dotted line) and the real valued LSE method with $\alpha_0 = 0°$ (solid line).

Figure 4-2 shows that the real valued LSE method is superior to the optimal averaging method in overall NSA* performance. For the (0°,90°,180°) sampling scheme, the NSA* is 2.67 for the optimal averaging method and 3.0 for the real valued LSE method.

4.4 Experiments and Results

Before this real valued LSE method was adopted, We have already implemented a (0°,90°,180°) version of DPE on several clinical imagers with field strengths ranging from 0.5T to 1.5T (SIGNA, GE Medical Systems, Milwaukee, WI; and EDGE, Picker International Inc., Highland Heights, OH). Now, we replace the optimal averaging algorithm in the water-fat reconstruction programs with the real valued LSE algorithm. The results were excellent. The NSA* for the (0°,90°,180°) sampling scheme was improved from 2.67 with the optimal averaging algorithm to 3.0 with this real valued LSE algorithm. A representative result of a phantom experiment is shown in Figure 4-3. The noise variance in image (a) is about 12% higher than in image (b), which agrees with the NSA* ratio between the optimal averaging algorithm and the real valued LSE algorithm.

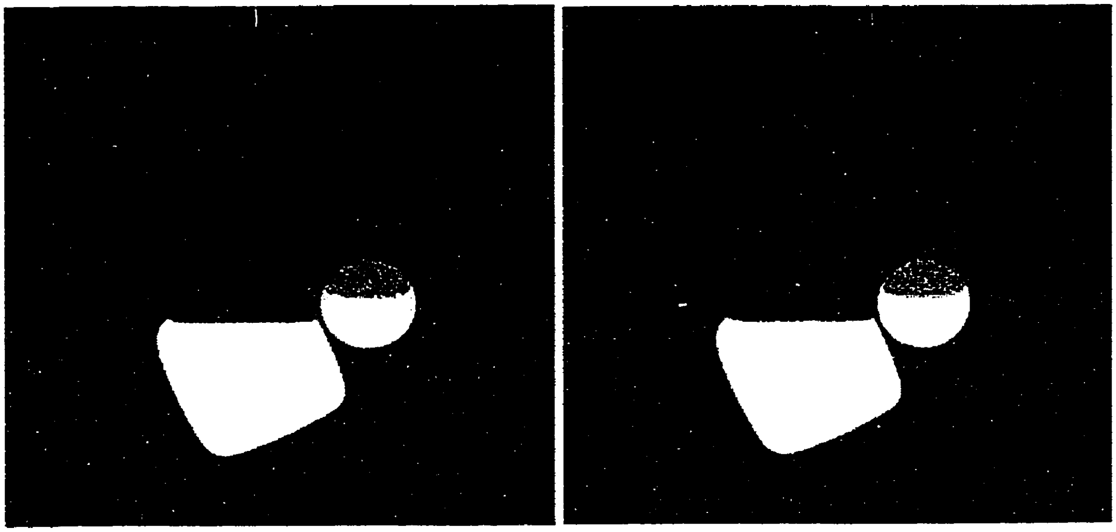
(a) (b)

Figure 4-3 Water images of a water and oil phantom with optimal averaging algorithm (a), and with real valued LSE algorithm (b). Sampling scheme (0°,90°,180°).

4.5 Discussion

The definitions of NSA* in the optimal averaging method and in the real valued LSE method are identical even though they look different. In the optimal averaging method, the NSA* is defined as [APPENDIX A]

$$\mathrm{NSA}^* = \frac{1}{\sigma_W^{\,2} / \sigma_0^{\,2}} \tag{4-19}$$

Assume the NSA* of a pair of water and fat images is 3.0 in the optimal averaging method. The NSA* would become 1.5 if we use the NSA* definition defined in equation (4-18). However, the water and fat images in optimal averaging are complex images. We can take the real part of these images as the final water and fat images to reduce the noise variances by 50 %. Hence, the final NSA* for the real valued water and fat images are still 3.0.

Even though the real valued LSE method is superior to the optimal averaging method in overall SNR performance, the real valued LSE method may be more sensitive to phase errors since the six real valued equations of equations (4-8) are more sensitive to phase errors than the three complex equations of equations (3-17).

CHAPTER 5

WATER-FAT IMAGING WITH THREE ORTHOGONAL-PHASE (TOP) ACQUISITIONS

5.1 Introduction

We know that, for the general DPE method, a sampling scheme with $A=-1$ is the best choice for the (X,Y) solution stability, while a sampling scheme with $CA=\pm i$ is the best choice for phase error tolerance. The sampling scheme $(0°, 90°, 180°)$, which we use most frequently, satisfies the condition of $CA=\pm i$ but does not satisfy the condition of $A=-1$, thus the solution stability is not maximized. A sampling scheme of $(-90°, 90°, 270°)$ or $(90°, -90°, -270°)$ would satisfy both conditions, thus has both stable (X,Y) solutions and strong phase error tolerance [67]. Furthermore, the three orthogonal-phase (TOP) images should have equal magnitudes. Any magnitude difference among these three images should be caused by factors other than water-fat chemical shift effects. This allows a magnitude correction and leads to improved water-fat image qualities. In this chapter, we will investigate TOP thoroughly by taking the $(-90°, 90°, 270°)$ case as an example. The other $(90°, -90°, -270°)$ case will be very much identical, thus will not be discussed.

5.2 Data Acquisition and First Pass Solution

The $(-90°, 90°, 270°)$ water-fat phase encoding corresponds to $\alpha_0=-90°$ and $\alpha=180°$ in the general DPE sampling scheme $(\alpha_0, \alpha_0+\alpha, \alpha_0+2\alpha)$. The three acquired complex images can be expressed as

$$\begin{aligned} I_1 &= (W - iF)P_0 \\ I_2 &= (W + iF)P_0P_1 \\ I_3 &= (W - iF)P_0P_1^2 \end{aligned} \tag{5-1}$$

where W, F, P_0 and P_1 are defined the same way as in chapter 3. Since the magnetization vectors of water and fat are orthogonal in all three images, the magnitudes of I_1, I_2, and I_3 should be equal and can be normalized to a same value, such as the average value of the three images. This can reduce the effects of erroneous magnitude modulations, of which one major cause is intra-voxel dephasing including the effect of T_2*. Hereafter, I_1, I_2, and I_3 in equation (5-1) represent normalized images. Equation (5-1) can be solved similarly as in the DPE method. By defining X and Y as

$$\begin{aligned} X &= W\ P_0P_1 \\ Y &= i\,F\,P_0P_1 \end{aligned} \tag{5-2}$$

The following equations are obtained from equations (5-1)

$$\begin{aligned} I_2 &= X + Y \\ I_1I_3 &= (X - Y)^2 \end{aligned} \tag{5-3}$$

Two possible sets of (X,Y) solutions are given by

$$\begin{aligned} X &= \frac{1}{2}(I_2 \pm \sqrt{I_1I_3}) \\ Y &= \frac{1}{2}(I_2 \mp \sqrt{I_1I_3}) \end{aligned} \tag{5-4}$$

The ambiguity in the solutions of X and Y is caused by the complex square-root operation. This ambiguity is expected since X and Y hold symmetric positions in equations (5-3). However, this symmetry between X and Y can be broken by using the definitions of X and Y in equations (5-2), from which we see that Y should be leading X by 90°. Therefore, X and Y can be distinguished by checking their phase relationship. This works well when both components are significantly greater than noise in a pixel. For some pixels with one of the two components being comparable with the noise level, the single peak treatment is used the same way as in the method described in chapter 3.

5.3 Spin Reversal Filtering (SRF)

After the steps described in the previous section, X and Y has been determined for most of the pixels. Some pixels could still be given swapped (X, Y) solutions due to poor SNR or artifacts. These wrong assignments can be corrected for by the use of an orientation filter. Although a general GOF has been tested to be quite effective for a general DPE sampling scheme $(\alpha_0, \alpha_0 + \alpha, \alpha_0 + 2\alpha)$, two practical problems still remain. The first problem is that there could be several invalid growing processes for a region before a successful growth is found because an original seed with wrong (X,Y) assignment will result in an invalid growing process. These invalid growing processes consume some precious processing time. The second problem is the choice of the threshold angle in determining if a pixel should be grown. From our experience, $\pm 10^0$ is a good value. This angle is so small that it could be difficult to choose a proper universal threshold for different imaging applications, and on different scanners. If the second image I_2 is a quadrature image, i.e. $CA = \pm i$, a spin reversal filtering (SRF) can be used to solve the first problem. The second problem can also be solved if a regional minimum spanning tree algorithm (RMST) is used in the SRF. The sampling scheme $(-90°, 90°, 270°)$ satisfies the condition of $CA = \pm i$, thus SRF can be used to do the orientation filtering. In SRF, a normalized orientation vector O is defined as

$$O = \text{phasor}(X^2 - Y^2) \qquad (5\text{-}5)$$

From the definitions of X and Y, O is found to be

$$O = \text{phasor}[(W^2 + F^2)P_0^2P_1^2] = P_0^2P_1^2 \qquad (5\text{-}6)$$

As we know, P_0 and P_1 are usually smooth phasor maps, thus O will be a spatially smooth phasor map if the (X,Y) assignments are correct for all the pixels. However, O has some sudden reversals due to wrong (X,Y) assignments since the orientation vector O will be equal to $-P_0^2P_1^2$ when a pixel has a wrong (X,Y) assignment. SRF is used to correct for the wrong (X,Y) assignments through removing the sudden reversals of O. There are two alternative approaches to do SRF, which will lead to the same result.

The first approach is to operate SRF directly on the orientation vector O. Initially, an arbitrary pixel in the FOV is chosen as an original seed and its orientation vector O_s is computed. The orientation vectors of the surrounding 4-connected neighboring pixels are computed and compared with that of the seed. The comparison is done by computing a dot product defined as

$$D = O_s \cdot O_n = \text{real}(O_s)\,\text{real}(O_n) + \text{imag}(O_s)\,\text{imag}(O_n) \qquad (5\text{-}7)$$

where O_n is the orientation vector of a neighboring pixel. If $|D|$ is greater than a threshold L (e.g. L= 0.96), i.e. O_s and O_n are near parallel or anti-parallel, D is added to an initially empty data structure T. After four dot products associated with the four neighboring pixels are processed , a dot product with maximum absolute value, D_{max}, is searched out from the data structure T and the associated neighboring pixel is identified. If D_{max} is positive, the pixel is grown with X and Y unchanged; If D_{max} is negative, the pixel is grown with X and Y swapped and O is reversed to -O. Once grown, the seed is labeled to be "visited" to prevent from being visited again in the future rounds of growth, and D_{max} is removed from the data structure T. The newly grown pixel, in turn, becomes a seed for the next round of growth. In each round of growth, from zero to four dot products between the seed and its neighboring pixels that have not been "visited" can be added to the data structure T; The dot product with maximum absolute value is searched out from T and the associated pixel is grown; The newly grown pixel becomes the seed for the next round of growth. This growing process continues until T becomes empty. After the growing process is finished, all the grown pixels constitute a region. In this region, The orientation vectors for all the pixels are consistent with that of the original seed since the inconsistent orientation vectors have been reversed. Nevertheless, the orientation vector of the original seed is not guaranteed to be correct, as a result, the orientation vectors for all the pixels in the region could be all wrong. Hence, there is a binary choice to make for the region: keeping the orientation vectors unchanged or reversing them. A consistency score has been accumulated as

$$S_{n+1} = \begin{cases} S_n + R_n & \text{if O is not reversed at the (n + 1)th pixel} \\ S_n - R_n & \text{if O is reversed at the (n + 1)th pixel} \end{cases} \tag{5-8}$$

where S_n and S_{n+1} are the consistency scores after the nth and (n+1)th pixel are grown, respectively. R_n is the reliability of the original (X,Y) assignment for the nth pixel. In our implementation, R_n is chosen to be the smaller value between $|X|$ and $|Y|$ since the smaller component is easier to be affected by noise and artifact, and hence, more crucial in determining the reliability of the (X,Y) assignment. If the consistency score S for the region is greater than or equal to zero, the orientation vectors are kept unchanged; If S is less than zero, the orientation vectors are reversed and (X, Y) assignments are swapped for all the pixels in the regions. This binary choice is based on the fact that most of the pixels have correct (X,Y) assignments before this orientation filtering. When S is less than zero, it means the original seed for the region has a wrong (X,Y) assignment which leads to all the correct (X,Y) assignments in the region being swapped and all the wrong

(X,Y) assignments being unchanged. This is why we swap all the (X,Y) assignments in the region if score S is less than zero. Unlike GOF, the result of the growth can still be used when the consistency score S is less than zero, therefore there is no invalid growth here, resulting in reduced processing time.

A region usually covers one piece of isolated tissue. There can be many pieces of isolated tissues in the whole FOV. Hence, the above growing process is repeated many times with virtually every pixel in the FOV being a candidate for original seeds. To be qualified as an original seed, the candidate must not have been visited by previous growths, so that each region can only be grown once.

In the whole process of the above spin reversal filtering, two things are worth further discussion. One issue is the specific data structure of T. The search speed of the data structure T largely determines the speed of the whole filtering process. In our implementation, T is a Red-Black Tree [69] that is a balanced binary search tree. Red-Black Tree is fast in search speed and relatively easy to program. The time complexity of searching the maximum or minimum value in the Red-Black Tree is $O(\log_2 n)$, where n is the number of nodes on the tree. Another issue is that the growing paths constitute a minimum spanning tree (MST) for the region. In order to understand MST, some concepts in graph theory need to be introduced. A graph G = (V,E) comprises a set of vertices $V = [v_1, v_2, ...]$ and another set of edges $E = [e_1, e_2, ...]$. A tree is a connected graph without any circuits. In our case, each pixel in an image is considered as a vertex and the link between two connected pixels is considered as an edge. Figure 4-3 shows an example of a tree. In a weighted graph, a weight is associated with each edge. A spanning tree in a graph is a tree connecting all the vertices of G. The weight of a spanning tree is defined as the sum of the weights of all branches in the tree. If the weight of a spanning tree is minimum among all the spanning trees in the graph, this spanning tree is called a minimum spanning tree. It has been found out that the growing path in our SRF process is actually a minimum spanning tree (MST) for the region if we define the weight for each edge w as

$$w = \frac{1}{1+|D|} \qquad (5\text{-}9)$$

The growing method we used belongs to the category of Prim's algorithm for generating a MST [69]. The difference between our MST and a general MST is that we use a threshold to generate a regional minimum spanning tree (RMST) instead of a MST for the whole FOV. It has been proved by experiments that the result of the SRF with RMST is highly consistent no matter which pixel is chosen as the original seed of the region.

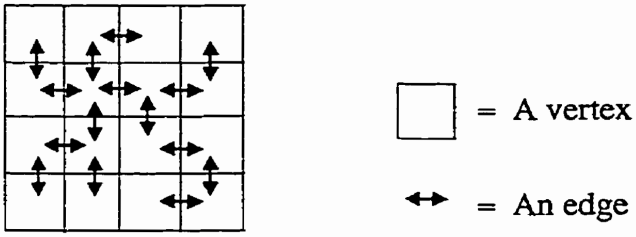

Figure 5-1 An example of a tree in an image

The second approach for doing SRF is based on a regional minimum spanning tree phase unwrapping method. A wrapped phase map P_w for O^2 is calculated by

$$P_w = \arg(O^2) \qquad (5\text{-}10)$$

The wrapped phase map P_w is unwrapped by the following procedure that is analogous to the growing procedure we described above. Initially, an arbitrary pixel in the FOV is chosen as an original seed and its unwrapped phase, P_s, is simply set to be its wrapped phase $P_{w,s}$. Four phase differences between the seed and its 4-connected neighboring pixels are computed, with each of the phase difference ΔP being defined as

$$\Delta P = W(P_{w,n} - P_{w,s}) = \begin{cases} P_{w,n} - P_{w,s} + 2\pi & \text{if } P_{w,n} - P_{w,s} < -\pi \\ P_{w,n} - P_{w,s} - 2\pi & \text{if } P_{w,n} - P_{w,s} > \pi \\ P_{w,n} - P_{w,s} & \text{otherwise} \end{cases} \tag{5-11}$$

where the operator "W" returns the principle value of a phase angle. $P_{w,n}$ is the wrapped phase of a neighboring pixel. If $|\Delta P|$ is less than a threshold M (e.g. M=0.6), ΔP is added to an initially empty red-black tree T. Next, a phase difference of minimum absolute value, ΔP_{min}, is searched out from T and the associated neighboring pixel is identified. The phase for the neighboring pixel, P_n, is unwrapped by

$$P_n = P_s + \Delta P_{min} \tag{5-12}$$

The neighboring pixel is labeled to be "visited" to prevent from being visited again in the future rounds of growth, and ΔP_{min} is also removed from T. The newly grown pixel, in turn, becomes a seed for the next round of growth. This growing process continues until T becomes empty. After the growing process is finished, all the grown pixels constitute a region. In this region, P, the unwrapped phase of O^2, is obtained. The unified orientation vector field O for the region has two possible values

$$O = \pm \exp(i P / 2) \tag{5-13}$$

Note that to use "+" or "-" sign should be consistent for all the pixels in the region. In order to make the binary choice, this unified orientation vector field O is compared with the original O field pixel by pixel to see if O has been reversed. A consistency score S, defined in the same way as that in equation (5-8), is used to determine the correct O field in a similar manner as the first approach. This growing process is repeated many times to cover the whole FOV. This approach of doing SRF will give exactly the same result as the first approach does provided that we make the two threshold values L and M equivalent, which requires

$$L = \cos(M / 2) \tag{5-14}$$

Since some phase unwrapping techniques have been used in the second approach of SRF, it is worthwhile to compare SRF with a general phase unwrapping method [43]. SRF differs from a general phase unwrapping method in at least three aspects. Firstly, SRF is based on regional phase unwrapping which, in many cases is much easier than a general phase unwrapping in the whole FOV. For instance, it is very hard if not impossible for a general phase unwrapping to handle a case where there are separated tissues in the FOV. Secondly, SRF is not a pure phase unwrapping method because it uses other information to do a binary choice of the orientation vector field in each region. Thirdly, the requirement for SRF is less than that of a general phase unwrapping method. SRF, after all, is only required to make a binary choice for each pixel.

Due to the use of RMST, the threshold value in the region growing for SRF is easier to select than for a general GOF. Therefore SRF with RMST is more robust than a general GOF. In addition, SRF is more efficient than a general GOF since there is no invalid growths in SRF.

In some applications, asymmetric k-space data are acquired and the associated complex images will have a linear phase ramp if no phase correction has been done. Hence there may be a linear phase ramp in the constant phasor map P_0. When this phase ramp is very steep, it may challenge the spin reversal filtering process that assumes a smoothly changing phase error. However, it is not difficult to remove the linear phase ramp from the original images I_1, I_2, and I_3 by either re-centering the data in k-space or automatically detecting and correcting the phase ramp in the image domain as follows. Averaged phase gradients of I_1, $<G_x>$ and $<G_y>$, are calculated by

$$\begin{aligned} <G_x> &= \frac{1}{N}\sum \text{phasor}[I_1(x+1,y)I_1(x,y)^*] \\ <G_y> &= \frac{1}{N}\sum \text{phasor}[I_1(x,y+1)I_1(x,y)^*] \end{aligned} \tag{5-15}$$

where N is the total number of non-noise pixels in the image and "Σ" represents the sum over all the non-noise pixels in the image. A phase coherence check is used to see if a pixel is noise or not. If the direction of vector $I_1(x,y)$ is roughly in agreement with that of all its eight neighboring pixels, pixel (x,y) will be considered to be non-noise. Otherwise, the pixel will be considered to be noise. The two averages $<G_x>$ and $<G_y>$ very much represent the linear phase ramps measured in radians per pixel in **x** and **y** directions. The linear phase ramps can be removed from the original images I_1, I_2, and I_3 by multiplying a phasor map P_c, which is given by

$$P_c = \exp(-i <G_x> x - i <G_y> y) \tag{5-16}$$

5.4 Second Pass Solution

After SRF, W and F can be obtained by simply taking the magnitudes of X and Y. For the improvement of SNR, W and F can be substituted into equations (1) to obtain the unknown phasors P_0, P_0P_1, and $P_0P_1^2$

$$
\begin{aligned}
P_0 &= \frac{I_1}{W - iF} \\
P_0 P_1 &= \frac{I_2}{W + iF} \\
P_0 P_1^2 &= \frac{I_3}{W - iF}
\end{aligned}
\tag{5-17}
$$

Because the above phasors are usually smooth spatial functions. They can be smoothed with a small sliding window (e.g. 9×9 pixels) to reduce noise. The three smoothed phasor maps P_0, P_0P_1, and $P_0P_1^2$ are removed from equations (5-1), resulting in the following phase corrected images

$$
\begin{aligned}
J_1 &= W - iF \\
J_2 &= W + iF \\
J_3 &= W - i\ F
\end{aligned}
\tag{5-18}
$$

where J_1, J_2, and J_3 are obtained by multiplying I_1, I_2, and I_3 with the complex conjugate of the appropriate phasors, respectively. Note that we use the original images of I_1, I_2, I_3 instead of the magnitude normalized images when calculating J_1, J_2, and J_3. There are two reasons behind this. One reason is that we want to keep the noise in J_1, J_2, and J_3 being independent to each other so that the signal-noise analysis will be simpler. The other reason is that the normalized I_1, I_2, I_3 in the previous calculations can be anything, such as constant 1, as long as the magnitudes of the three images are equal. In this case, the original images I_1, I_2, and I_3 have to be used to recover the lost magnitude information. From equations (5-18), three sets of solutions for W and F can be found as

$$
\begin{aligned}
W_1 &= \mathrm{real}(J_1) \\
F_1 &= -\mathrm{imag}(J_1)
\end{aligned}
\tag{5-19}
$$

$$
\begin{aligned}
W_2 &= \mathrm{real}(J_2) \\
F_2 &= \mathrm{imag}(J_2)
\end{aligned}
\tag{5-20}
$$

$$\begin{aligned} W_3 &= \mathrm{real}(J_3) \\ F_3 &= -\mathrm{imag}(J_3) \end{aligned} \tag{5-21}$$

These three sets of solutions should be essentially identical and differ only in noise and artifacts, therefore they can be averaged for an improved final result. Thus we have

$$\begin{aligned} <W> &= (W_1 + W_2 + W_3)/3 \\ <F> &= (F_1 + F_2 + F_3)/3 \end{aligned} \tag{5-22}$$

The NSA* for <W> and <F> are 3.0. This final result in equation (5-22) is actually the real valued LSE solution to equation (5-18).

5.5 Experimental

TOP has been tested on a 0.5T GE SIGNA scanner. The standard spin-echo sequences were modified to perform a 3-point interleaved acquisition by shifting the $180°$ RF pulses. Complex image data were saved and processed on UNIX based workstations. The algorithm was coded in the C and C++ programming language. It takes 15-20 seconds to generate a pair of water and fat images. The operations are summarized as the following steps

- Remove linear phase ramps in the original images if necessary
- Normalize the magnitudes of the three original complex images.
- Find 2 sets of possible solutions for (X,Y)
- Choose the correct (X,Y) based on the fact that Y is leading X by $90°$
- Single peak treatment
- Apply SRF with RMST to get the 1st pass W & F solutions
- Obtain phase corrected images J_1, J_2, and J_3
- Find 3 sets of W & F solutions from the real part and imaginary part of J_1, J_2, and J_3

- Output W & F images as simple averaging of the 3 sets of solutions

5.6 Results

Studies on volunteers each of 8 slices have been performed with T_1 Weighted scans. The results are excellent with no failure so far. Some representative water-fat images are shown below.

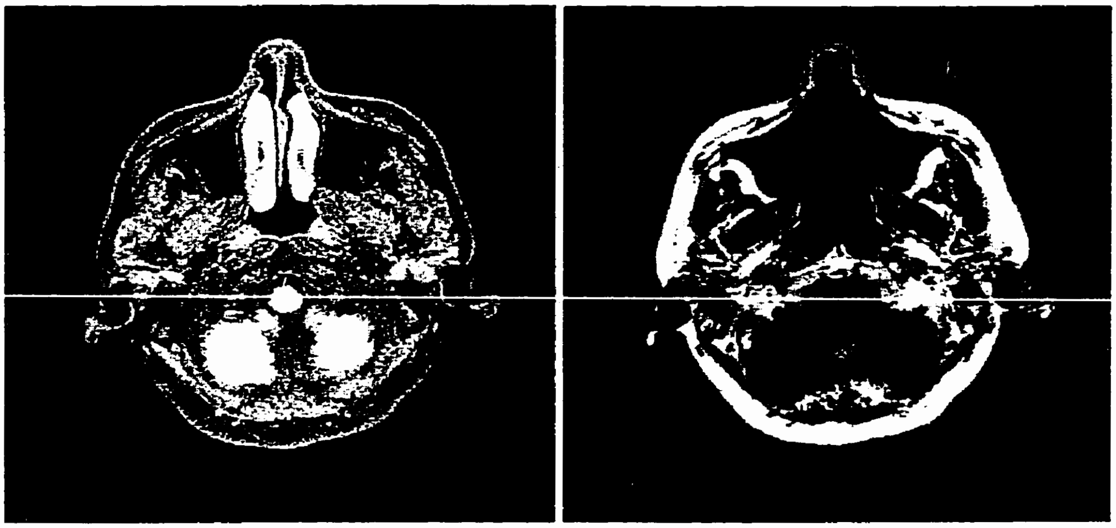

(a) (b)

Figure 5-2 Transverse water (a) and fat (b) images of the head acquired at 0.5 T. Spin-echo, TR=500ms, TE≈20ms, sampling scheme (−90°,90°,270°).

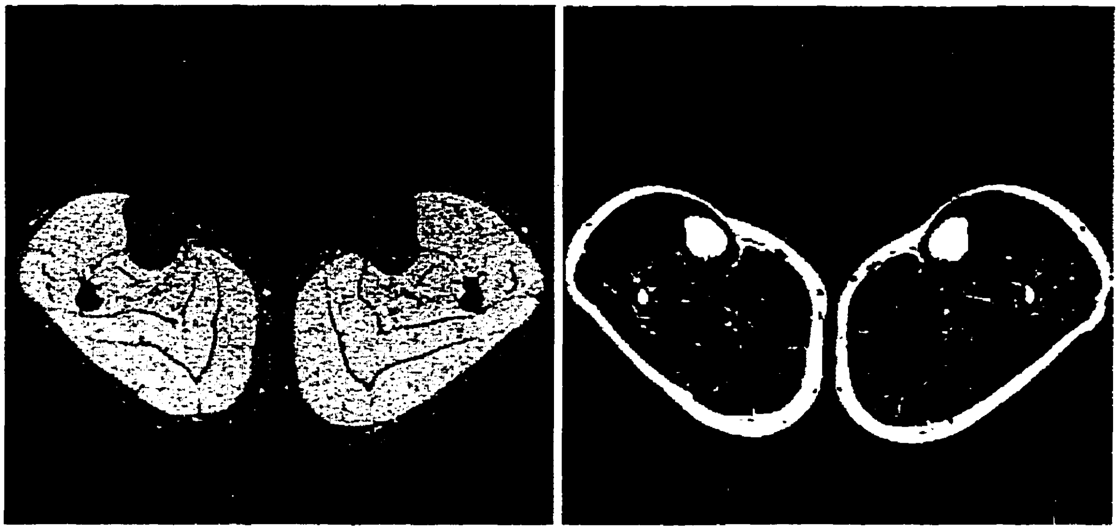

(a) (b)

Figure 5-3 Transverse water (a) and fat (b) images of the leg acquired at 0.5 T. Spin-echo, TR=500ms, TE$\approx$20ms, sampling scheme $(-90°,90°,270°)$.

5.7 Conclusions

As a special case of DPE, TOP is the best sampling scheme for the solution stability since it satisfies $A = -1$. TOP has the best phase error tolerance and allows the use of SRF in orientation filtering due to the fact that TOP satisfies $CA = \pm i$. SRF appears to be an efficient and robust filter, and is applicable to any sampling schemes with the second acquisition being quadrature. It has been used for the TOP and $(0°,90°,180°)$ sampling schemes. TOP also allows a magnitude error correction, which leads to a better magnitude error tolerance. TOP is optimal in SNR with the NSA* being 3.0. Overall, TOP appears to be an optimal sampling scheme of DPE.

CHAPTER 6

TWO-POINT WATER-FAT IMAGING WITH MINIMIZED GRADIENT ENERGY (MGE)

6.1 Introduction

We have shown that DPE and its special case TOP are very robust and efficient water-fat imaging methods. They are the methods of choice if robustness and good SNR is desired. However, when the imaging time is a major concern for some applications, the three-point methods may not be preferred. Instead, two-point methods can be more favored. The existing two point water-fat imaging methods acquire the water-fat in-phase and opposed-phase images by two excitations or single-excitation double-echo sampling schemes [37-43]. From the in-phase and opposed-phase images, the phase error 2Θ map can be obtained. Separate water and fat images can be calculated after the Θ map is obtained by phase unwrapping the 2Θ map. One major problem with existing two-point methods is the unreliability of phase unwrapping. A successful phase unwrapping in the whole FOV is especially difficult if not impossible when tissues are separated by noise, such as the cross-sections of the two separated legs. Even when phase unwrapping is successful, the existing two-point methods can only separate water and fat but cannot tell which is water and which is fat. This is a problem for automatic water-fat image reconstruction and display. We have proposed a two-point method [70] utilizing the gradient energies in the phasor map of a $W + iF$ image to solve the order/connectivity problem [42]. In that method, the gradient energy processing was complicated. In this chapter, we will introduce a more general two-point method with a more clearly defined gradient energy criterion. This two-point method determines water and fat with no ambiguity and handles well-disconnected tissues.

6.2 Data Acquisition and First Pass Solution

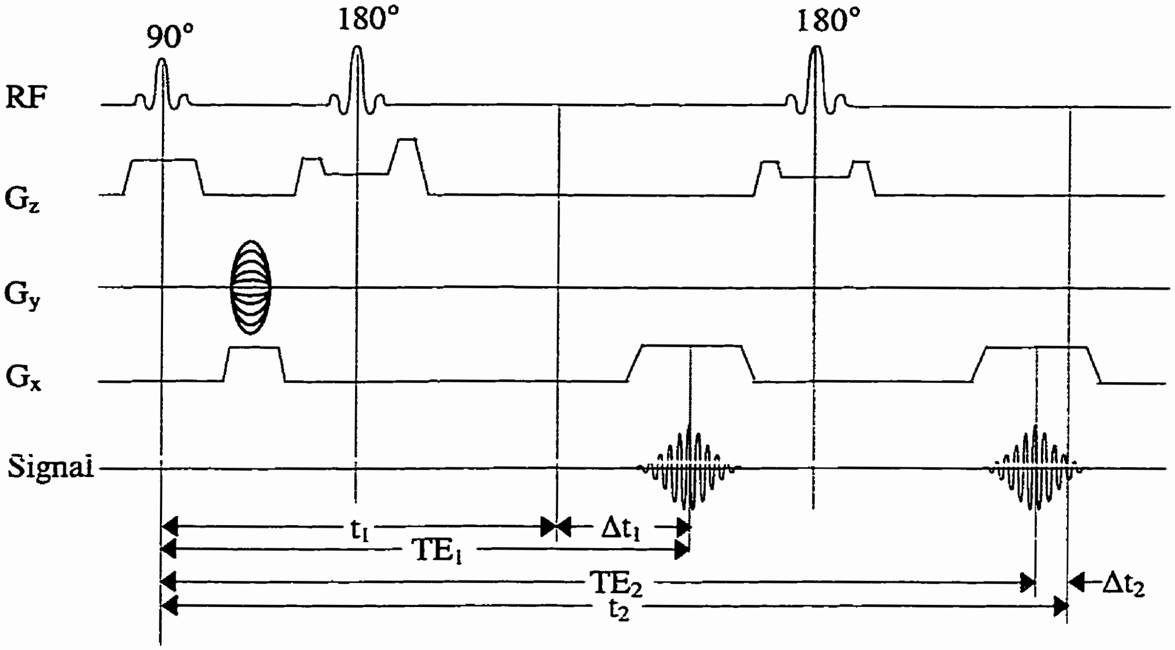

Figure 6-1 Pulse sequence for two-point water-fat imaging with MGE

The pulse sequence is shown in Figure 6-1. It is a spin-echo sequence with two echoes in each excitation. Two images from the two echoes have water-fat phase encoding scheme of $(180°, \alpha)$. Time t_1 and t_2 are the two Hahn echo positions, at which moments the water and fat magnetization vectors are in phase. The center of the first readout gradient and acquisition window are located at Δt_1 to the right side of the Hahn echo position t_1 so that the water and fat magnetization vectors have opposed phases at the first echo time TE_1. The time shift Δt_1 satisfies

$$\Delta\omega \, \Delta t_1 = \pi \tag{6-1}$$

where $\Delta\omega$ is the chemical shift between water and fat. The center of the second readout gradient and acquisition window are located at Δt_2 to the left side of the Hanh echo position t_2 so that the fat magnetization vector has a phase angle α with respect to that of water at the second echo time TE_2. The time shift Δt_2 satisfies

$$-\Delta\omega\,\Delta t_2 = \alpha \tag{6-2}$$

This sampling scheme can be labeled as (π, α). The two complex images I_1 and I_2 reconstructed from the two echoes can be written as

$$\begin{aligned} I_1 &= (W - F)\,P_1 \\ I_2 &= [W + \exp(i\alpha)\,F]\,P_2 \end{aligned} \tag{6-3}$$

where W and F are the magnitudes of water and fat; P_1 and P_2 are phasors due to field inhomogeneity and other systematic errors. In some cases, asymmetric k-space data is acquired and the associated complex images will have a linear phase ramp. The phase ramp can be removed from I_1 and I_2 by using the method described in equations (5-15) to (5-16). From the magnitudes of equations (6-3), W and F are found to have the following two possible sets of solutions

$$\begin{aligned} \hat{W} &= (\Delta I \pm |I_1|)/2 \\ \hat{F} &= (\Delta I \mp |I_1|)/2 \end{aligned} \tag{6-4}$$

where $\hat{W}$ and $\hat{F}$ are the solutions of W and F, respectively; The term ΔI is given by

$$\Delta I = \sqrt{\frac{2|I_2|^2 - (1-\cos\alpha)|I_1|^2}{1+\cos\alpha}} \tag{6-5}$$

The reason of introducing two new variables $\hat{W}$ and $\hat{F}$ is to make later derivation more clear. W and F represent the correct values of water and fat, while $\hat{W}$ and $\hat{F}$ represent our current water and fat solutions. It can be seen that $\hat{W} = W$ and $\hat{F} = F$ when the $(\hat{W}, \hat{F})$ assignment is correct; $\hat{W} = F$ and $\hat{F} = W$ when the $(\hat{W}, \hat{F})$ assignment is wrong. Different from the previous three-point methods, we do not have extra information to make a binary choice between the two possible solutions at the pixel level. Therefore, we temporarily take one solution as the correct result for each pixel. Next, a spin reversal filter is used to get the correct $(\hat{W}, \hat{F})$ assignment in the whole FOV.

6.3 Spin Reversal Filtering with Minimized Gradient Energy

A normalized orientation vector O is defined as

$$O = \mathrm{phasor}[I_1(\hat{W} - \hat{F})] \tag{6-6}$$

If the $(\hat{W}, \hat{F})$ assignment is correct, it can be derived from equations (6-3) that

$$O = P_1 \tag{6-7}$$

Therefore, the orientation vector O should be a spatially smooth phasor map. However, O has some sudden reversals due to wrong $(\hat{W}, \hat{F})$ assignments because the orientation vector O will be equal to $-P_1$ when the pixel has a wrong $(\hat{W}, \hat{F})$ assignment. This spin reversal filtering process is very similar to SRF used in TOP. The only difference is the consistency score S for each region, where the score S is calculated after orientation vectors O are unified in a region. Here, the consistency score S consists of two parts: S_1 and S_2. Score S_1 will be discussed first and S_2 will be introduced later. Score S_1 is defined as the total gradient energy of $\hat{P}_2$ in the region, where $\hat{P}_2$ is one of the two possible values of P_2. S_1 is given by

$$S_l = \sum_{\text{region}} \left(\left| \frac{\partial \hat{P}_2}{\partial x} \right|^2 + \left| \frac{\partial \hat{P}_2}{\partial y} \right|^2 \right) \tag{6-8}$$

where $\hat{P}_2$ can be calculated by

$$\hat{P}_2 = \text{phasor}\{I_2 * [\hat{W} + \exp(-i\alpha)\hat{F}]\} \tag{6-9}$$

After the orientation vector O is unified in one region by reversal filtering or localized phase unwrapping, as described in the previous chapter, the $(\hat{W}, \hat{F})$ assignments for all the pixels in the region could be all right or could be all wrong. As a result, $\hat{P}_2$ can be of two possible phasor maps, and thus, S_l has two possible values for the region. We have found that the smaller S_l value corresponds to the correct $(\hat{W}, \hat{F})$ assignment for the region. This conclusion has been tested by many experiments. The reason is as follows. According to equations (6-3) and (6-9), $\hat{P}_2$ is found to be

$$\hat{P}_2 = \begin{cases} P_2 & \text{when } (\hat{W}, \hat{F}) \text{ assignment is correct} \\ P_2 P_{WF} & \text{when } (\hat{W}, \hat{F}) \text{ assignment is wrong} \end{cases} \tag{6-10}$$

where P_{WF} is given by

$$P_{WF} = \text{phasor}\{[W + \exp(i\alpha)F][F + \exp(-i\alpha)W]\} \tag{6-11}$$

Therefore S_l is the total gradient energy of P_2 when $(\hat{W}, \hat{F})$ assignment is correct and that of P_2P_{WF} when $(\hat{W}, \hat{F})$ assignment is wrong. Since the detailed structures of P_2 and P_{WF} is very unlikely to be correlated, the total gradient energy of P_2P_{WF} can be shown to be roughly the sum of the total gradient energies of P_2 and P_{WF} [71]. Thus the total gradient energy P_2P_{WF} is generally greater than that of P_2. Hence, a smaller S_l corresponds to the correct $(\hat{W},\hat{F})$ assignment for the region. There are three conditions for the above gradient energy criterion to work. Firstly, α can not be 0 or π. When α is 0 or π, P_{WF} will be constant 1, thus P_2 and P_2P_{WF} will be the same. Secondly, the pixels in the region can not be pure water (pure fat is impossible) since pure water will result in a constant P_{WF}, consequently, the gradient energies of P_2 and P_2P_{WF} will be the same. Thirdly, the region has to have some structures, otherwise, the gradient energy of P_{WF} will be close to zero. This condition is usually satisfied in real human body imaging.

The other part of the consistency score, S_2, can give some help when S_1 fails to tell the difference between the two possible $(\hat{W},\hat{F})$ assignments. S_2 is the sum of $s_2(x,y)$ for all the pixels in the region

$$S_2 = \sum_{\text{region}} s_2(x,y) \qquad (6\text{-}12)$$

where $s_2(x,y)$ is defined as

$$s_2(x,y) = \begin{cases} 1 & \text{if } \hat{W}(x,y) > c\,\hat{F}(x,y) \\ -1 & \text{if } \hat{F}(x,y) > c\,\hat{W}(x,y) \\ 0 & \text{otherwise} \end{cases} \qquad (6\text{-}13)$$

The constant number c is chosen as 14 in our implementation. When $\hat{W}(x,y)$ is much larger than $\hat{F}(x,y)$, the pixel is probably pure water and the $(\hat{W},\hat{F})$ assignment for the pixel is probably correct. So S_2 is added by 1. When $\hat{F}(x,y)$ is much larger than $\hat{W}(x,y)$, the $(\hat{W},\hat{F})$ assignment for the pixel is probably wrong since there is no pure fat in a living tissue. This pixel should be pure water. Hence, this pixel has a -1 contribution to

S_2. When the $\hat{W}(x,y)$ and $\hat{F}(x,y)$ are not greatly different, this pixel has no contribution to S_2. When S_2 is greater than 0, it means the $(\hat{W},\hat{F})$ assignment for the whole region is probably correct. When S_2 is less than 0, it means the $(\hat{W},\hat{F})$ assignment for the whole region is probably wrong since there are more pixels in the region being probably wrong than being probably correct. The S_2 criterion works well in a region with a lot pixels being pure water.

The two consistency scores S_1 and S_2 can be normalized and combined together to give a comprehensive consistency score S which can be defined as

$$S = (S_1 - S_1') / (S_1 + S_1') + \lambda S_2 / N \qquad (6\text{-}14)$$

where S_1' is the other possible value of S_1, corresponding to the swapped $(\hat{W},\hat{F})$ assignments for the whole region; N is the total number of pixels in the region; λ is a constant, which can be chosen as 1.0 in a simple case. When the consistency score S is greater than zero, it means the $(\hat{W},\hat{F})$ assignment for the region is correct. When the consistency score S is less than zero, it means the $(\hat{W},\hat{F})$ assignment for the region is wrong and the $(\hat{W},\hat{F})$ assignments for all the pixels in the region need to be swapped.

6.4 Second Pass Solution

After SRF, the first pass water-fat solution is obtained. For the improvement of SNR, a second pass water-fat solution is calculated. In the SRF process, phasor maps P_1 and P_2 have already been calculated. P_1 is the final filtered O and P_2 is the correct $\hat{P}_2$ which is calculated in equations (6-9). Next, P_1 and P_2 are smoothed by weighted averaging with a standard $n \times n$ (e.g. 9×9) pixel sliding window. The smoothed phasors are removed from equations (6-3), resulting in the following phase corrected images

$$\begin{aligned} J_1 &= W - F \\ J_2 &= W + \exp(i\alpha) F \end{aligned} \tag{6-15}$$

where J_1 and J_2 are obtained by multiplying I_1 and I_2 with the complex conjugate of the appropriate phasors, respectively. Complex equations (6-15) can be split into the following real value equations

$$\begin{aligned} \mathrm{real}(J_1) &= W - F \\ \mathrm{real}(J_2) &= W + F\cos\alpha \\ \mathrm{imag}(J_2) &= F\sin\alpha \end{aligned} \tag{6-16}$$

These real value equations can be written in matrix form as

$$U = MV \tag{6-17}$$

where V is an unknown vector with elements W and F

$$V = \begin{pmatrix} W \\ F \end{pmatrix} \tag{6-18}$$

U is a known vector given by

$$U = \begin{pmatrix} \mathrm{real}(J_1) \\ \mathrm{real}(J_2) \\ \mathrm{imag}(J_2) \end{pmatrix} \tag{6-19}$$

M is a 3×2 matrix given by

$$M = \begin{pmatrix} 1 & -1 \\ 1 & \cos\alpha \\ 0 & \sin\alpha \end{pmatrix} \tag{6-20}$$

The LSE solution of equation (6-17) is given by

$$V = L\,U \tag{6-21}$$

In the above equation, L is a 2×3 matrix given by

$$L = (M^T M)^{-1} M^T \tag{6-22}$$

Equation (6-21) can be written more clearly as

$$\begin{pmatrix} W \\ F \end{pmatrix} = L \begin{pmatrix} \text{real}(J_1) \\ \text{real}(J_2) \\ \text{imag}(J_2) \end{pmatrix} \tag{6-23}$$

From equation (6-23), W and F can be calculated numerically and output as the final water and fat images.

Now, we want to calculate the NSA* of the second pass water-fat solution. Equation (6-23) can be expanded to

$$\begin{aligned} W &= L_{1,1}\,\text{real}(J_1) + L_{1,2}\,\text{real}(J_2) + L_{1,3}\,\text{imag}(J_2) \\ F &= L_{2,1}\,\text{real}(J_1) + L_{2,2}\,\text{real}(J_2) + L_{2,3}\,\text{imag}(J_2) \end{aligned} \tag{6-24}$$

where $L_{m,n}$ is the matrix element of L at the mth row and nth column. The phase corrected images J_1, J_2, and J_3 have the same noise variances as their original counterparts I_1, I_2, and I_3, i.e. $\sigma_1^2 = \sigma_2^2 = \sigma_3^2 = \sigma_0^2$, because the noise variances in phasor maps P_0, P_0P_1, and $P_0P_1^2$ are greatly reduced by heavy smoothing operations. Hence, the noise variances of the real part and imaginary part of J_1, J_2, and J_3 are $\sigma_0^2 / 2$. Because the noises in the real part and imaginary part of J_1, J_2, and J_3 are independent of each other, the noise variance in W, σ_W^2, and the noise variance in F, σ_F^2, are given by

$$\begin{aligned} \sigma_W^2 &= (L_{1,1}^2 + L_{1,2}^2 + L_{1,3}^2)(\sigma_0^2 / 2) \\ \sigma_F^2 &= (L_{2,1}^2 + L_{2,2}^2 + L_{2,3}^2)(\sigma_0^2 / 2) \end{aligned} \tag{6-25}$$

From analytical derivation, it can be proved that σ_W^2 is always equal to σ_F^2. Therefore, NSA* of the water image and fat image can both be calculated by

$$\begin{aligned}\mathrm{NSA}^* &= \frac{1}{\sigma_W^2/(\sigma_0^2/2)} \\ &= \frac{1}{L_{1,1}^2+L_{1,2}^2+L_{1,3}^2} \\ &= \frac{6-2\cos\alpha}{(\cos\alpha-3)^2(1+\cos\alpha)}\end{aligned} \tag{6-26}$$

The curve of NSA* versus phase angle α is plotted in Figure 6-2 below.

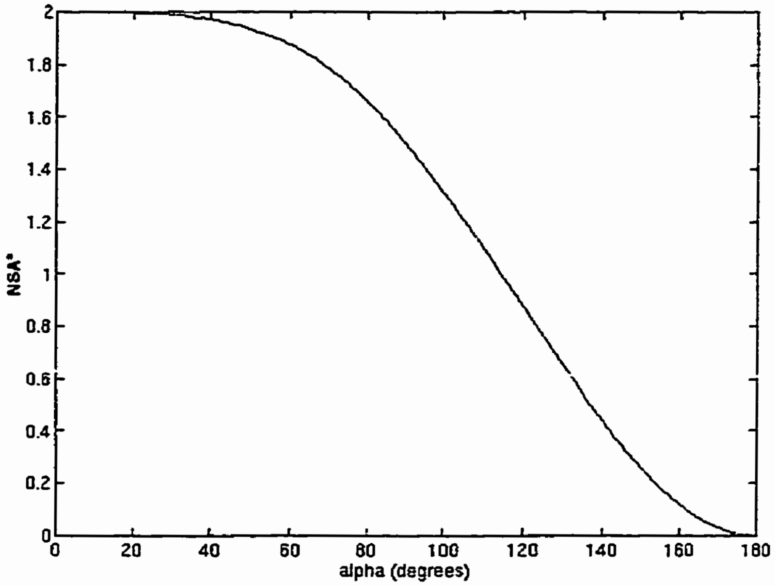

Figure 6-2 NSA* curve as a function of phase angle α.

6.5 Experimental

For the reason of gradient energy performance and image SNR, a (180°,–45°) sampling scheme was adopted in our experiments. The NSA* of the final water and fat images are 1.95 which is very close to 2.0. The experiments were performed on a 0.5T GE SIGNA scanner. A standard spin-echo sequence with double echoes were modified to realized the (180°,–45°) sampling scheme by shifting the two 180° RF pulses. The time shift Δt_1 was set to be 3.356ms and Δt_2 was 0.840ms. Complex image data were saved and processed on UNIX based workstations. The algorithm was coded in the C and C++

programming language. It takes 10-15 seconds to generate a pair of water and fat images. The operations are summarized as the following steps

- Remove linear phase ramps in the original two images if necessary
- Find 2 sets of possible solutions for water and fat
- Spin reversal filtering with minimized gradient energies for the phasor map P_2
- Remove smoothed P_1 and P_2 from I_1 and I_2 to obtain phase corrected images J_1 and J_2
- Find the final W & F images by real value LSE method

6.6 Results

Images of volunteers each of 6-8 slices were acquired. The results were all successful. Some of the representative results are shown below

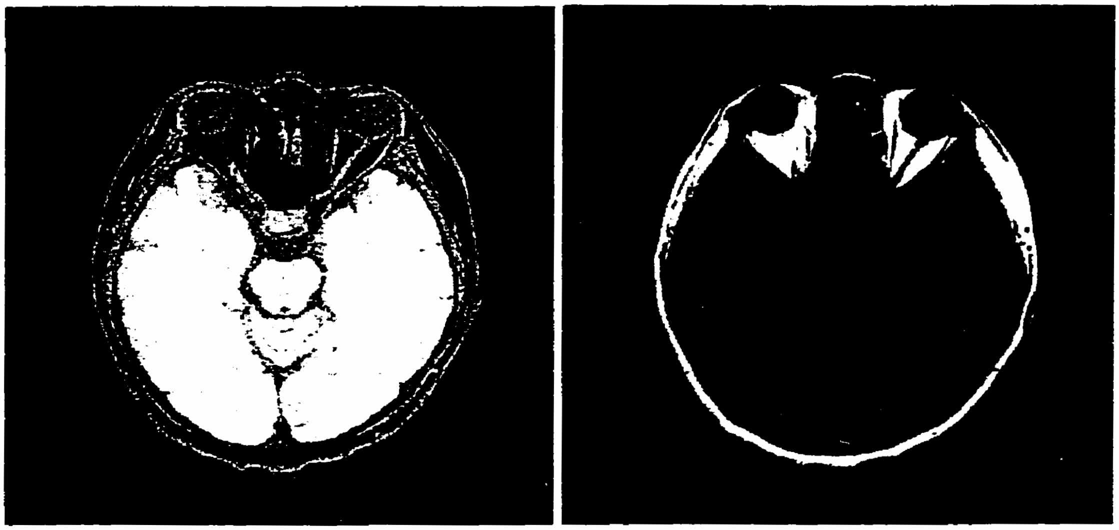

(a) (b)

Figure 6-3 Transverse water (a) and fat (b) images of a human head acquired at 0.5 T. Spin-echo, 2 echoes, TR=500ms, TE_1=20ms, TE_2=42ms. Sampling scheme (180°,–45°).

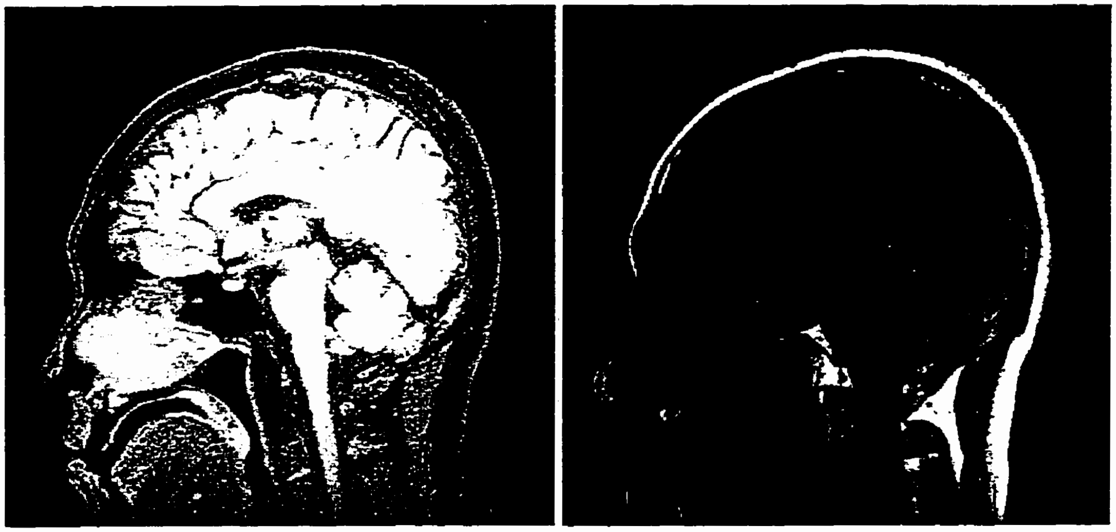

(a) (b)

Figure 6-4 Sagittal water (a) and fat (b) images of a human head acquired at 0.5 T. Spin-echo, 2 echoes, TR=500, TE_1=20ms, TE_2=42ms. Sampling scheme (180°,–45°).

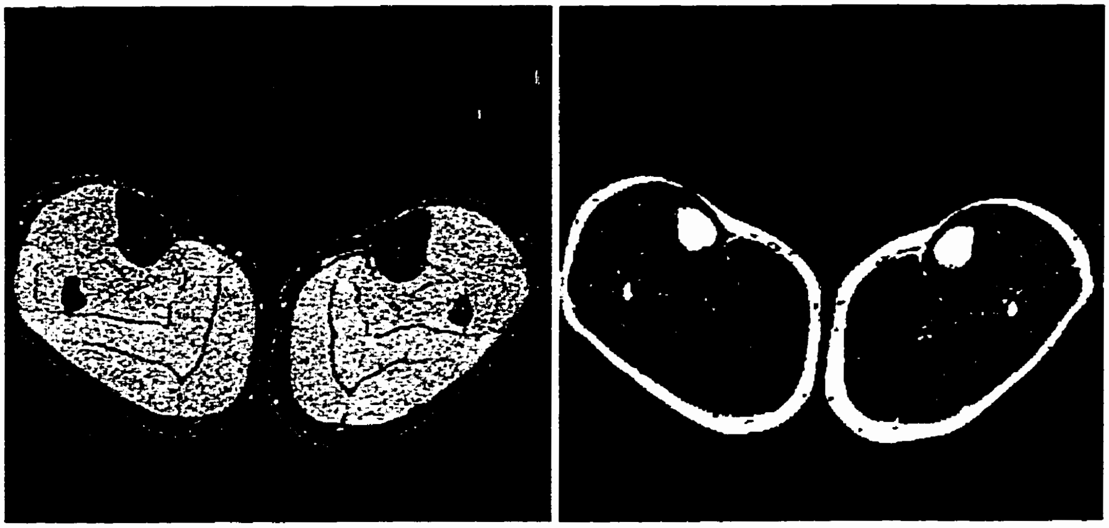

(a) (b)

Figure 6-5 Transverse water (a) and fat (b) images of legs acquired at 0.5 T. Spin-echo, 2 echoes, TR=500ms, TE_1=20ms, TE_2=42ms. Sampling scheme (180°,–45°).

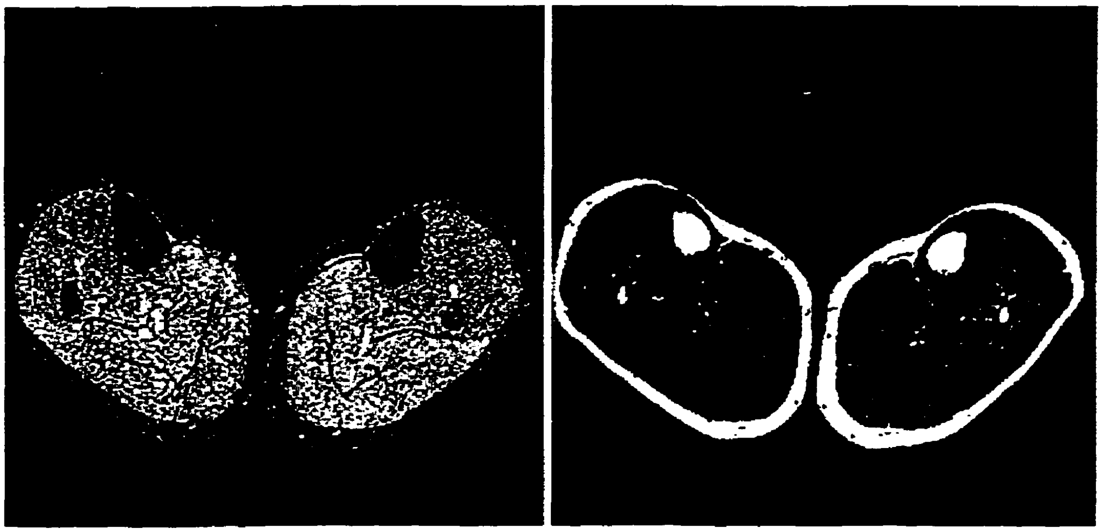

(a) (b)

Figure 6-6 Sagittal water (a) and fat (b) images of a human head acquired at 0.5 T. Spin-echo, 2 echoes, TR=1000ms, TE_1=20ms, TE_2=120ms. Sampling scheme (180°,−45°).

6.7 Discussion

This unparalleled two-point sampling scheme allows the use of gradient energy of the phasor map to help determine the water-fat assignments in a whole region. The order/connectivity problem, which is still bothering other two-points methods, are solved. The assumption that the structures in the phasor map P_1 and the structures in water and fat tissues are very much uncorrelated has been proved by imaging different parts of the human body. The SRF filter with minimized gradient energy has been proved to be robust. The score S_1, which is related to the gradient energy difference, is maximized when α is chosen to be ±90°. However, The SNR of the water and fat images are not optimal when α is chosen to be ±90°. The (180°,−45°) sampling scheme is a good balance between good S_1 score and optimal image SNR.

CHAPTER 7

CHEMICAL SHIFT IMAGING WITH SPECTRUM MODELING (CSISM)

7.1 Introduction

In Fourier transform based chemical shift imaging (CSI) techniques, spectral resolution is realized by frequency encoding and spatial resolution is accomplished by multi-dimensional phase encoding which takes an extremely long scan time for a good spatial resolution [18,19]. To reduce imaging time, CSI experiments with low spatial resolution are often performed. However, low spatial resolution may degrade the spectral resolution due to larger B_0 inhomogeneity per pixel, partial volume and truncation artifacts. Furthermore, automatic spectrum quantification for each pixel is complicated, unreliable, and time consuming, thus has major limitations.

Dixon [22] first modeled fat and water in tissue as two rotating vectors and made it possible to obtain separated fat and water images with only two spin-echo data acquisitions. Based on the Dixon model, DPE [60,61] resolves fat and water pixel by pixel without ambiguity, in the presence of field inhomogeneity errors.

Chemical shift imaging with spectrum modeling (CSISM) [72] is a generalization of DPE, which can output separate images of different chemical components with only several spin-echo data acquisitions. CSISM achieves high scan time efficiency by modeling the NMR spectra of the sample as several peaks with known resonance frequencies and unknown peak amplitudes before the data acquisitions are performed.

7.2 Data Acquisition and First Pass Solution

When a sample is given, one or several localized NMR spectroscopy experiments can be performed to obtain the NMR spectra of the sample. Every primary peak in the spectra is associated with a certain chemical component. It is reasonable to model the spectrum for every voxel in the sample as several delta-function shaped peaks with known resonance frequencies but unknown amplitudes. This is equivalent to say that every voxel in the sample consists of several chemical components and all the components have fixed chemical shift values and no line broadening. Based on this model, several spin-echo images are collected with the 180° refocusing pulse shifted a different amount of time for every image. As a result, the magnetization vectors of the chemical components are put into different orientations across these spin-echo images. If the images are properly collected, the amplitudes of the magnetization vectors for different chemical components can be resolved from these complex images. Assume we found N peaks in the spectrum of the sample with angular frequency shifts being $\delta\omega_1, \delta\omega_2, ..., \delta\omega_N$, respectively. Then, we can model each voxel as being composed of N distinctive chemical components with their magnetization vectors revolving clockwise at angular frequencies $\delta\omega_1, \delta\omega_2, ..., \delta\omega_N$ in the rotating frame of reference. The unknown amplitudes of these N magnetization vectors are labeled as $X_1, X_2, ..., X_N$, respectively. In order to resolve these unknown amplitudes, K spin-echo images $I_1, I_2, ..., I_K$ are acquired with the 180° refocusing pulse shifted by $M_1\Delta t, M_2\Delta t, ..., M_K\Delta t$, respectively, where Δt is the minimum time shift unit and $M_1, M_2, ..., M_K$ are integers with M_1 equal to zero. A sketch of the pulse sequence is shown in Figure 7-1.

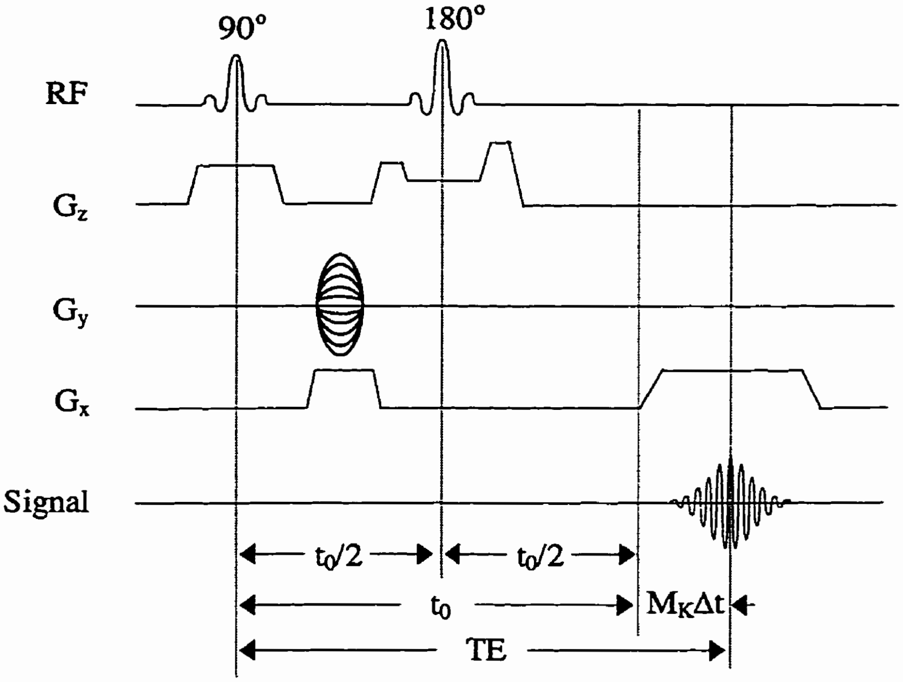

Figure 7-1 Pulse sequence for CSISM

The acquired K complex images can be expressed as

$$\begin{aligned} I_1 &= (X_1 + X_2 + \cdots + X_N)P_0 \\ I_2 &= (A_1^{M_2}X_1 + A_2^{M_2}X_2 + \cdots + A_N^{M_2}X_N)P_0P_1^{M_2} \\ &\vdots \\ I_K &= (A_1^{M_K}X_1 + A_2^{M_K}X_2 + \cdots + A_N^{M_K}X_N)P_0P_1^{M_K} \end{aligned} \tag{7-1}$$

where A_n, with n = 1, 2, ..., or N, is a known phasor given by

$$A_n = \exp(-i\ \delta\omega_n \Delta t) \tag{7-2}$$

which represents the orientation of the nth magnetization vector in the rotating frame at the unit time shift Δt. Hence the phasor $A_n^{M_k}$, with k = 1, 2, ..., or K, represents the orientation of the nth magnetization vector in the kth image which is acquired with a time shift $M_k\Delta t$. The parameter P_0 is a phasor map due to phase errors caused by factors such as RF field inhomogeneity or data acquisition window off-centering. The phasor map P_0

is a constant across the K images for a given pixels. Parameter P_1 is a phasor map caused by field inhomogeneity error and it is given by

$$P_1 = \exp(-i\gamma \Delta B_0 \Delta t) \tag{7-3}$$

where γ is the averaged gyro-magnetic ratio of the N chemical components; ΔB_0 is the field inhomogeneity map. The term $P_1^{M_k}$ in equations (7-1) represents the phase error caused by field inhomogeneity in the kth image which has a time shift $M_k\Delta t$. Because X_1, X_2, ..., X_N should have non-negative real values, P_0 is simply the phasor of I_1 and can be removed from equations (7-1). To reduce noise, P_0 can be calculated as the phasor of smoothed I_1 by a small sliding window (e.g. 7×7 pixels). By multiplying P_0^* to I_1, I_2, ..., and I_K respectively, phase corrected images J_1, J_2, ..., J_K are obtained. Equations (7-1) are transformed into

$$\begin{aligned} J_1 &= X_1 + X_2 + \cdots + X_N \\ J_2 P_1^{-M_2} &= A_1^{M_2} X_1 + A_2^{M_2} X_2 + \cdots + A_N^{M_2} X_N \\ &\vdots \\ J_K P_1^{-M_K} &= A_1^{M_K} X_1 + A_2^{M_K} X_2 + \cdots + A_N^{M_K} X_N \end{aligned} \tag{7-4}$$

Except the first equation in equations (4), all the other equations are complex value equations. Equations (7-4) can be split into 2K-1 real value equations

$$\begin{aligned} J_1 &= (X_1 + X_2 + \cdots + X_N) \\ \mathrm{real}(J_2 P_1^{-M_2}) &= \mathrm{real}(A_1^{M_2}) X_1 + \mathrm{real}(A_2^{M_2}) X_2 + \cdots + \mathrm{real}(A_N^{M_2}) X_N \\ \mathrm{imag}(J_2 P_1^{-M_2}) &= \mathrm{imag}(A_1^{M_2}) X_1 + \mathrm{imag}(A_2^{M_2}) X_2 + \cdots + \mathrm{imag}(A_N^{M_2}) X_N \\ &\vdots \\ \mathrm{real}(J_K P_1^{-M_K}) &= \mathrm{real}(A_1^{M_K}) X_1 + \mathrm{real}(A_2^{M_K}) X_2 + \cdots + \mathrm{real}(A_N^{M_K}) X_N \\ \mathrm{imag}(J_K P_1^{-M_K}) &= \mathrm{imag}(A_1^{M_K}) X_1 + \mathrm{imag}(A_2^{M_K}) X_2 + \cdots + \mathrm{imag}(A_N^{M_K}) X_N \end{aligned} \tag{7-5}$$

where operators "real" and "imag" represent taking the real part and imaginary part of a complex number, respectively. In equations (7-5), there are N+1 unknown variables: P_1 and X_1, X_2, ..., X_N. If the number of equations 2K-1 is no less than the number of unknowns N+1, it is possible to solve equations (7-5) which can be expressed in matrix form as

$$Y(P_1) = AX \tag{7-6}$$

where X is an unknown N-dimensional vector

$$X = \begin{pmatrix} X_1 \\ X_2 \\ \vdots \\ X_N \end{pmatrix} \tag{7-7}$$

$Y(P_1)$ is a (2K-1) dimensional vector

$$Y(P_1) = \begin{pmatrix} J_1 \\ \mathrm{real}(J_2 P_1^{-M_2}) \\ \mathrm{imag}(J_2 P_1^{-M_2}) \\ \vdots \\ \mathrm{real}(J_K P_1^{-M_K}) \\ \mathrm{imag}(J_K P_1^{-M_K}) \end{pmatrix}, \tag{7-8}$$

A is a (2K-1) × N matrix

$$A = \begin{pmatrix} 1 & 1 & \cdots & 1 \\ \mathrm{real}(A_1^{M_2}) & \mathrm{real}(A_2^{M_2}) & \cdots & \mathrm{real}(A_N^{M_2}) \\ \mathrm{imag}(A_1^{M_2}) & \mathrm{imag}(A_2^{M_2}) & \cdots & \mathrm{imag}(A_N^{M_2}) \\ \vdots & \vdots & \vdots & \vdots \\ \mathrm{real}(A_1^{M_K}) & \mathrm{real}(A_2^{M_K}) & \cdots & \mathrm{real}(A_N^{M_K}) \\ \mathrm{imag}(A_1^{M_K}) & \mathrm{imag}(A_2^{M_K}) & \cdots & \mathrm{imag}(A_N^{M_K}) \end{pmatrix} \tag{7-9}$$

We start solving the nonlinear equations (7-9) by fitting P_1 whose magnitude is always 1 and its phase angle ranges from $-\pi$ to π. Typically, 360 different testing angles with 1°

increment per step are tried out for the phase angle of P_1. For each given P_1, equation (7-6) becomes linear equation of X whose least square error (LSE) solution is given by

$$X = L\,Y(P_1) \tag{7-10}$$

where L is a $N \times (2K-1)$ matrix given by

$$L = (A^T A)^{-1} A^T \tag{7-11}$$

where operator "T" represents the transpose of a matrix and operator "-1" represents the inverse of a matrix. The least-square errors LSE for different values of P_1 can be calculated by

$$\begin{aligned} LSE &= \text{energy}[Y(P_1) - AX] \\ &= \text{energy}[Y(P_1) - A(A^T A)^{-1} A^T Y(P_1)] \\ &= \text{energy}\{[U - A(A^T A)^{-1} A^T]\,Y(P_1)\} \end{aligned} \tag{7-12}$$

where operator "energy" returns the square sum of all the elements of a vector; U is a $(2K\text{-}1) \times (2K\text{-}1)$ unit matrix. Different P_1 values usually result in different LSE values. The P_1 value with minimum LSE is selected as the correct answer for P_1, and the associated solution of X is the correct result for the peak amplitudes.

The results for P_1 and X from the fitting process are reliable for pixels with balanced peak amplitudes. For pixels with only one chemical component or insufficient number of chemical components, the results for P_1 and X are not reliable. From equation (7-12), it is not difficult to see that LSE is a polynomial function of $\cos(\Theta)$ and $\sin(\Theta)$, where Θ is the phase angle of P_1. Therefore, a curve of LSE versus the phase angle of P_1 is a smooth curve with limited number of local minimums. For a pixel with balanced peak amplitudes, the minimum value of LSE is significantly smaller than the other local minimums on the curve. Thus, it is easy to find the correct phase angle of P_1. For a pixel with a single peak or insufficient number of peaks, the values of several local minimums will be very close. Thus, it is often impossible to tell which local minimum corresponds to the correct phase angle of P_1. To help illustrating the above statements, two plots of LSE versus the phase angle of P_1 from a CSISM experiment are shown in Figure 7-2.

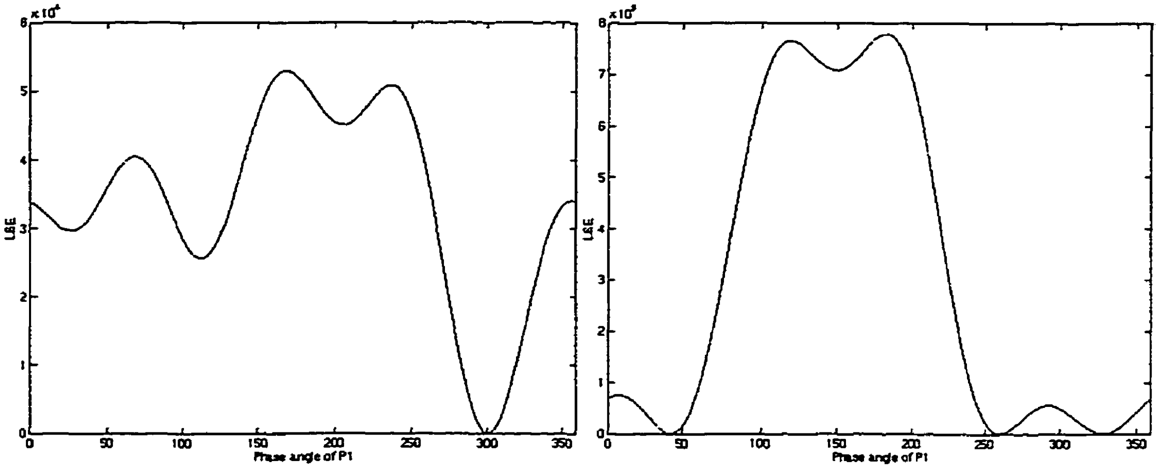

(a) (b)

Figure 7-2 Plots of LSE versus the phase angle of P_1, in a pixel with two chemical components (a), and a pixel with a single chemical component (b). The sample has three chemical components. Three complex images were acquired.

From the two curves in Figure 7-2, we can easily tell which pixel has more reliable results for P_1 and X. To mathematically evaluate the reliability of the results for a pixel, a score S is calculated for the pixel by the following procedure. First, all the local minimums are identified by checking the testing phase angles of P_1 one by one. If the LSE value of a phase angle is smaller than or equal to the LSE value of its left neighbor and right neighbor, the LSE value at this phase angle is a local minimum. To avoid having extra local minimums due to round off errors, no other local minimums are allowed in the proximity of an existing local minimum. Second, the global minimum and second minimum values are sorted out from the local minimums. The minimum value is labeled as LSE_1 and the second minimum value is labeled as LSE_2. Third, a score S is calculated for this pixel

$$S = (LSE_2 - LSE_1)/(E + C) \qquad (7\text{-}13)$$

where E is the total energy of vector Y, i.e. the square sum of all the elements of Y; C is a constant which can be chosen to be 10 times the averaged energy of vector Y for the pixels in the background noise. A pixel of noise can be roughly determined by checking its phase coherence with its neighboring pixels in the in-phase image I_1. When S is large, the results from the fitting process are reliable, and vice versa.

In addition to the single peak or insufficient peaks problem, the computation time for the fitting process is also too long. To solve these two problems, a process of combined region-growing and fitting is adopted. Initially, a small number of pixels, which distributed uniformly in the whole FOV (e.g. one pixel in every 8×8 pixels) except the regions of background noise, are picked as original seeds. The above fitting process is performed for each of these original seeds to calculate P_1 and score S. Then, the original seeds are sorted into an array with their scores in a descending order. The growing process begins from the original seed which has the highest score S. To avoid growing in noise, phase differences between the seed and its 4-connected neighboring pixels in the in-phase image I_1 are calculated. If the phase difference between the seed and a neighboring pixel is out of a range (e.g. $\pm 10^\circ$), the neighboring pixel is discarded and will not be "grown" by this seed. On the other hand, if the phase difference between the seed and a neighboring pixel is within the range, the neighboring pixel qualifies to be grown, as a result, P_1 and LSE values for the neighboring pixel will be calculated. With the P_1 value for the seed previously determined, the P_1 value for a neighboring pixel is quickly obtained by fitting the phase angle of P_l in a small range (e.g. $\pm 10^\circ$) around the phase angle of the seed, since P_l should be a fairly smooth phasor map. After P_l and minimum least square error LSE_l are obtained, an error ratio R is calculated for the neighboring pixel

$$R = LSE_l /(E + C) \qquad (7\text{-}14)$$

where E and C are same defined as in equation (13). The P_l value for the neighboring pixel is more reliable when R is smaller. The R values for the grown neighboring pixels are added to an empty red-black tree. The grown pixels are labeled as “visited” to prevent from being grown again. For the second round of growth, a newly grown pixel with minimum R is searched out from the red-black tree and acts as the seed for this round of growth. In each round of growth, there is only one seed. Four neighboring pixels of the seed are checked to see if they can be grown. If a neighboring pixel is phase coherent with the seed and has not been "visited" before, it is grown and its R value is added to the red-black tree. From searching the red-black tree, a pixel with the smallest R value is selected as the seed for the next round of growth and its R value is removed from the red-black tree. This growing process continues until the red-black tree becomes empty.

The grown pixels from one original seed usually covers one piece of isolated tissue. There can be many pieces of isolated tissue in the whole FOV. In order to cover the whole FOV, the original seed with the second highest score is selected to start a new growth if the original seed has not been “visited” by the previous growths. All the original seeds will be gone through according to their order of score S. After the growing process stops, tissue in the whole FOV should be covered. Some left over pixels in the background noise will not affect our result. From the growing process, we obtain the P_1 map in the whole FOV.

7.3 Second Pass Solution

The images of all the X elements can be obtained from the above process of region growing and fitting. For the improvement of image SNR, however, a second pass solution of X is calculated. First, P_1 map is weighted smoothed with a small sliding window (e.g. 9×9 in size) to reduce the noise level in P_1. There will not be much useful information loss since P_1 should be a smooth phasor map after all. The weighting for each pixel in the smoothing operation is chosen to be the magnitude of image I_1. The smoothed P_1 map is substituted into equation (7-8) and the second pass solution X is directly given by equation (7-10). The images of the elements of X are output as the spectroscopic images.

Now, we want to calculate the NSA* of the second pass spectroscopic images. Assume the original complex images I_1, $I_2, \cdots, I_K$ have equal noise variances of σ_0^2. Then, the noise variances in the real part and imaginary part of the images are $\sigma_0^2/2$. Because the noise variances in P_0 and P_1 are greatly reduced by heavy smoothing operations, The noise variances for the elements of Y, given in equation (7-8), are all approximately $\sigma_0^2/2$. Based on equation (7-10) and the fact that the noises in the elements of Y are independent to each other, the noise variance for the first element of X, $\sigma_{X_1}^2$ can be calculated by

$$\sigma_{X_1}^2 = \sum_{k=1}^{2K-1} L_{1,k}^2 \sigma_0^2 / 2 \qquad (7\text{-}15)$$

where $L_{1,k}$ is the matrix element of L at the first row and kth column. From numerical calculation or analytical derivation, it can be proved that $\sigma_{X_n}{}^2$, for n=1 to N, are all equal to $\sigma_{X_1}{}^2$. Therefore, NSA* of all the chemical shift images can be calculated by

$$\begin{aligned} NSA^* &= \frac{1}{\sigma_{X_1}{}^2 / (\sigma_0{}^2 / 2)} \\ &= 1 / (\sum_{k=1}^{2K-1} L_{1,k}{}^2) \end{aligned} \tag{7-16}$$

Overall, the major operations in CSISM are summarized in the following flowchart

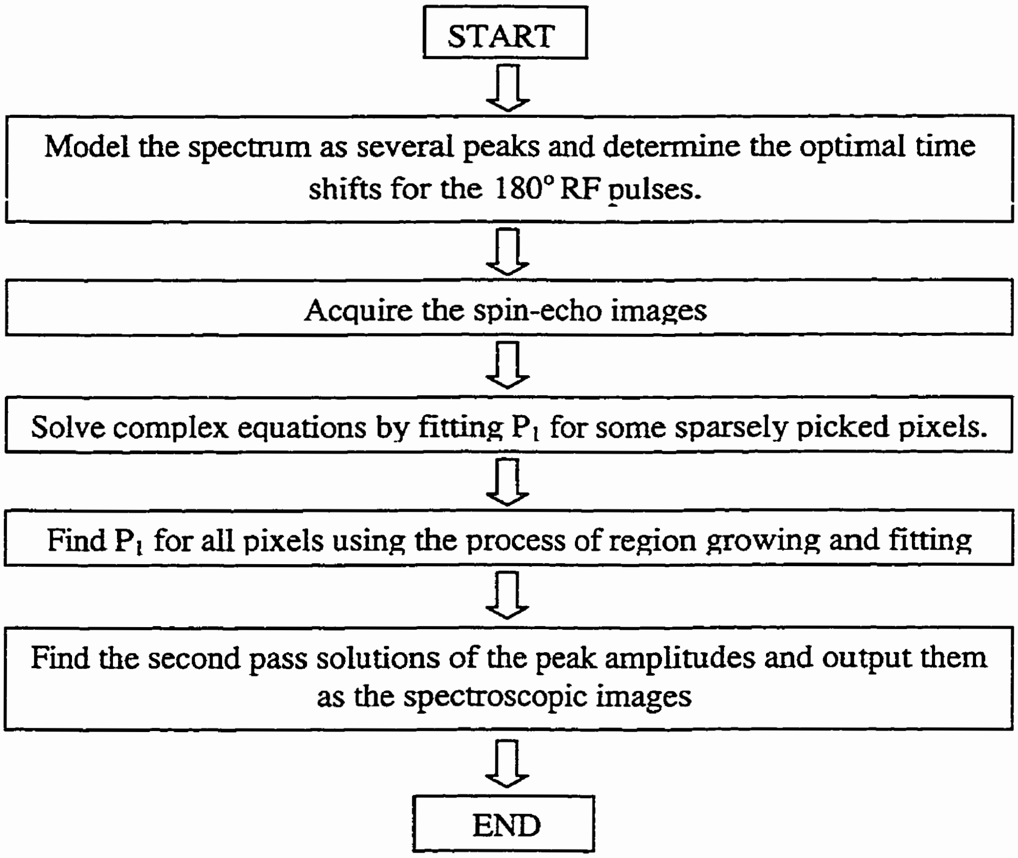

Figure 7-3 Flowchart of the CSISM operations

7.4 Experimental and Results

Experiments on an ethanol (CH_3CH_2OH) phantom were performed on a 1.5T GE SIGNA scanner. A localized spectroscopy was conducted prior to imaging to measure the peak frequencies for ethanol. The reconstructed spectrum is shown in Figure 7-4

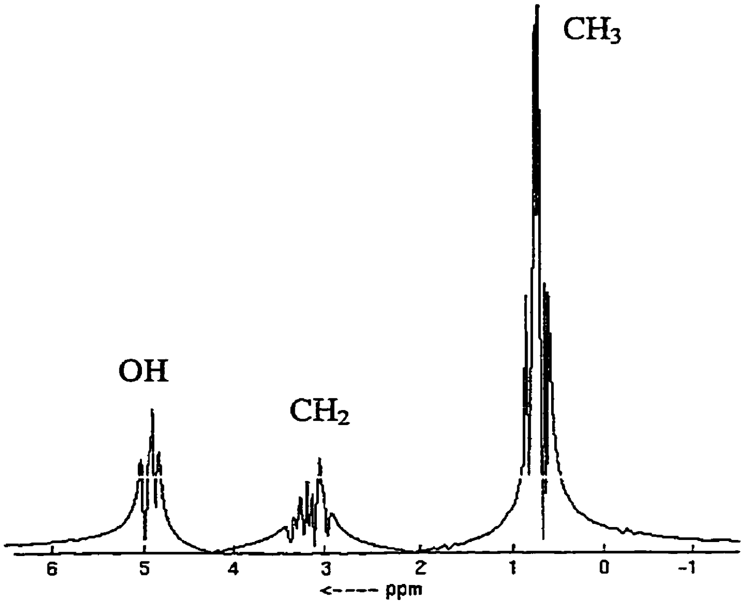

Figure 7-4 Localized NMR spectrum of ethanol (CH_3CH_2OH)

If we assume the Larmor frequency of CH_3 is 0 Hz in the rotating frame, the angular frequencies of the three peaks will given by $\delta\omega_1 = 2\pi \times 0\,\text{Hz}$ (CH_3), $\delta\omega_2 = 2\pi \times 156\,\text{Hz}$ (CH_2), and $\delta\omega_3 = 2\pi \times 267\,\text{Hz}$ (OH). Four spin-echo images were acquired with the 180° RF pulse shifted 0.000, 0.848, 1.696, and 2.544 ms. For simplicity, these numbers were selected to make the time shift $M_k\Delta t$ linearly increasing, i.e. M_1=0, M_2=1, M_3=2, and M_4=3. The unit time shift Δt is so chosen that the reciprocal condition number of matrix A^TA is as large as possible while keeping Δt as small as possible. A plot of reciprocal condition number of A^TA versus Δt is plotted in Figure 7-5 (a).

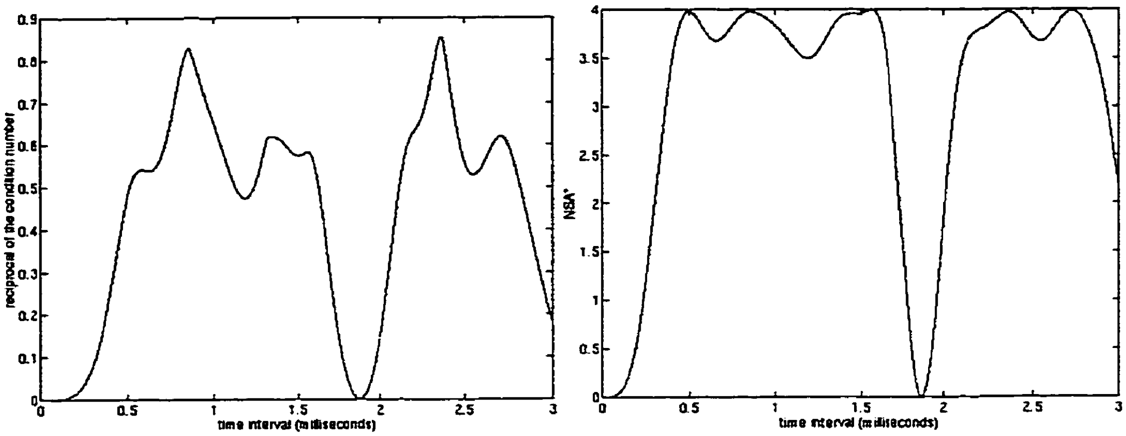

(a) (b)

Figure 7-5 Plots of the reciprocal condition number of A^TA versus Δt (a), and NSA* versus Δt (b)

At Δt=0.848, the reciprocal condition number is 0.82. The values of NSA* for different Δt values are calculated using equation (16) and plotted in Figure 5 (b). At Δt=0.848, the NSA* is 3.97 which is very close to 4.0. Therefore, the SNR for this four point sampling scheme is very close to be optimal. Complex images from the scans were saved and processed on UNIX based workstations (Sun Sparc 10, Sun Microsystems, Mountain View, CA; and DEC 3000/400, Digital Equipment Corporation, Maynard, MA) The algorithm was coded in the C and C++ programming language. The plots were drawn using Matlab package. A set of representative spectroscopic images of ethanol is shown in Figure 7-6. The peak amplitudes are in agreement with the results from localized spectroscopy plotted in Figure 7-4.

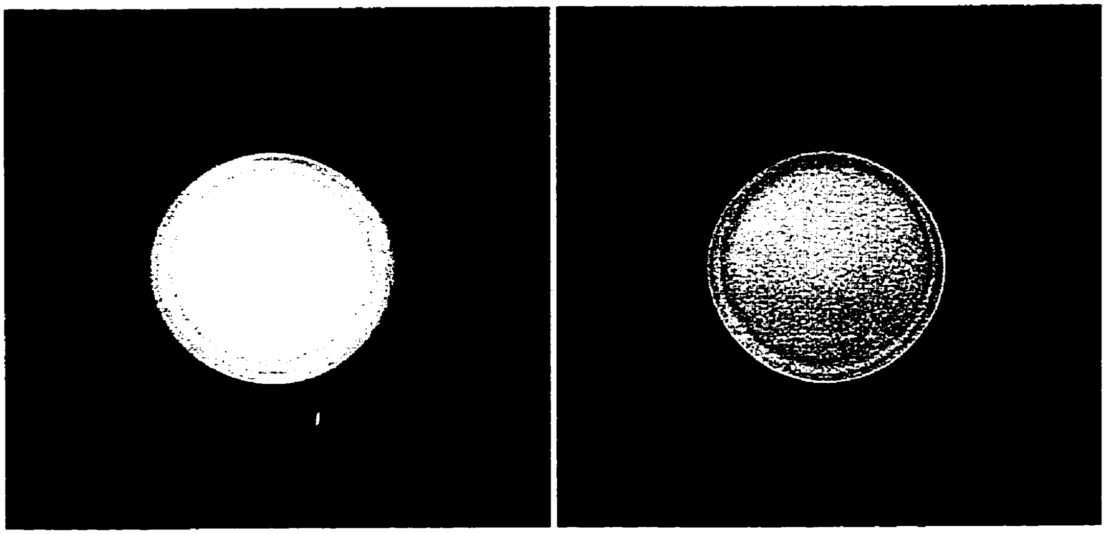

(a) In-phase image

(b) CH_3 image

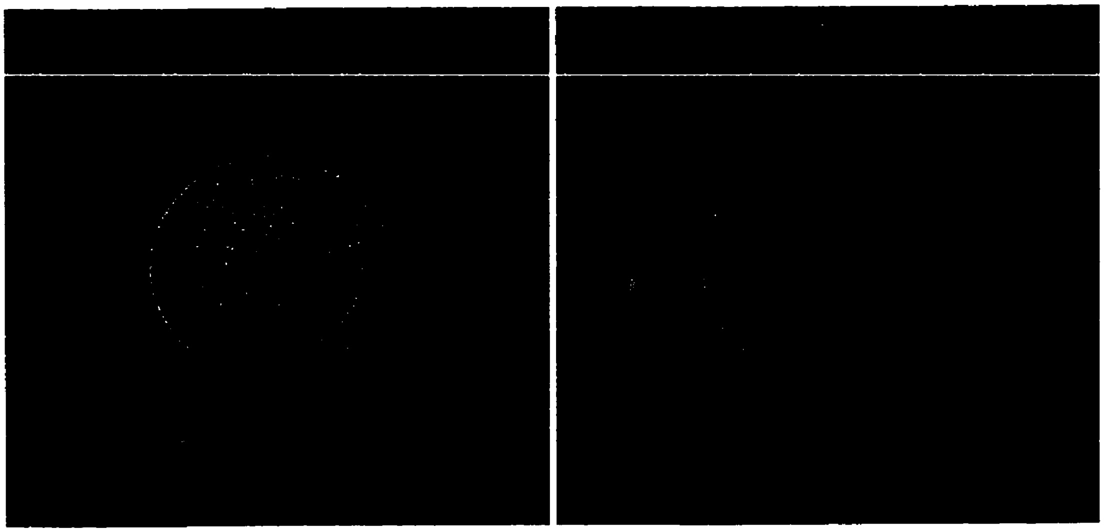

(c) CH_2 image

(d) OH image

Figure 7-6 Spectroscopic images of ethanol acquired at 1.5 T. Spin-echo, TR=500ms, TE=20ms.

We have found that water-fat-silicone imaging is a practical application of CSISM for patients with silicon implants in breasts. Three acquisitions will be enough to reconstruct a set of water fat and silicone images. Doctors at a local hospital did a muti-slice (22 slices) water-fat imaging with a DPE sampling scheme of $(0°,90°,180°)$. The water-fat results had some problems because the patient has silicone implants in her breasts. By using CSISM, we were able to reconstruct water-fat-silicone images successfully for most of the slices. We assume the chemical shift between water and fat is 3.5 ppm, and the chemical shift between fat and silicone is 1.7 ppm [73]. The order of the Larmor frequencies is water, fat, and silicone with silicone having the lowest Larmor frequency. A representative water-fat-silicone result is shown in Figure 7-7

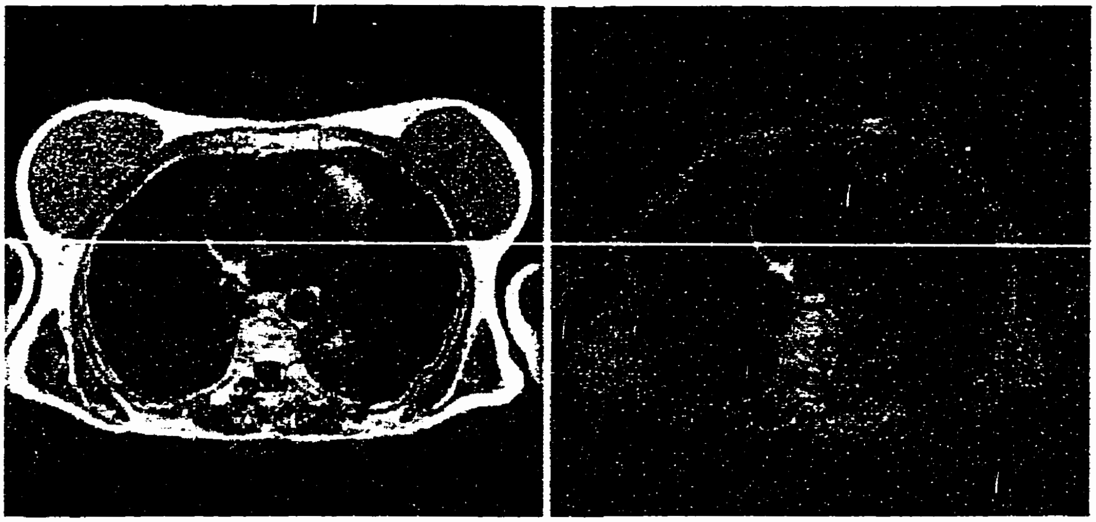

(a) In-phase image (b) Water image

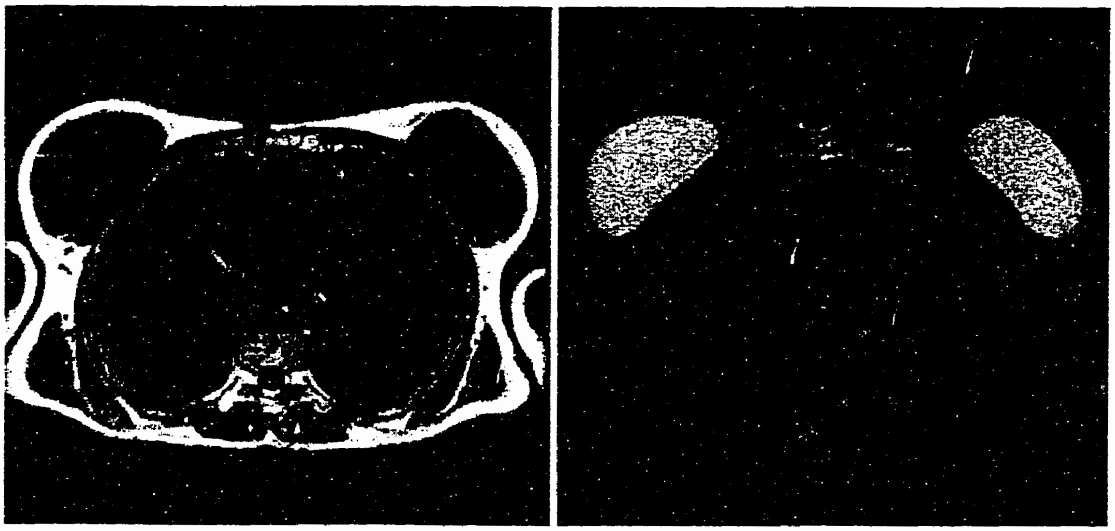

(c) Fat image (d) Silicone image

Figure 7-7 Transverse images of woman breasts with silicone implants acquired at 0.5 T. Spin-echo, TR=500ms, TE=20ms.

We have also performed some water-fat-silicone experiments on a 1.5 T scanner. A phantom of pork and silicone implant was used in the experiments. Before imaging, localized NMR spectroscopy experiments were performed to measure the chemical shifts. If we define the chemical shift for silicone to be 0 ppm, then the chemical shift for fat is 1.2 ppm and the chemical shift for water is 4.7 ppm. Three spin-echo images were acquired with the 180° RF pulse shifted 0.000, 1.34, and 2.68 ms. The spectroscopic images are excellent. A representative water-fat-silicone result is shown in Figure 7-8

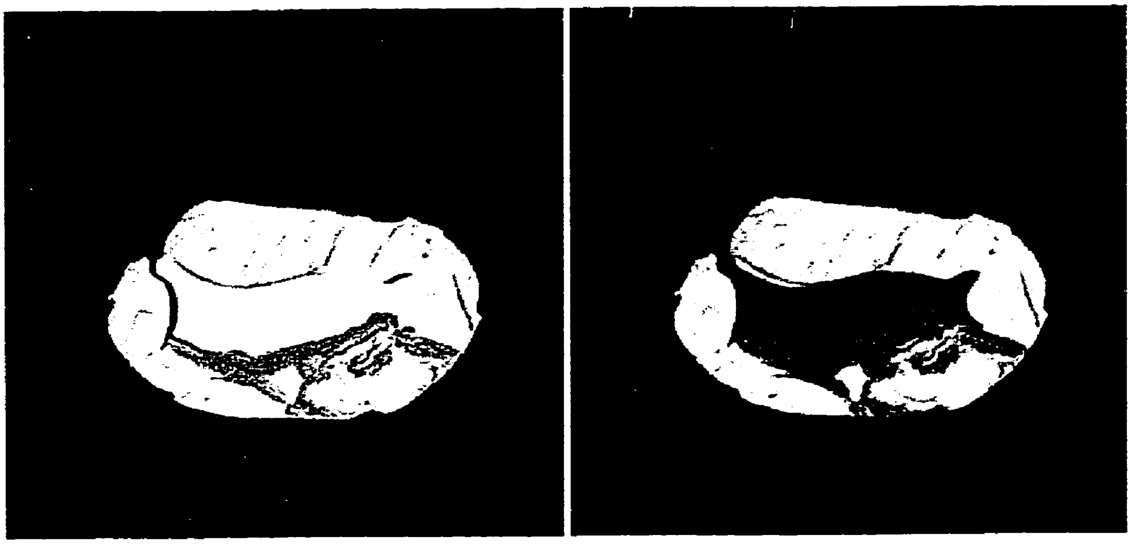

(a) In-phase image

(b) Water image

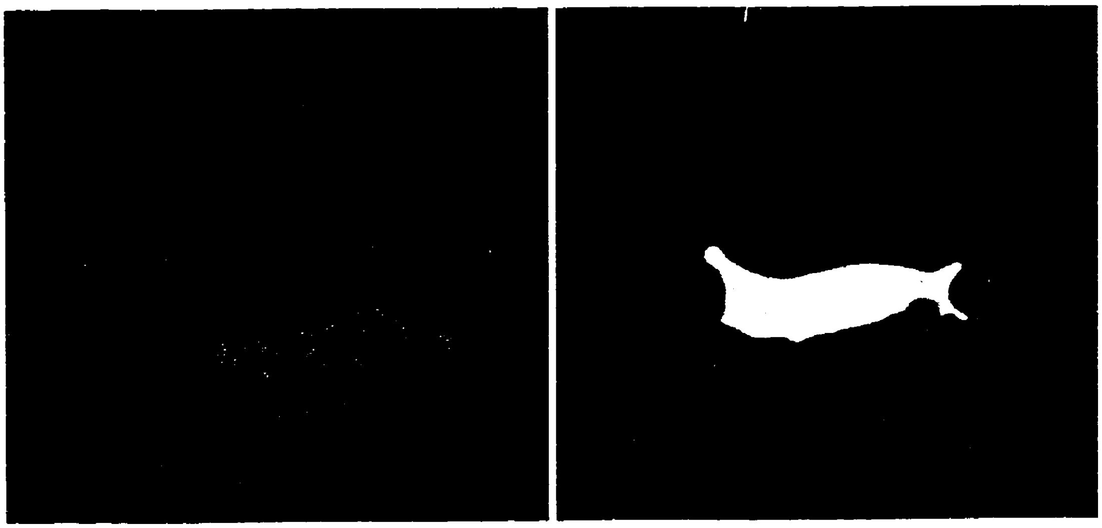

(c) Fat image

(d) Silicone image

Figure 7-8 Transverse images of a pork-silicone phantom acquired at 1.5 T with 13 slices. Spin-echo, TR=800ms, TE=25.6ms.

7.5 Discussion

Before data acquisitions are performed, the spectrum of the sample is modeled as several separated peaks with known resonance frequencies but unknown peak amplitudes. The spectrum model is based on localized NMR spectroscopy experiments or published information. With the help of the spectrum model, we only need to sample several special points in the temporal direction to resolve the spectrum instead of hundreds of evenly distributed points as in a NMR spectroscopy or a Fourier transform based chemical shift imaging. This is the key to the imaging efficiency of CSISM. With spatial resolution, the special points in the temporal direction are actually spin-echo images. The temporal positions of these spin-echo images are controlled by the time shifts of the 180° RF pulses relative to their Hahn echo positions.

The time shifts of the 180° RF pulses are so chosen that matrix A^TA to be well conditioned while keeping the time shift not too large. When matrix A^TA is well conditioned, the inverse of matrix A^TA will be stable, as a result, the solutions will be more stable. Meanwhile, when matrix A^TA is well conditioned, the SNR of the final spectroscopic images will also be close to optimal.

The simplest shape model for the peaks are delta-function shapes, i.e. the peaks have no line broadening. Other shape models for the peaks can also be used by changing the values of A_k ($k = 0, 1, \ldots, K$). For peak shapes other than delta-function shape, the magnitude of A_k will be less than 1.

The number of spin-echo images K must satisfy that $2K-1 \geq N+1$, where N is the number of peaks in the model of the spectra. However, enough images do not guarantee the unambiguous solutions to the unknowns everywhere in the FOV. The spectra for some pixels, with single peak or insufficient number of peaks, cannot be unambiguously resolved. Information from other pixels must be used to help solve this problem.

The SNR of CSISM is close to optimal. The more images you acquire, the more reliable results and better SNR you can get, provided the temporal positions of the images are correctly chosen.

One major limitation of CSISM is that every peak in the spectrum that you want to distinguish must have strong enough signal. Otherwise, the small peaks will be embedded in noise and errors of large peaks, thus cannot be resolved.

CSISM achieves spectroscopic resolution while its scan time, spatial resolution, and image SNR is comparable with those of ordinary spin-echo imaging applications. CSISM should be able to be used for applications with reasonable peak amplitudes and well defined peak separations. Water-fat-silicone imaging appears to be the first practical application of CSISM.

CHAPTER 8

CONCLUSION

Among all the CSI methods we developed, one common characteristic is spectrum modeling before data acquisitions. A spectrum is modeled as two peaks in water-fat imaging or several peaks in CSISM based on prior knowledge about the spectrum, which comes from published information or localized NMR spectroscopy experiments. With the help of the spectrum model, several data acquisitions are enough to yield the chemical shift images, for which hundreds of data acquisitions are needed by Fourier transform based CSI methods.

It is Dixon [22] who first introduced spectrum modeling to water-fat chemical shift imaging, which led to a dramatic improvement in imaging efficiency. However, in the Dixon method and its variations, the phase relationship between water and fat magnetization vectors is not fully used, thus the symmetry between water and fat cannot be broken. DPE samples the water and fat magnetization vectors asymmetrically and breaks the symmetry between water and fat. Unlike existing water-fat imaging methods, DPE fully exploits the complex nature of the MRI signal. The leading and lagging phase relationship between the magnetization vectors of water and fat is used to identify them. DPE allows a direct and unambiguous determination of water and fat on a pixel by pixel basis. This is a fundamental difference between DPE and other existing methods. To correct for possible wrong water-fat assignments due to single peaks, artifacts, and noise, GOF is developed. GOF is a statistical operator by nature, and thus is reliable. With second pass solutions and optimal averaging, DPE offers good image SNR. DPE with a sampling scheme of $(0°,90°,180°)$ has been implemented at several local hospitals and thousands of water-fat images have been successfully reconstructed and used as part of their clinical practice [66].

In chapter 4, we proved that optimal averaging is equivalent to the complex valued LSE method. Generally, image SNR for DPE can be further improved with the real valued LSE method. For the sampling scheme of $(0°,90°,180°)$, the image NSA* is improved from 2.67 with optimal averaging to 3.0 with the real valued LSE method.

TOP is a special sampling scheme of DPE, allowing the correction of magnitude errors due to intra-voxel dephasing (T_2^*) or other effects causing magnitude modulations. TOP also has the maximum solution stability among all possible DPE sampling schemes. A more efficient orientation filter SRF is developed for TOP and any other DPE sampling schemes, for which the middle acquisition is quadrature. SRF is adaptive and stable with the use of a regional minimum spanning tree algorithm. Compared to a general GOF, SRF is more efficient and robust. TOP has been successfully tested on volunteers at a local hospital and the water-fat images are excellent.

Unlike other 2-point methods with symmetric sampling, MGE solves the order /connectivity problem, as demonstrated in a 2-point double-spin-echo single-excitation experiment. By minimizing the gradient energy of a phasor map, correct water-fat assignments are achieved. With second pass solution using real valued LSE method, image SNR for MGE is close to optimal. MGE has been successfully tested on volunteers at a local hospital.

When robustness and good image SNR are required, TOP and other DPE sampling schemes, such as the $(0°,90°,180°)$ scheme, are the methods of choice. Even though

TOP or the $(0°, 90°, 180°)$ sampling scheme uses three data acquisitions which triples the scanning time of a spin-echo sequence, the NSA* of the water and fat images is 3.0, therefore there is no waste of scanning time. As a matter of fact, spin-echo imaging with three or more image averages is often used in the hospitals for an improved SNR. DPE can provide normal water-fat in-phase images with good SNR, as well as a pair of water and fat images as a bonus. When scan time is a major concern for some applications, the 2-point MGE method should be implemented with a double-echo single-excitation pulse sequence. The imaging time for MGE is only one-third of the imaging time needed for DPE. However, the allowed number of interleaved slices in one scan for MGE is reduced because there are two echoes in each excitation. A one-point qualitative water-fat imaging method is newly proposed [74], where a pair of qualitative water and fat images can be resolved from a single quadrature acquisition. This approach allows more interleaved slices than MGE does. Due to its fast speed, this one-point method can be used when a qualitative fat suppression is needed.

CSISM is an extension of DPE to general chemical shift imaging. It works well for spectra with well-defined peak resonance frequencies and sufficiently large peak SNR. CSISM models a spectrum as several peaks and find the amplitudes of these peaks from a set of spin-echo images. The time shifts of the RF pulses are so chosen that matrix ATA can be well conditioned while keeping the time shift not too large. When matrix A^TA is well conditioned, the first pass solutions will be stable and the SNR of the final spectroscopic images will also be close to optimal. CSISM has been successfully tested with ethanol phantoms and pork-silicone phantoms. Water-fat-silicone images are also successfully reconstructed from a clinical scan of a female patient with silicone implants.

In the future, we plan to do more clinical trials for DPE, TOP and MGE. Our final goal is to make a series of water-fat imaging methods clinically available. Although these techniques have been mostly demonstrated with spin-echo experiments in this thesis, they are by no means limited to spin-echo imaging. Being independent methods, they can be combined with many other existing MRI methods, such as gradient-echo imaging, RARE [75], or fast-spin-echo imaging [34,76], or echo-planar-imaging [77] for a faster scan time. Further development of water-fat-silicone imaging is also high on our agenda. More experiments on phantoms or volunteers with silicone implants are needed for optimized performance. In addition to water-fat-silicone imaging, we also anticipate other practical applications for CSISM. Phosphate is an attractive potential candidate for CSISM because of balanced peak amplitudes in its spectrum.

APPENDIX A

Form equations (3-18) to (3-23), the water image after weighted averaging can be written as

$$< W > = \frac{A}{A-1}(\lambda + \frac{A}{A+1}\xi)J_1 + \frac{1}{A-1}(A\eta - \lambda)J_2 - \frac{1}{A-1}(\eta + \frac{\xi}{A+1})J_1 \qquad \text{(A-1)}$$

According to the rule of noise propagation, the noise variance in <W> is

$$\sigma_W{}^2 = \sum_{i=1}^{3} \left| \frac{\partial < W >}{\partial J_i} \right|^2 \sigma_0{}^2 \qquad \text{(A-2)}$$

We have assumed that J_1, J_2, and J_3 have the same noise variance as their original couterparts I_1, I_2, and I_3, i.e. $\sigma_1{}^2 = \sigma_2{}^2 = \sigma_3{}^2 = \sigma_0{}^2$, since the noise variances in the phasors P_0, P_0P_1, and $P_0P_1{}^2$ are greatly reduced by heavy smoothing operations so that they can be negligible. Using the fact that $A = \exp(i\alpha)$ and $|A| = 1$, we find the output-input noise variance ratio

$$\begin{aligned} \frac{\sigma_W{}^2}{\sigma_0{}^2} &= \frac{1}{|A-1|^2}(|\lambda + \frac{A}{A+1}\xi|^2 + |A\eta - \lambda|^2 + |\eta + \frac{\xi}{A+1}|^2) \\ &= \frac{1}{1-\cos\alpha}[\lambda^2 + \eta^2 - \lambda\eta\cos\alpha + (\lambda+\eta)\xi/2 + \xi^2/(1+\cos\alpha)] \end{aligned} \qquad \text{(A-3)}$$

Substituting ξ with $1-\lambda-\eta$, we have

$$\frac{\sigma_W{}^2}{\sigma_0{}^2} = \frac{2(1+\cos\alpha)}{1-\cos\alpha}[(\lambda^2 + \eta^2 - 2\lambda\eta\cos\alpha)(2+\cos\alpha) + (\lambda+\eta)(\cos\alpha - 1) + 1] \qquad \text{(A-4)}$$

To minimize the above expression with appropriate λ and η, we need

$$\begin{aligned} &\frac{\partial}{\partial\lambda}(\frac{\sigma_W{}^2}{\sigma_0{}^2}) = 0 \\ &\frac{\partial}{\partial\eta}(\frac{\sigma_W{}^2}{\sigma_0{}^2}) = 0 \end{aligned} \qquad \text{(A-5)}$$

From equations (A-5), it is straightforward to obtain the following

$$\begin{aligned} \lambda = \eta &= \frac{1}{2(2+\cos\alpha)} \\ \xi &= \frac{1+\cos\alpha}{2+\cos\alpha} \end{aligned} \qquad \text{(A-6)}$$

Substituting (A-6) into (A-3), the optimized output-input noise variance ratio is

$$\left(\frac{\sigma_w^2}{\sigma_0^2}\right)_{opt} = \frac{3}{4(2+\cos\alpha)(1-\cos\alpha)} \qquad \text{(A-7)}$$

Therefore, the optimized equivalent "number of signal average" (NSA*) [24] is

$$(NSA^*)_{opt} = 1/\left(\frac{\sigma_w^2}{\sigma_0^2}\right)_{opt} = \frac{4}{3}(2+\cos\alpha)(1-\cos\alpha) \qquad \text{(A-8)}$$

Substituting $\lambda = \eta = \xi = 1/3$ into (A-3), we obtain the corresponding result for simple averaging

$$\left(\frac{\sigma_w^2}{\sigma_0^2}\right)_{simple} = \frac{5+4\cos\alpha+2\sin^2\alpha}{18\sin^2\alpha} \qquad \text{(A-9)}$$

and

$$\begin{aligned} (NSA^*)_{simple} &= 1/\left(\frac{\sigma_w^2}{\sigma_0^2}\right)_{simple} \\ &= \frac{18\sin^2\alpha}{5+4\cos\alpha+2\sin^2\alpha} \end{aligned} \qquad \text{(A-10)}$$

Exactly analogous procedure can yield identical result for the fat image.

APPENDIX B

Substituting equations (3-20), (3-21), (3-22), and (3-24) into equations (3-23), the final water-fat result with the optimal averaging method is given by

$$
\begin{aligned}
\begin{pmatrix} <W> \\ <F> \end{pmatrix} &= \frac{1}{2(2+\cos\alpha)}\begin{pmatrix} W_{12} \\ F_{12} \end{pmatrix} + \frac{1}{2(2+\cos\alpha)}\begin{pmatrix} W_{23} \\ F_{23} \end{pmatrix} + \frac{1+\cos\alpha}{2+\cos\alpha}\begin{pmatrix} W_{13} \\ F_{13} \end{pmatrix} \\
&= \begin{pmatrix} A(A+2)(A+1)I_1 + (A+1)(A-1)I_2 - A^*(2A+1)(A+1)I_3 \\ -C^*A^*(2A+1)(A+1)I_1 + C^*A^*(A+1)(A-1)I_2 + C^*A^*(A+2)(A+1)I_3 \end{pmatrix} \\
&\quad / \, [2(2+\cos\alpha)(A-1)(A+1)] \\
&= \frac{1}{2(2+\cos\alpha)(A-1)}\begin{pmatrix} A(A+2)I_1 + (A+(A-1)I_2 - A^*(2A+1)I_3 \\ -C^*A^*(2A+1)I_1 + C^*A^*(A-1)I_2 + C^*A^*(A+2)I_3 \end{pmatrix}
\end{aligned}
\tag{B-1}
$$

Substituting equations (4-4) into equations (4-6), matrix L for the complex valued LSE method is given by

$$
\begin{aligned}
L &= \begin{pmatrix} 2-A-A^2, & 2-A^*-A, & 2-A^{*2}-A^* \\ C^*(2-A^{*2}-A^*), & C^*(2A^*-1-A^{*2}), & C^*(2A^{*2}-1-A^*) \end{pmatrix} \\
&\quad / \, [(4+A+A^*)(2-A-A^*)] \\
&= \begin{pmatrix} -(A+2)(A-1), & -A^*(A-1)^2, & A^{*2}(2A+1)(A-1) \\ C^*A^{*2}(2A+1)(A-1), & -C^*A^{*2}(A-1)^2, & -C^*A^{*2}(A+2)(A-1) \end{pmatrix} \\
&\quad / \, [2(2+\cos\alpha)(-A^*)(A-1)^2] \\
&= \frac{1}{2(2+\cos\alpha)(A-1)}\begin{pmatrix} A(A+2), & (A-1), & -A^*(2A+1) \\ -C^*A^*(2A+1), & C^*A^*(A-1), & C^*A^*(A+2) \end{pmatrix}
\end{aligned}
\tag{B-2}
$$

The final water-fat result with the complex valued LSE method can be obtained by simply substituting equation (B-2) into equation (4-7)

$$
\begin{pmatrix} W \\ F \end{pmatrix} = \frac{1}{2(2+\cos\alpha)(A-1)}\begin{pmatrix} A(A+2)I_1 + (A+(A-1)I_2 - A^*(2A+1)I_3 \\ -C^*A^*(2A+1)I_1 + C^*A^*(A-1)I_2 + C^*A^*(A+2)I_3 \end{pmatrix} \tag{B-3}
$$

The result in equation (B-3) is identical with the result in equation (B-1). Therefore, the optimal averaging method is identical to the complex valued LSE method.

REFERENCES

[1] R. Frisch and O. Stern, Z. Phys. 85, 4 (1933)

[2] I. Estermann and O. Stern, Z. Phys. 85, 17 (1933)

[3] I. I. Rabi, J. R. Zacharias, S. Millman, and P. Kusch, "A New Method of Measuring Nuclear Magnetic Moment," Phys. Rev. 53, 318 (1938)

[4] E. D. Becker, C. L. Fisk, and C. L. Khetrapal, "The Development of NMR", Encyclopedia of Nuclear Magnetic Resonance," 1-158, Editors-in-chief, D. M. Grant and R. K. Harris, John Wiley & Sons (1996)

[5] E. M. Purcell, H. C. Torrey, and R. V. Pound, "Resonance Absorption by Nuclear Magnetic Moments in a Solid," Phys. Rev. 69, 37 (1946)

[6] F. Bloch, W. W. Hansen, and M. Packard, "Nuclear Induction," Phys. Rev. 69, 127 (1946)

[7] P. C. Lauterbur, "Image Formation by Induced Local Interactions: Examples Employing Nuclear Magnetic Resonance," Nature, 242, 190-191 (1973)

[8] A. Kumar, D. Welti, and R. R. Ernst, "NMR Fourier Zeugmatography," J. Magn. Reson., 18, 69-83 (1975)

[9] W. A. Edelstein, J. M. S. Hutchison, G. Johnson, and T. W. Redpath, "Spin Warp NMR Imaging and Applications to Human Whole-Body Imaging," Phys. Med. Biol. 25, 751-756 (1980)

[10] D. I. Hoult, "Sensitivity of the NMR Experiment", Encyclopedia of Nuclear Magnetic Resonance, 4256-4266, Editors-in-chief, D. M. Grant and R. K. Harris, John Wiley & Sons (1996)

[11] W. G. Proctor and F. C. Yu, "The Dependence of Nuclear Magnetic Resonance Frequency upon Chemical Compound," Phys Rev., 77, 717 (1950)

[12] J. T. Arnold, S. S. Dharmatti, and M. E. Packard, J. Chem. Phys. 19, 507 (1951)

[13] R. R. Ernst and W. A. Anderson, "Application of Fourier Transform Spectroscopy to Magnetic Resonance," Rev. Sci. Instr. 37, 93-102 (1965)

[14] E. Hahn, "Spin Echoes", Phys. Rev. 80(4), 580-594 (1950)

[15] H. Y. Carr and E. M. Purcell, Phys. Rev., 94, 630 (1954)

[16] A. N. Garroway, P. K. Grannell, and P. Mansfield, J. Phys. C, 7, L457 (1974)

[17] A. Haase, J. Frahm, D. Matthaei, W. Haenicke, K. D. Merboldt, "FLASH Imaging: Rapid NMR Imaging Using Low Flip Angle Pulses," J. Magn. Reson. 67, 258-266 (1986)

[18] T. R. Brown, B. M. Kincaid, and K. Ugurbil, "NMR Chemical Shift Imaging in Three Dimensions," Proc. Natl. Acad. Sci. 79, 3523-3526 (1982)

[19] A. A. Maudsley, S. K. Hilal, H. E. Simon, And W. H. Perman, "Spatially Resolved High Resolution Spectroscopy by 'Four Dimensional' NMR," J. Magn. Reson. 51, 147-152 (1983)

[20] I. L. Pykett and B. R. Rosen, "Nuclear Magnetic Resonance: In Vivo Proton Chemical Shift Imaging", Radiology, 149, 197-201 (1983)

[21] R. E. Sepponen, J. T. Sipponen, and J. I. Tanttu, " A Method for Chemical Shift Imaging: Demonstration of Bone Marrow Involvement with Proton Chemical Shift Imaging," J. Comput. Assist. Tomogr., 8, 585-587 (1984)

[22] W. T. Dixon, " Simple Proton Spectroscopic Imaging," Radiology, 153, 189-194 (1984)

[23] Z. Paltiel, "Separate Water and Lipids Images Obtained by a Single Scan," proceedings of 4th SMRM, 172-173 (1985)

[24] J. L. Patrick, E. M. Haacke, and J. E. Hahn, "Water/Fat Separation and Chemical Shift Artifact Correction Using a Single Scan," proceedings of 4th SMRM, 174-175 (1985)

[25] C. B. Ahn, S. Y. Lee, O. Nalcioglu, and Z. H. Cho, "Spectroscopic Imaging by Quadrature Modulated Echo Time Shifting," presented at 4th SMRI, Magn. Reson. Imag. 4, 110-111 (1986)

[26] C. B. Ahn and Z. H. Cho, "A New Phase Correction Method in NMR Imaging Based on Autocorrelation and Histogram Analysis," IEEE Trans. Med. Imag. MI-6, 32-36 (1987)

[27] J. V. Hajnal and I. R. Young, "Use of Spatial Phase Distribution Models to Produce Water and Fat only Imaging from Single Echo Shifted Data Sets," proceedings of the 3rd SMR, 650 (1995)

[28] H. N. Yeung and D. W. Kormos, "Seperation of True Fat and Water Images by Correcting Magnetic Field Inhomogeneity in Situ," Radiology, 159, 783-786 (1986)

[29] H. N. Yeung and D. W. Kormos, and D. A. Sebok, "Single-Acquisition Chemical-Shift Imaging of a Binary System with Use of Stimulated Echoes," Radiology, 167, 537-540 (1988)

[30] C. C. Lodes, J. P. Felmlee, R. L. Ehman, *et al.* "Proton Chemical Shift Imaging Using Double and Triple Phase Contrast Acquisition Methods," J. Comput. Assist. Tomogr. 13, 855-861 (1989)

[31] G. H. Glover and E. Schneider, "Three-Point Dixon Technique for True Water/Fat Decomposition with B_0 Inhomogeneity Correction," Magn. Reson. Med. 18, 371-383 (1991)

[32] G. H. Glover, "Multipoint Dixon Technique for Water and Fat Proton and Susceptibility Imaging," J. Magn. Reson. Imag. 1, 521-530 (1991)

[33] J. Szumowski, W. R. Coshow, F. Li, and S. F. Quinn, "Phase Unwrapping in the Three-Point Dixon Method for Fat Suppression MR Imaging," Radiology, 192, 555-561 (1994)

[34] P. A. Hardy, R. S. Hinks, and J. A. Tkach, "Separation of Fat and Water in Fast Spin-Echo MR Imaging with the Three-Point Dixon Technique," J. Magn. Reson. Imag. 5, 181-185 (1995)

[35] J. Szumowski, W. R. Coshow, F. Li, B. Coombs, and S. F. Quinn, "Double-Echo Three-Point-Dixon Method for Fat Suppression MRI," Magn. Reson. Med. 34, 120-124 (1995)

[36] S. C. R. Williams, M. A. Horsfield, and L. D. Hall, "True Water and Fat MR Imaging with Use of Multiple-Echo Acquisition," Radiology, 173, 249-253 (1989)

[37] Q. S. Xiang, L. An, D. Aikins, and A. MacKay, "Phase Correction in Two-Point Dixon Chemical Shift Imaging," Poceedings of 3rd SMR, 1904 (1995)

[38] C. Z. Yang, D. N. Firmin, R. H. Mohiaddin, J. P. Konrad, D. B. Longmore, "B_0 Inhomogeneity Correction for Two Point Dixon Chemical Shift Imaging," proceedings of 11th SMRM, 3819 (1992)

[39] B. D. Coombs, J. Szumowski, W. Coshow, and F. Li, "Two-Point Dixon Technique for Water-Fat Signal Decomposition with B_0 Inhomogeneity Correction," Proceedings of 3rd SMR, 647 (1995)

[40] E. M. Akkerman and M. Maas, "A Region-Growing Algorithm to Simultaneously Remove Dephasing Influences and Separate Fat and Water in Two-Point Dixon Imaging," Proceedings of 3rd SMR, 649 (1995)

[41] G. Zhu, J. Huang, and S. Freeland, "A Robust Water and Fat Separation Method," Proceedings of 4th SMR, 1542 (1996)

[42] B. D. Coombs, Jerzy Szumowski, William Coshow, "Two-Point Dixon Technique for Water-Fat Signal Decomposition with B_0 Inhomogeneity Correction," Magn. Reson. Med. 38, 884-889 (1997)

[43] T. E. Skinner, G. H. Glover, "An Extended Two-Point Dixon Algorithm for Calculating Separate Water, Fat, and B_0 Images," Magn. Reson. Med. 37, 628-630 (1997)

[44] T. R. Judge, P. J. Bryanston-Cross, "A Review of Phase Unwrapping Techniques in Fringe Analysis," Optics and Lasers in Engineering, 21, 199-239 (1994)

[45] Z. P. Liang, "A New Algorithm for Obtaining Unwrapped Phase Images," Proceedings of 3rd SMR, 648 (1995)

[46] S. Nakadate and H. Saito, "Fringe Scanning Speckle-Pattern Interferometry," Appl. Optics, 24 (14), 2172-2180 (1985)

[47] D. C. Ghiglia, G. A. Mastin, and L. A. Romero, "Cellular-Automata Method for Phase Unwrapping," J. Opt. Soc. Am. 4A, 267-280 (1987)

[48] R. M. Goldstein, H. A. Zebker, and C. L. Werner, "Satallite Radar Interferometry Two-Dimensional Phase Unwrapping," Radio Science, 23 (4), 713-720 (1988)

[49] D. J. Bone, "Fourier Fringe Analysis: The Two-Dimensional Phase Unwrapping Problem," Appl. Optics, 30 (25), 3627-3632 (1991)

[50] J. J. Gierloff, "Phase unwrapping by Regions," In Current Developements in Optical Engineering II, SPIE Vol. 818, 2-9 (1987)

[51] J. M. Huntley, R. Cuzack, and H. Saldner, "New Phase Unwrapping Algorithms," Proc. 2nd Int. Workshop on Automatic Processing of Fringe Patterns, 148-153 (1993)

[52] Q. S. Xiang, "Temporal Phase Unwrapping for CINE Velocity Imaging", J. Magn. Reson. Imag., 5, 529 (1995)

[53] Q. S. Xiang and L An, " Pseudo Temporal Phase Unwrapping (PTPU): A Diffusion Model," proceedings of 3rd SMR, 37 (1995)

[54] H. Takajo and T. Takahashi, "Least-squares Phase Estimation From The Phase Difference," J. Opt. Soc. Am. A, Vol. 5, No. 3, 416 (1988)

[55] D. C. Ghiglia and Louise A. Romero, "Robust Two-Dimensional Weighted and Unweighted Phase Unwrapping That Uses Fast Transforms and Iterative Methods,", J. Opt. Soc. Am. A, Vol. 11, No. 1, 107-117 (1994)

[56] R. J. Green and J. G. Walker, "Phase Unwrapping Using A Priori Knowledge about The Band Limits of A Function," Industrial Inspection, SPIE, 1010, 36-43 (1988)

[57] D. P. Towers, T. R. Judge, and P. J. Bryanston-Cross, "A Quasi-Heterodyne Holographic Technique and Automatic Algorithms for Phase Unwrapping," SPIE, Vol. 1163 (1989)

[58] S. Chavez and Q. S. Xiang, "2D Phase Unwrapping Based on Dipole Connections," proceedings of the 5th ISMRM, 2053 (1997)

[59] Q. S. Xiang and L. An, "Water-Fat Imaging with Three-Point Direct Phase Encoding," Proceedings of 3rd SMR, 658 (1995)

[60] Q. S. Xiang and L. An, " General 3-Point Water-Fat Imaging with Optimized SNR," proceedings of 4th SMR, 1904 (1996)

[61] Q. S. Xiang and L. An, "Water-Fat Imaging with Direct Phase Encoding," J. Magn. Reson. Imag. 7, 1002-1015 (1997)

[62] Gray's Anatomy, 37th ed. Churchill-Livingstone (1989)

[63] Q. S. Xiang and R. M. Henkelman, "Weighted Average and its Application in Ghost Artifacts Reduction," proceedings of 9th SMRI, 22 (1991)

[64] J. K. Riek, S. M. Totterman, A. M. Tekalp, *et al.*, "Flow Compensation in MRI Using a Phase-Corrected Real Reconstruction," Magn. Reson. Med., 30, 724-731 (1993)

[65] J. H. Bilbey, R. F. McLoughlin, P. S. Kurkjian, *et al.* "MR Imaging of Adrenal Masses: Value of Chemical-Shift Imaging for Distingushing Adenomas From Other Tumors," A. J. R. 164, 637-642 (1995)

[66] M. A. Sargent, R. A. Cairns, K. J. Poskitt, M. S. Johnson, Q. S. Xiang, and L. An, "Clinical Pediatric Experience Using Three-point Water-Fat Imaging for Fat Suppression," proceedings of 6th ISMRM, 1352 (1998)

[67] L. An and Q. S. Xiang, "Water-Fat Imaging with Three Orthogonal-Phase Acquisitions," proceedings of 6th ISMRM, 1866 (1998)

[68] B. Klaus and P. Horn, “Robot Vision,” The MIT Press, Cambridge, Massachusetts, USA (1986)

[69] T. H. Cormen, C. E. Leiserson, and R. L. Rivest, “Introduction to Algorithms,” The MIT Press, Cambridge, Massachusetts, USA (1990)

[70] L. An and Q. S. Xiang, "Quadrature 2-Point Water-Fat Imaging," proceedings of 4th ISMRM, 1541 (1996)

[71] Q. S. Xiang, M. J. Bronskill, and R. M. Henkelman, “Two-Point Interference Method for Suppression of Ghost Artifacts Due to Motion,” J. Magn. Reson. Imag. 3, 900-906 (1993)

[72] L. An and Q. S. Xiang, "Chemical Shift Imaging with Spectrum Modeling", proceedings of 5th ISMRM, 1456 (1997)

[73] E. Schneider and T. S. Chan, "Selective MR Imaging of Silicone with the Three-point Dixon Technique," Radiology, 187, 89-93 (1993)

[74] Q. S. Xiang, “Fat Suppression with Single Quadrature Acquisition,” proceedings of 6th ISMRM, 1880 (1998)

[75] J. Hennig, A. Nauerth, H. Friedburg, "RARE Imaging: A fast imaging method for clinical MR," Magn. Reson. Med. 3, 823-833 (1986)

[76] J. Ma, "Multi-Point Dixon Imaging with Reduced Time and Increased Reliability," proceedings of 6th ISMRM, 622 (1998)

[77] P. Mansfield, "Multi-Planar Image Formation Using NMR spin echoes," J. Phys. C10, L55-L58 (1977)